

The SALT survey of helium-rich hot subdwarfs: methods, classification, and coarse analysis.

C. S. Jeffery¹, B. Miszalski² and E. Snowdon¹

¹*Armagh Observatory and Planetarium, College Hill, Armagh BT61 9DG, United Kingdom*

³*Australian Astronomical Optics - Macquarie, Faculty of Science and Engineering, Macquarie University, North Ryde, NSW 2113, Australia*

Accepted Received . . . ; in original form . . .

ABSTRACT

A medium- and high-resolution spectroscopic survey of helium-rich hot subdwarfs is being carried out using the Southern African Large Telescope (SALT). Objectives include the discovery of exotic hot subdwarfs and of sequences connecting chemically-peculiar subdwarfs of different types. The first phase consists of medium-resolution spectroscopy of over 100 stars selected from low-resolution surveys. This paper describes the selection criteria, and the observing, classification and analysis methods. It presents 107 spectral classifications on the MK-like Drilling system and 106 coarse analyses (T_{eff} , $\log g$, $\log y$) based on a hybrid grid of zero-metal non-LTE and line-blanketed LTE model atmospheres. For 75 stars, atmospheric parameters have been derived for the first time. The sample may be divided into 6 distinct groups including the classical ‘helium-rich’ sdO stars with spectral types (Sp) sdO6.5 - sdB1 (74) comprising carbon-rich (35) and carbon-weak (39) stars, very hot He-sdO’s with Sp \leq sdO6 (13), extreme helium stars with luminosity class \leq 5 (5), intermediate helium-rich subdwarfs with helium class 25 – 35 (8), and intermediate helium-rich subdwarfs with helium class 10 – 25 (6). The last covers a narrow spectral range (sdB0 – sdB1) including two known and four candidate heavy-metal subdwarfs. Within other groups are several stars of individual interest, including an extremely metal-poor helium star, candidate double-helium subdwarf binaries, and a candidate low-gravity He-sdO star.

Key words: stars: early type, stars: subdwarfs, stars: chemically peculiar, stars: fundamental parameters

1 INTRODUCTION

Hot subluminal stars can be divided into three major groups. These include i) the hydrogen-rich subdwarf B (sdB) stars, often characterized as extreme horizontal-branch stars, ii) the sdOB and sdO stars lying on or around the helium-main sequence, and iii) the more luminous sdO stars on post-AGB evolution tracks (Heber 2016). Apart from the sdB stars which have hydrogen-rich surfaces, a substantial fraction of hot subdwarfs have hydrogen-deficient or hydrogen-weak surfaces. Amongst these, there is evidence for sequences extending either away from or towards the helium main-sequence, connecting with cooler extreme helium stars, or with the white dwarf cooling sequence; many have atmospheres enriched in carbon or nitrogen or both. Amongst the subdwarfs with hydrogen-weak surfaces, several show extraordinary overabundances of heavy metals (transition elements) including zirconium and lead (Naslim et al. 2011, 2013). This diversity is apparent in the helium subclasses identified by Drilling et al. (2013) (D13 hereafter), who noted that certain classes of helium-rich hot subdwarf and extreme helium stars are difficult to distinguish at low resolution. In order to trace these sequences of hydrogen-deficient and hydrogen-weak subdwarfs with greater clarity, to discover how they relate to other categories of hydrogen-deficient star, and to study the physics that transforms their surface chemistries, we commenced a survey of chemically-peculiar hot subdwarfs. The object of the survey would be to obtain spectra of sufficient quality to measure effective temperature, surface gravities, and surface hydrogen, helium, carbon and nitrogen abundances, as

well as to identify any exotic elements that might be present. This paper reports the initial part of the survey including selection criteria, observing procedures, data products and primary classifications.

2 OBSERVATIONS

2.1 Target selection

The primary motivation for this survey was the classification of several stars in the Edinburgh-Cape (EC) survey of faint blue stars as ‘He-sdB’ (Stobie et al. 1997a; Kilkenny et al. 1997), a classification similar to sdOD in the Palomar-Green (PG) survey (Green et al. 1986) and indistinguishable at the survey resolutions from that of ‘extreme helium stars’ (D13). Efforts to explore this category by Ahmad & Jeffery (2003) and by Naslim et al. (2010) were limited by telescope aperture and observing time. The construction of the Southern African Large Telescope (SALT) offered the perfect opportunity to extend previous studies.

Initial target selection was made on the basis of low-resolution classifications of He-sdB, He-sdOB and He-sdO in the EC survey. These classifications are described by Moehler et al. (1990b); Geier et al. (2017) and Lei et al. (2020). To these were added similar stars classified He-sdB, sdOD, or similar in one or more of the compilations by Carnochan & Wilson (1983); Green et al. (1986); Kilkenny & Lynas-Gray (1982); Kilkenny (1988); Beers et al. (1992); Stobie et al. (1997a); Kilkenny et al.

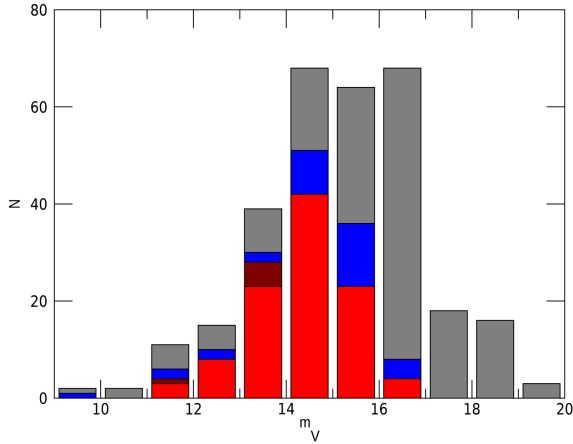


Figure 1. Relative numbers of known or suspected He-sdO, He-sdOB and He-sdB stars visible from SALT ordered by brightness. The coloured segments represent the numbers observed in the current sample with SALT/RSS only or with SALT/RSS and SALT/HRS (103 stars: red), with SALT/HRS only (6: dark red), or with another high-resolution spectrograph and *not* SALT (33: blue). As of 2020 September 30, the total known to us is 306.

Table 1. Observation dates in the form *yyyymmdd*. The full table is given in the Supplementary Online Data.

Name	RSS Dates	HRS Dates
Ton S 144	20181101	20180611
Ton S 148	20191101	20180616 20180705 20180722 20190619 20190715
...

(1997); Adelman-McCarthy et al. (2006); Østensen (2006); Németh et al. (2012); O’Donoghue et al. (2013); Kilkenny et al. (2015); Kepler et al. (2015); Kilkenny et al. (2016) or Geier et al. (2017). Stars which had been observed at high resolution with échelle spectrographs at either VLT/UVES (Ströer et al. 2007), AAT/UCLES (Ahmad et al. 2007; Naslim et al. 2011, 2012), ESO/FEROS (Naslim et al. 2013), or Subaru/HDS (Jeffery et al. 2017b; Naslim et al. 2020) were not included at first, but the benefits of having medium resolution spectra available for class prototypes meant that some were included later.

Since the boundaries between He-sdB, He-sdOB and He-sdO are spectroscopic and therefore artificial in terms of exploring connections between stars in closely related classes, stars from all three categories were included as the survey progressed. Moreover, since some chemically-peculiar subdwarfs simply have solar or slightly super-solar abundances of helium, we included a number of sdOB and sdO stars. The principal exclusions were stars classified sdB, since these usually have weak or absent HeI and no HeII lines.

Our helium-rich list currently (2020 September) contains over 600 subdwarfs, of which 306 lie between the declinations of -75° and $+8^\circ$, the effective limits of SALT. Some 33 of the latter have been observed at high resolution in campaigns cited above and are not included here. Approximately 30 are common to previous campaigns and to the SALT observations presented here. Figure 1 shows the brightness distribution of known or suspected southern helium-rich subdwarfs accessible to SALT.

2.2 SALT/HRS

From 2016 to the present, observations have been obtained with the SALT High Resolution Spectrograph (HRS: $R \approx 43\,000$, $\lambda\lambda = 4100 - 5200\text{\AA}$, Bramall et al. 2010). Observation dates are given in Table 1. HRS spectra obtained prior to 2019 were reduced to order-by-order wavelength calibrated rectified form using the SALT pipeline pyHRS (Crawford et al. 2016); orders were stitched into a single spectrum using our own software. In general, spectra were obtained in pairs (or a higher multiple) which were coadded to provide a single observation for each date. The pyHRS pipeline ceased to be supported after the beginning of 2019. HRS spectra obtained after that date will be described in a subsequent paper.

2.3 SALT/RSS

To reduce errors arising from poor blaze correction, which is difficult for broad-lined spectra, and also to extend the sample to stars too faint for HRS, observations were also obtained with the SALT Robert Stobie Spectrograph (RSS: resolution $R \approx 3\,600$, Burgh et al. (2003); Kobulnicky et al. (2003)). Observation dates are given in Table 1. Since the RSS detector consists of three charge-coupled devices separated by two gaps, double exposures were taken at two different grating angles. This provides a continuous spectrum in the wavelength range $3850 - 5150\text{\AA}$ and assists in the removal of cosmic-ray contamination. Basic data processing used the PYSALT¹ package (Crawford et al. 2010). Reduction used standard IRAF tasks and the LACOSMIC package (van Dokkum 2001) as described by Koen et al. (2017). The one-dimensional wavelength-calibrated and sky-subtracted spectra were extracted using the APALL task. These were rectified using low-order polynomials fitted to regions of continuum identified automatically. The three segments from both observations at both grating angles were merged using weights based on the number of photons detected in each segment. The wavelengths of each spectrum were adjusted to correct for Earth motion.

2.4 The Drilling sample

The complete sample of normalised spectra used by D13 (the ‘Drilling sample’) has been used to validate the classification procedure.

2.5 Nomenclature

The SALT sample is described in Table 3, which gives positions (J2000.0), Gaia magnitudes, names, and classifications. By convention, we adopt the catalogue name at which the star was first identified as a helium-rich subdwarf. Other catalogues which include the star are indicated by abbreviation; a full list is available for each star from SIMBAD (Wenger et al. 2000). For brevity, we have contracted BPS CS to BPS and, except in Table 3, the full GALEX identifier to GLX Jhhmm+ddmm, with positions rounded down to tenths of a minute in right ascension and arcminutes in declination.

¹ <http://pysalt.salt.ac.za>

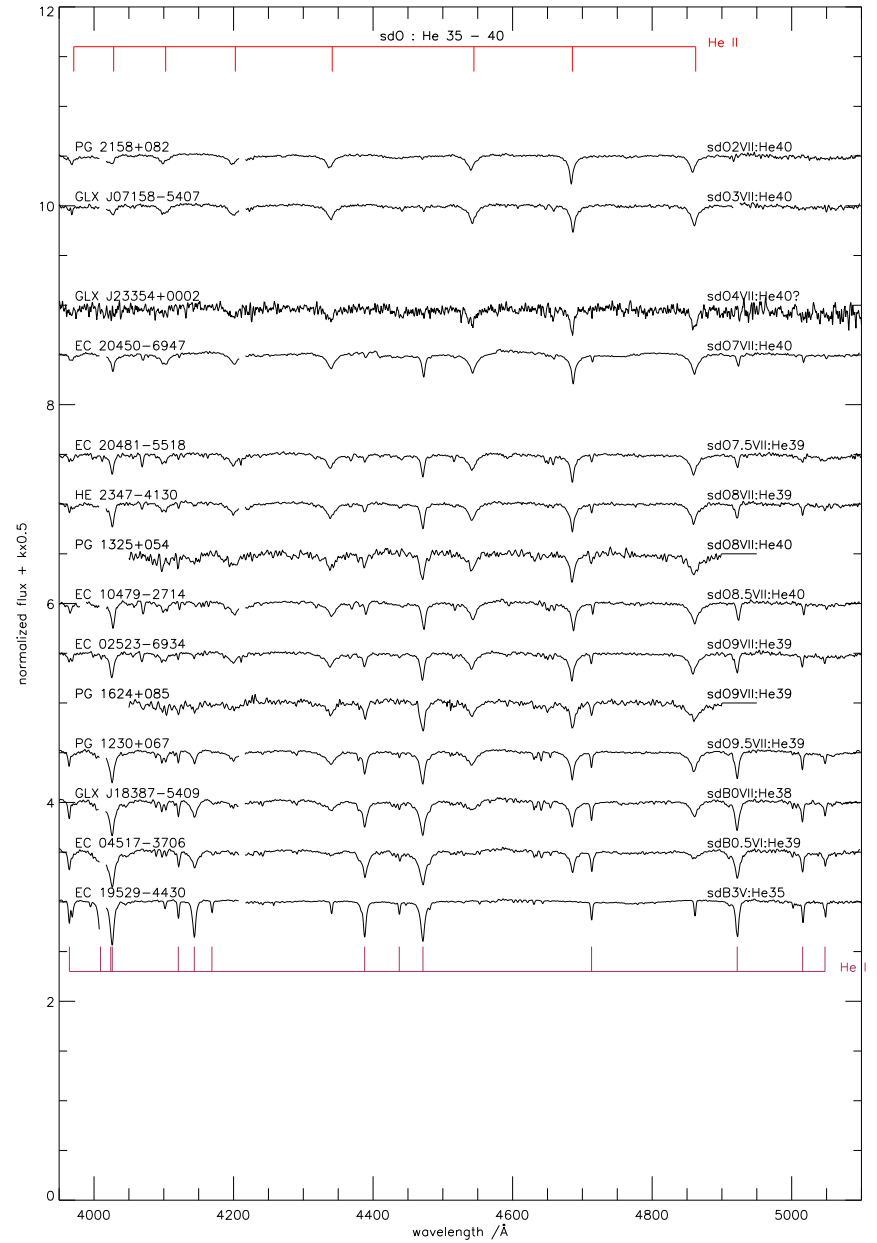
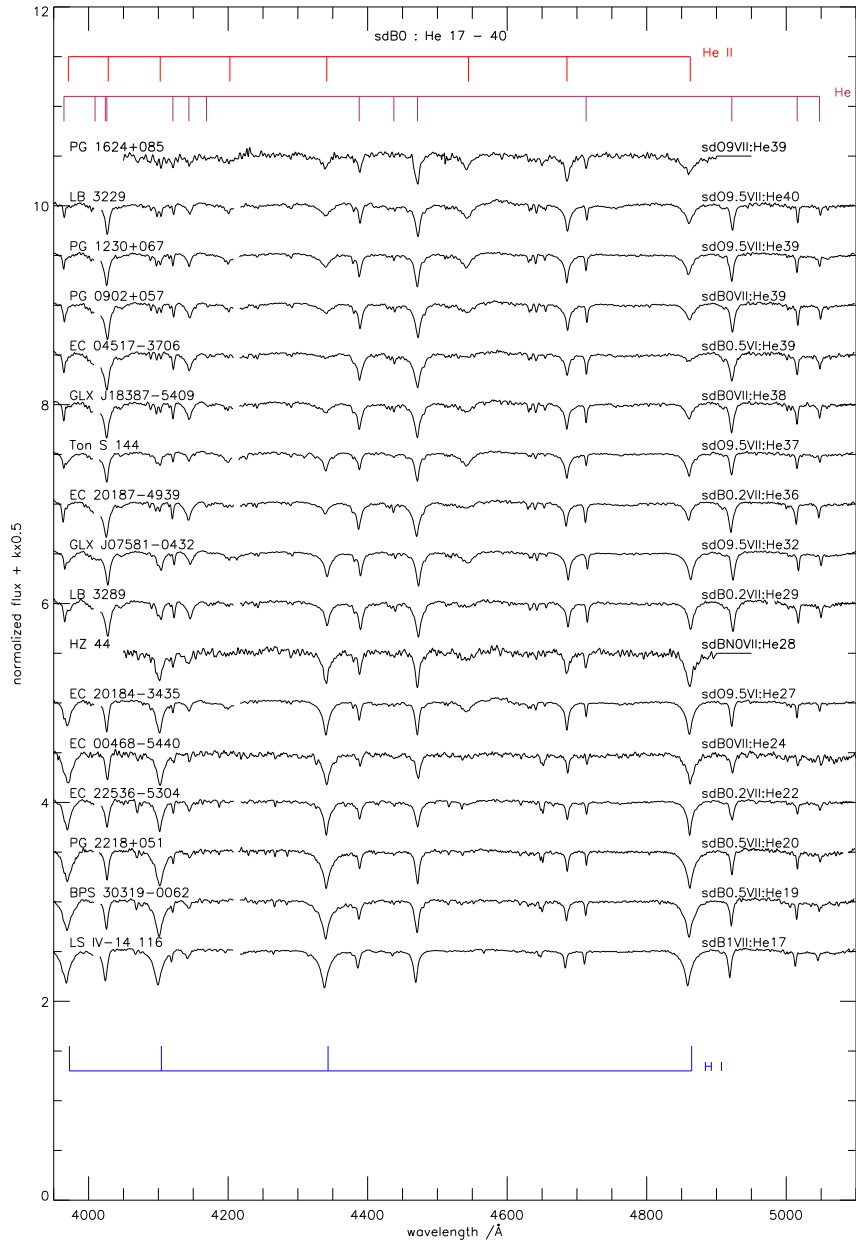


Figure 2. SALT atlas of early-type helium-rich hot subdwarfs showing (left) helium classes from He17 to He40 at spectral type around sdB0 and (right) spectral types from sdO2 to sdB3 with helium class 38 – 40 that do not show strong C or N lines. Principal lines are indicated in colour. In some cases star names are obvious contractions of names given in Table 2. Bold labels and spectra represent standards from D13.

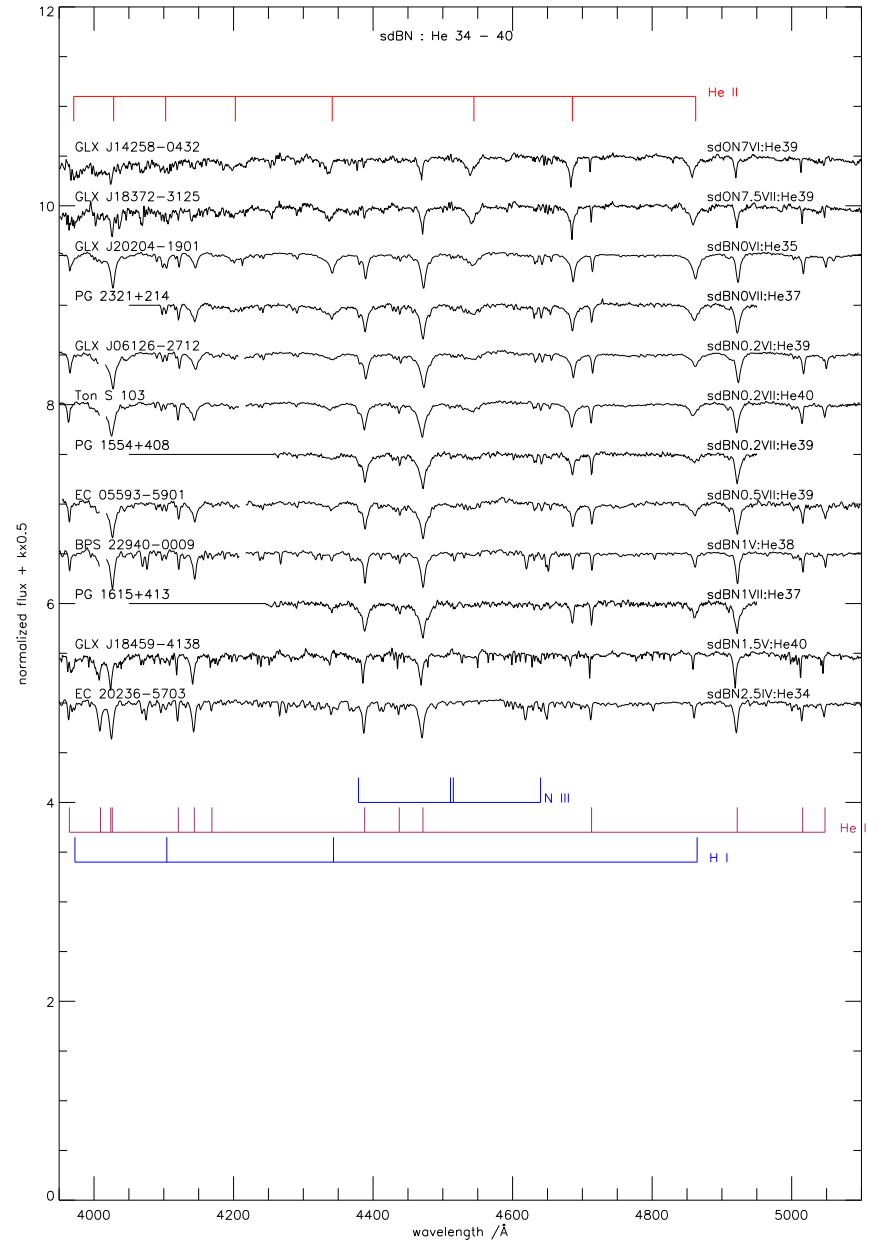
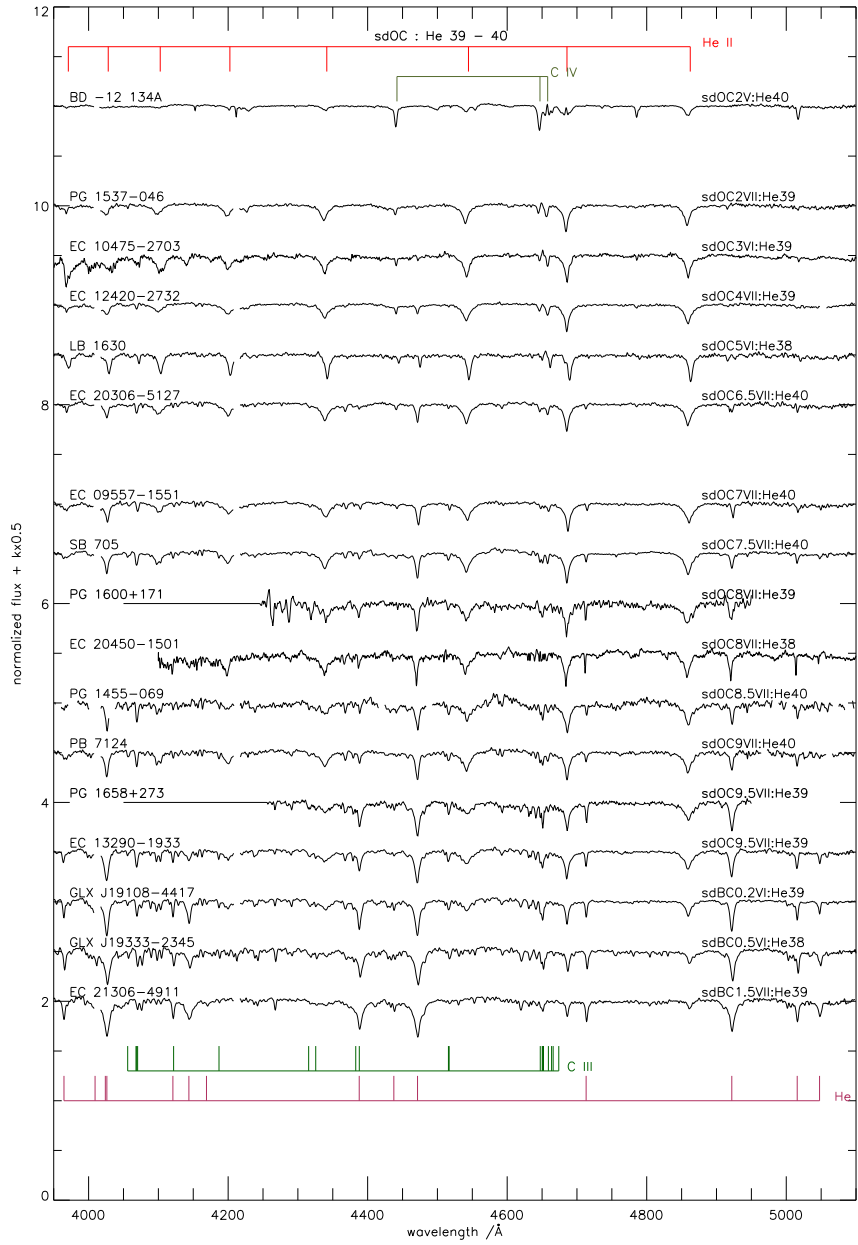


Figure 3. As Fig. 2 for (left) C-rich subdwarfs with spectral types from sdOC2 to sdBC1.5 with helium class 38 – 40 and (right) N-rich subdwarfs with spectral types from sdON7 to sdBN2.5 with helium class 34 – 40.

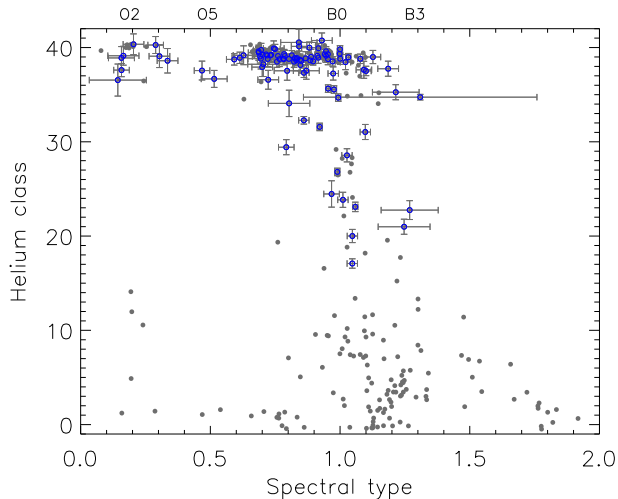


Figure 4. The Sp – He classification diagram for helium-rich subdwarfs (blue circles). The distribution from D13 is shown by grey dots; a uniform jitter covering \pm half a division has been applied to both datasets in both axes.

Table 2. Line depth criteria for He-strong stars to be sub-classified C or N.

C	C _{IV} 4658 4442	$d > 0.08$
C	C _{III} 4647 4650	$d > 0.10$
C	C _{II} 4267 4619	$d > 0.13$
N	N _{III} 4379 4513 4640	$d > 0.09$
N	N _{II} 4530 4447	$d > 0.20$ & $Sp > 1.0$

3 CLASSIFICATION

3.1 Method

Classification using the D13 system gives proxies for effective temperature T_{eff} (spectral type), surface gravity g (luminosity class), and helium / hydrogen ratio y (helium class). The criteria for spectral type and helium class are based on relative line strengths and depths assuming a spectral resolution $R \approx 2000$. Both HRS and RSS spectra are therefore degraded to this resolution for classification.

Spectral type, luminosity class and helium class are evaluated numerically from the digital spectra. For helium class (He) formulae based on fractional line depths d are given by D13:

$$\text{He} < 20 : \quad \text{He} = 20 * (d_{4471} + d_{4541}) / (d_{\gamma} - 0.83d_{4541})$$

$$\text{He} \geq 20 : \quad \text{He} = 40 - 20 * (d_{\gamma} - 0.83d_{4541}) / (d_{4471} + d_{4541})$$

Spectral types (Sp) for helium-rich classes are based on HeI/HeII line ratios as follows:

$$d_{4686} \geq d_{4471} : \text{Sp} = 0.1 + 0.8d_{4471} / d_{4686},$$

$$d_{4686} < d_{4471} : \text{Sp} = 0.9 + 0.4(1 - d_{4686} / d_{4471}).$$

Sp corresponds to a numerical scale on which spectral type O2 = 0.2, O5 = 0.5, B0 = 1.0, etc. D13 derived spectral types for hydrogen-rich classes using the depths of H β (d_{β}) and H γ (d_{γ}). For helium classes He < 12 and spectral types later than O8, we define:

$$\text{Sp} = ((3.8d_{\gamma} - 0.5) + (4.8d_{\beta} - 0.8)) / 2.$$

Luminosity classes are harder to quantify from simple line criteria. Line widths for gravity-sensitive lines were calibrated against spectral

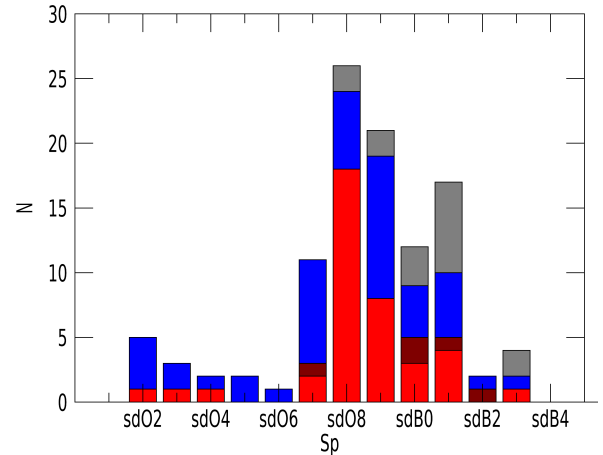


Figure 5. The distribution of SALT helium-rich subdwarf stars by spectral type. Coloured segments represent stars in helium class $\text{He} \geq 35$, subdivided into carbon-rich (C: blue), nitrogen-rich (N: maroon) and no qualification (red). Stars with $\text{He} < 35$ are enumerated in grey. The total number of stars in the sample is 106.

type and helium class using the sample of spectra from D13, and used with partial success.

Criteria for identifying carbon- and nitrogen-strong spectra were established by measuring depths of carbon and nitrogen lines for stars identified as sdOC and sdBN by D13. Criteria valid for He-strong spectra ($\text{He} > 25$) are summarized in Table 2

Errors are based on the signal-to-noise in each spectrum estimated from a region of continuum and then propagated formally through the line depth formulae.

Figures comparing automatic classification of the Drilling sample with the D13 manual classifications are shown in Appendix A.

3.2 Results

To achieve sufficient signal-to-noise for subsequent analysis, spectra for several stars were obtained over more than one observing block. Originally, the reduced spectrum from each block was classified as a separate spectrum, which gave a good indication of the errors associated with noise. The final classification was obtained from a single spectrum constructed from all SALT/RSS observations combined. Where an RSS spectrum was not available, the weighted average HRS spectrum was degraded by convolution with a Gaussian FWHM = 1.2\AA . This is essential because the relative depths of broad and sharp lines change with spectral resolution. Final classifications are shown in Table 3. The prefix ‘sd’ implies a D13 classification as distinct from an MK classification; it does not of itself imply that the object is a subdwarf. Fig. 4 shows the spectral-type helium-class distribution obtained from automatic SALT classifications. The distribution of the sample by spectral type is shown in Fig. 5. Both Figs. 4 and 5 suggest a break in the distribution at spectral type sdO6. One may identify a minimum of three groups containing stars with: a) spectral type earlier than sdO6 (all have helium class ≥ 35), b) helium class < 35 (and spectral types between sdO9 and sdB1), and c) those having helium class ≥ 35 and spectral type between sdO6 and sdB3. These groups include all but two or three outliers. By further considering the luminosity class, it may be shown that other groups exist.

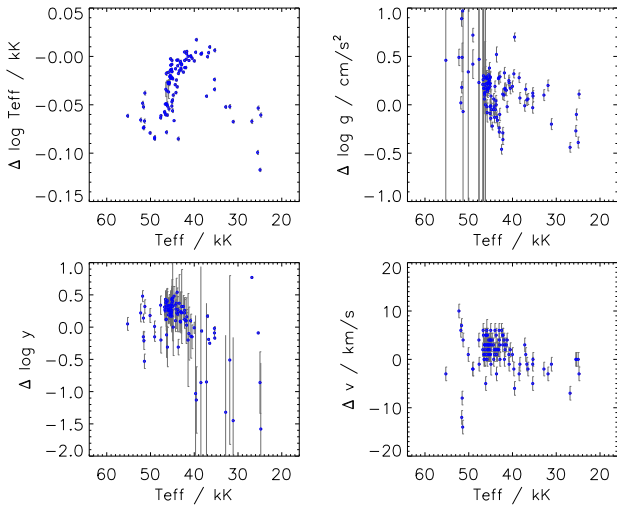


Figure 6. Residuals in the sense *salt_p00* – *XTgrid* for T_{eff} , $\log g$, $\log y$ and v as functions of T_{eff} . Offscale error bars are due to fit failures with *salt_p00* at high T_{eff} and with *XTgrid* at low T_{eff} and y .

However, errors currently associated with the luminosity criteria determine that other physical characteristics associated with the spectra should be examined first.

Although there are 58 stars with $\text{He} \geq 15$ in D13, only 7 are common to the SALT sample. The majority of the D13 sample are northern hemisphere stars. The latter range from spectral type sdO2 to sdB1, from luminosity class VI to VIII, and from helium class He18 to He40. In six, the differences are less than one subclass in spectral type, luminosity class and helium class. The seventh is sdO2 in D13 and sdO4 here.

4 PHYSICAL PROPERTIES

4.1 Model atmospheres

An alternative to classification is to match observed spectra within a grid of theoretical spectra (models) in order to estimate physical properties pertaining to the atmosphere of each star. Here, these comprise the star’s effective temperature T_{eff} , surface gravity g and $y \equiv n_{\text{He}}/n_{\text{H}}$, the ratio of hydrogen to helium atoms by number.

Ideally, such models should also match the abundances of other significant chemical species, carbon, nitrogen and iron all having significant effects on the stellar spectrum. To minimize computational costs, the present study considers only the following grids:

salt_p00: models were computed with the Armagh LTE radiative transfer package LTE-CODES (Jeffery et al. 2001; Behara & Jeffery 2006) on a grid²:

$$\begin{aligned} T_{\text{eff}}/\text{kK} &= [08(01)16(02)40(02.5)55], \\ \log g/\text{cm s}^{-2} &= [1.50(0.25)6.50], \\ n_{\text{He}} &= [0.01, 0.05, 0.10, 0.3, 0.5, 0.7, 0.8, 0.9, 0.99, 1.0]. \end{aligned}$$

Emergent spectra were computed on a self-adapting wavelength grid which optimally samples the local opacity structure and yields between 50 000 and 200 000 wavelength points in the range 3500 –

6800 Å. The abundance distribution for elements heavier than helium based was assumed to be solar; hence the label p00 which is shorthand for +0.0 dex. In the course of this investigation, it was realised that the abundance normalisation within STERNE, the model atmosphere component of LTE-CODES, assumed conservation of relative number fractions for metals when replacing hydrogen by helium. It is more natural that relative *mass fractions* should be conserved following, say, the fusion of 4 protons to a ${}^4\text{He}$ nucleus. STERNE was consequently modified and the entire model grid, currently comprising ~ 4000 models for a single metallicity and microturbulent velocity (v_{turb}), was recomputed. For the latter, $v_{\text{turb}} = 0 \text{ km s}^{-1}$ was assumed for both the calculation of line opacities in the model atmosphere (which affects the temperature stratification of the models) and for the formal solution, which affects relative line strengths and widths. For comparison with the SALT RSS spectra, a subset of these models having

$$T_{\text{eff}}/\text{kK} = [20, 24, 28, 32, 36, 40, 42.5, 45, 47.5, 50, 55],$$

$$\log g/\text{cm s}^{-2} = [3.0, 3.5, 4.0, 4.5, 5.0, 5.5, 6.0, 6.5],$$

$$n_{\text{He}} = [0.3, 0.5, 0.7, 0.9, 0.99, 1.0]$$

was sampled over the wavelength interval 3600–5200Å on an interval 0.2Å.

XTgrid: models computed with the non-LTE radiative transfer codes TLUSTY and SYNSPEC (Hubeny et al. 1994) for the analysis of hot subdwarfs observed in the Sloan Digital Sky Survey (Vennes et al. 2011; Németh et al. 2012) were made available by Németh et al. (2014)³. The original grid⁴ was defined as

$$\begin{aligned} [T_{\text{eff}}/\text{kK}, \log g/\text{cm s}^{-2}, \log y] \\ = [20(1)56, 5.0(0.1)6.2, -5.0(0.3) + 2.0], \end{aligned}$$

with no contribution from elements heavier than helium, and a microturbulent velocity $v_{\text{turb}} = 0 \text{ km s}^{-1}$ throughout. This grid contains some 1390 model spectra each computed on a wavelength range 3130 – 7530 Å with typically 38 000 wavelength points. To conserve memory a subset having

$$T_{\text{eff}}/\text{kK} = [24, 28, 32, 36, 40, 44, 48, 52, 56],$$

$$\log g/\text{cm s}^{-2} = [5.0, 5.3, 5.6, 5.9, 6.2],$$

$$\log y = [-1.0, -0.4, +0.2, +0.8, +1.4, +2.0]$$

was sampled over the wavelength interval 3600–5200Å on an interval 0.2Å (as above).

Ideally, the model atmosphere and emergent spectrum would be adapted and iterated to match the heavy-element distribution, and microturbulent velocity measured on a first iteration, since these strongly influence the atmosphere structure at low hydrogen abundances. At present, a full fine analysis is only practical for limited numbers of stars. For this paper, only approximate values are required in order to identify overall trends and stars of interest for further analysis. The LTE approximation is known to break down increasingly for stars with $T_{\text{eff}} \geq 30\,000 \text{ K}$, but is less important than the contribution of metal opacities otherwise (Anderson & Grigsby 1991; Löbbling 2020). These systematics are also discussed for restricted cases by Napiwotzki (1997); Latour et al. (2011); Pereira (2011); Latour et al. (2014) and Schindewolf et al. (2018b). Chemical stratification due to radiative levitation provides an additional vector of free parameters not considered in the current models (Behara & Jeffery 2008).

³ http://stelweb.asu.cas.cz/~nemeth/work/sd_grid/

⁴ described by three parameters $[p_1, p_2, p_3]$ and three triplets $p_{\text{min}}(\delta p)p_{\text{max}}$ implying $p \in p_{\text{min}}, p_{\text{min}} + \delta p, p_{\text{min}} + 2\delta p, \dots, p_{\text{max}}$.

² <http://193.63.77.2:2805/~SJeffery/m45.models/index.html>

Table 3. Fundamental data and classifications for helium-rich hot subdwarfs observed with SALT.

FUNDAMENTAL DATA			NAMES		LORES		SALT		CLASS	Notes
α_{2000}	δ_{2000}	m_G	Adopted	Other	Class	Ref				
00:10:07	-26:12:56	12.8	Ton S 144	PHL, SB, FB, MCT, BPS, EC	HesdB	EC5	RSS	HRS	sdO9.5VII:He37	
00:18:53	-31:56:02	14.4	Ton S 148	PHL, HE, MCT, GLX, EC	HesdB	EC5	RSS	HRS	sdBC0.2VI:He37	
00:49:05	-54:24:39	16.2	EC 00468-5440		HesdB	EC5	RSS		sdBC0VII:He24	
01:16:53	-22:12:09	14.8	BPS 22946-0005	MCT	B, pAGB	BPS	RSS		sdB2.5II:He24	
01:43:08	-38:33:16	13.0	SB 705	GLX, EC	HesdO	ki189	RSS	HRS	sdOC7.5VII:He40	
01:47:17	-51:33:39	13.5	LB 3229	JL, GLX	HesdO	ki189	RSS	HRS	sdO9.5VII:He39	
02:10:54	+01:47:47	13.7	Feiden 19	PB, PG, GLX	HesdO	moe90	RSS	HRS	sdO9VII:He37	D13
02:33:26	-59:12:31	15.1	LB 1630	EC	HesdO	EC5	RSS		sdOC5VI:He38	
02:43:23	+04:50:36	14.1	PG 0240+046	GLX	sdOB	PG	RSS	HRS	sdBC0.5VII:He25	D13
02:51:21	-72:34:33	14.6	LB 3289	EC, GLX	HesdO	EC3	RSS	HRS	sdB0.2VII:He30	
02:52:51	-69:22:34	16.1	EC 02523-6934		HesdO	EC4	RSS		sdO9VII:He39	
03:06:08	-14:31:52	15.6	PHL 1466	PB, EC	HesdO	EC5	RSS		sdOC4V:He40	noisy
03:50:38	-69:20:57	14.7	EC 03505-6929		HesdO	EC4	RSS		sdO9VII:He40	
04:03:05	-40:09:41	14.4	EC 04013-4017		HesdB	EC5	RSS	HRS	sdBC1VII:He32	
04:11:10	-00:48:48	14.1	GLX J041110.1-004848		HesdO	ØG	RSS	HRS	sdO8VII:He40	
04:13:19	-13:41:03	12.5	EC 04110-1348		HesdO	EC3	RSS		sdOC7.5VII:He39	
04:15:30	-54:21:59	14.9	HE 0414-5429	EC, GLX	HesdO	ØG	RSS		sdO8VII:He39	
04:20:35	+01:20:41	12.3	GLX J042034.8+012041		HesdO	ven11	RSS	HRS	sdOC8.5VII:He40	
04:22:37	-54:08:50	14.0	LB 1721	EC, GLX	HesdO	EC4	RSS		sdOC9VII:He38	
04:29:11	-29:02:48	14.1	EC 04271-2909	BPS, GLX	HesdO	BPS	RSS		sdO8.5VI:He39	
04:29:33	-47:31:44	15.8	EC 04281-4738	GLX	sdB?	EC4	RSS		sdOC6.5VII:He39	
04:36:15	-53:43:34	12.5	LB 1741	EC	HesdO	ki192	RSS		sdO9VII:He39	
04:37:34	-61:57:43	14.6	BPS 29520-0048	EC, GLX	HesdO	rod07	RSS		sdOC9VII:He39	
04:42:26	-32:06:01	14.8	EC 04405-3211	GLX	HesdO	EC4	RSS		sdO7.5VII:He39	
04:53:32	-37:01:43	15.7	EC 04517-3706		HesdB	EC3	RSS		sdB0.5VI:He40	
05:13:48	-19:44:18	15.1	GLX J051348.2-194417		HesdOB	ØG	RSS		sdO7.5VII:He39	
05:17:57	-30:47:50	13.3	Ton S 415	EC, GLX	HesdO	EC3	RSS	HRS	sdO8VII:He30	
05:26:12	-28:58:25	15.6	EC 05242-2900	GLX	HesdB	EC3	RSS		sdOC7VII:He39	
05:58:05	-29:27:09	15.2	GLX J055804.5-292708		HesdOB	ØG	RSS		sdOC7VII:He39	
06:00:01	-59:01:03	16.1	EC 05593-5901		HesdB	EC3	RSS		sdBN0.5VII:He39	
06:12:37	-27:12:55	13.4	GLX J061237.5-271254		HesdOB	ØG	RSS	HRS	sdBN0.2VI:He40	
07:07:39	-62:22:41	14.5	GLX J070738.9-622241		HesdOB	ØG	RSS	HRS	sdOC6.5VII:He40	
07:15:50	-54:07:57	14.4	GLX J071549.6-540755		HesdO	ØG	RSS	HRS	sdO3VII:He40	
07:58:08	-04:32:05	13.1	GLX J075807.5-043203		HesdO	nem12	RSS	HRS	sdO9.5VII:He33	
08:35:24	-01:55:53	11.4	[CW83] 0832-01		sdOp	CW83	RSS		sdO8VII:He40	
08:45:29	-12:14:10	14.0	GLX J084528.7-121410		HesdOB	ØG	RSS	HRS	sdOC9.5VI:He39	
09:05:05	+05:33:01	14.1	PG 0902+057	GLX	sdOD	PG	RSS	HRS	sdB0VII:He39	D13
09:07:08	-03:06:14	11.9	[CW83] 0904-02		sdOp(He)	ber80	RSS		sdO7.5VI:He39	
09:18:56	-57:04:25	12.9	LSS 1274		HesdO	ØG	RSS		sdOC8VI:He39	
09:58:11	-16:05:52	14.3	EC 09557-1551	BPS, GLX	HesdO	EC2	RSS		sdO7VII:He40	
10:00:43	-12:05:59	14.0	PG 0958-119	HE, EC, GLX	HesdO	EC2	RSS		sdO8VI:He39	
10:49:55	-27:19:09	13.4	EC 10475-2703	GLX	HesdO	EC2		HRS	sdOC3VII:He39	
10:50:18	-27:30:37	13.9	EC 10479-2714	GLX	HesdO	EC2	RSS		sdO8.5VII:He40	
11:26:11	-20:01:39	14.4	EC 11236-1945	GLX	HesdO	EC2	RSS		sdOC2VII:He40	
11:30:04	+01:37:37	13.8	PG 1127+019	GLX	sdOD	PG	RSS	HRS	sdOC9.5VII:He39	D13
12:22:59	-05:53:05	14.7	PG 1220-056	GLX	sdOC	PG	RSS		sdO4VII:He39	D13
12:33:23	-06:25:18	13.1	PG 1230+067	GLX		PG	RSS		sdON9.5VII:He39	D13
12:37:35	-28:41:01	14.8	EC 12349-2824	GLX	HesdO	EC2	RSS		sdO8VII:He40	
12:44:42	-27:48:58	14.7	EC 12420-2732	GLX	HesdO	EC2	RSS		sdOC4VII:He40	
13:20:44	+05:59:01	14.7	PG 1318+062		sdOC	PG	RSS	HRS	sdOC9VII:He39	
13:31:46	-19:48:26	14.4	EC 13290-1933	GLX	HesdB	EC2	RSS		sdOC9.5VII:He39	sen15
14:25:50	-04:32:33	14.0	GLX J142549.8-043231		HesdOB	ØG		HRS	sdO9VII:He39	
14:57:57	-07:05:05	16.4	PG 1455-069		sdOB	PG	RSS		sdOC8.5VII:He40	
15:23:32	-18:17:26	13.9	GLX J152332.2-181726		HesdOB	ØG	RSS	HRS	sdCO9VII:He39	
15:30:56	+02:42:23	15.4	PG 1528+029	GLX	sdOC	PG	RSS		sdO8VII:He40	
15:37:40	-17:02:15	15.1	EC 15348-1652	GLX	HesdO	EC2	RSS		sdO8VII:He39	
15:40:33	-04:48:12	15.0	PG 1537-046	BPS, GLX	HesdO	PG	RSS		sdOC2VII:He40	D13
16:28:36	-03:32:38	15.5	PG 1625-034	BPS, GLX	HesdO	BPS	RSS		sdO8VII:He39	noisy
16:54:38	+03:18:47	15.1	GLX J165438.5+031847		HesdO	ØG	RSS		sdOC3VII:He40	
17:05:06	-71:56:09	13.8	GLX J170506.0-715609		HesdO	ØG	RSS	HRS	sdO7.5VII:He39	
18:32:32	-47:44:38	13.5	GLX J183231.7-474435		HesdOB	ØG		HRS	sdOC9VII:He38	
18:37:17	-31:25:16	13.9	GLX J183716.7-312514		HesdOB	ØG		HRS	sdO7.5VII:He39	

Table 3 – *continued*

FUNDAMENTAL DATA			NAMES		LORES		SALT		CLASS	Notes
α_{2000}	δ_{2000}	m_G	Adopted	Other	Class	Ref				
18:38:46	-54:09:34	13.6	GLX J183845.6-540935		HesdOB	ØG	RSS	HRS	sdB0VII:He39	
18:46:00	-41:38:28	14.6	GLX J184559.8-413827		HesdB	ven11	RSS	HRS	sdBN2V:He38	jef17
19:05:56	-44:38:40	13.6	GLX J190555.7-443838		HesdOB	ØG		HRS	sdO8.5VII:He39	
19:10:50	-44:17:14	12.9	GLX J191049.5-441713		HesdOB	ØG	RSS	HRS	sdBC0.2VI:He39	
19:11:09	-14:06:53	11.9	GLX J191109.3-140654		HesdO	ven11		HRS	sdOC6.5VII:He39	
19:15:04	-42:35:04	14.0	GLX J191504.3-423502		HesdOB	ØG	RSS	HRS	sdO8.5VII:He40	
19:33:24	-23:45:53	14.8	GLX J193323.6-234553		HesdOB	ØG	RSS		sdBC0.5VI:He38	
19:37:40	-43:03:56	13.4	GLX J193740.3-430356		HesdB	ØG	RSS	HRS	sdB2.5V:He21	
19:41:04	-52:46:57	15.7	BPS 22896-0128	EC	HesdO	BPS	RSS		sdOC7VII:He39	
19:56:31	-44:22:19	11.8	EC 19529-4430		B	EC3	RSS	HRS	sdB3IV:He35	metal poor
20:13:19	-12:01:18	13.8	GLX J201318.8-120119		HesdO	ØG	RSS	HRS	sdOC2VII:He37	
20:14:23	-37:15:42	13.4	EC 20111-3724	GLX	HesdO	EC3	RSS		sdO9VII:He33	
20:16:09	-68:53:33	15.9	EC 20111-6902	GLX	HesdB	EC3	RSS		sdBC1.5VII:He38	
20:20:26	-19:01:50	14.8	GLX J202026.0-190150		HesdOB	ØG	RSS		sdBN0VI:He35	
20:21:39	-34:25:46	14.4	EC 20184-3435	GLX	HesdO	EC3	RSS		sdO9.5VI:He28	
20:22:22	-49:29:40	13.4	EC 20187-4939	GLX	HesdB	EC3	RSS	HRS	sdB0.2VII:He36	
20:25:06	-08:04:18	13.9	GLX J202506.0-080419		HesdO	ØG	RSS	HRS	sdOC2VII:He39	
20:26:30	-62:40:07	14.1	EC 20221-6249	GLX	HesdO	EC3	RSS	HRS	sdOC9.5VII:He39	
20:27:37 ¹	-56:53:56 ¹	14.8 ¹	EC 20236-5703		H.def	EC3	RSS	HRS	sdBC2.5V:He35	
20:30:20	-59:50:39	14.0	BPS 22940-0009	EC, GLX	HesdB	BPS	RSS	HRS	sdBN1VI:He37	
20:34:21	-51:17:16	14.3	EC 20306-5127	GLX	HesdO	EC3	RSS	HRS	sdOC6.5VII:He39	
20:47:48	-14:50:27	13.9	EC 20450-1501	GLX	HesdB	EC3	RSS	HRS	sdO8.5VII:He38	
20:49:54	-69:36:31	14.7	EC 20450-6947		HesdO	EC3	RSS		sdO7VII:He40	
20:51:54	-55:07:34	15.6	EC 20481-5518	GLX	HesdO	EC3	RSS		sdO7.5VII:He40	
20:57:38	-14:25:44	13.0	LS IV-14 116	GLX, EC	HesdO	vit91	RSS		sdB1VII:He18	D13, nas11
21:01:30	-56:29:43	16.2	EC 20577-5641	GLX	HesdB/O	EC3	RSS			noisy
21:04:18	-27:11:43	15.2	Ton S 14	EC	HesdO	EC3	RSS		sdOC9VII:He40	
21:11:11	-48:02:57	15.3	EC 21077-4815		HesdO	EC4	RSS		sdOC7.5VII:He39	
21:11:21	-23:48:14	14.4	BPS 30319-0062	GLX, EC	HesdOB	BPS	RSS	HRS	sdB0.5VII:He20	
21:17:09	-70:01:04	14.1	EC 21125-7013	GLX	HesdO	EC3	RSS		sdOC6.5VII:He40	
21:33:58	-48:58:03	15.1	EC 21306-4911	GLX	HesdB	EC4	RSS		sdBC1VII:He40	
21:44:38	-36:31:47	15.3	EC 21416-3645		HesdO	EC4	RSS		sdO8.5VII:He34	
21:47:52	-12:35:44	14.5	PHL 149	BPS, GLX, EC	HesdO	BPS	RSS		sdO7.5VII:He40	
21:51:13	-21:07:04	13.0	PHL 178	EC	HesdO	kil89	RSS		sdO7.5VII:He40	
22:01:02	+08:30:48	13.1	PG 2158+082	GLX	HesdO	PG	RSS		sdO2VII:He40	D13
22:14:58	-63:41:45	14.5	BPS 22956-0090	GLX	HesdB	BPS	RSS	HRS	sdO9VII:He40	
22:16:04	-17:19:47	14.6	BPS 22892-0051	GLX, EC	HesdO	BPS	RSS		sdOC7VII:He40	
22:17:22	-05:27:50	14.3	PB 7124	GLX	HesdOB	ØG	RSS		sdOC9VII:He40	
22:19:02	-41:23:32	13.9	BPS 22875-0002	GLX, EC	HesdO	BPS	RSS	HRS	sdOC9VII:He40	
22:21:23	+05:24:58	15.3	PG 2218+052		HesdB	PG	RSS		sdB0.5VII:He21	
22:36:50	-68:22:20	16.1	EC 22332-6837	GLX	HesdO	EC4	RSS		sdO7.5VII:He37	
22:52:20	-63:15:55	15.3	BPS 22938-0044	GLX, EC	HesdB	BPS	RSS		sdO7.5VII:He40	
22:56:36	-52:48:36	13.3	EC 22536-5304	GLX	sdB	EC5	RSS	HRS	sdB0.2VI:He23	
23:10:54	-63:03:25	14.3	BPS 22938-0073	GLX	HesdO	BPS	RSS	HRS	sdO7.5VII:He39	
23:29:10	-10:06:06	13.3	PHL 540	GLX	sdO	kil88	RSS		sdO7.5VII:He40	
23:34:02	-28:51:38	14.7	Ton S 103	FB, PHL, BPS, GLX	HesdB	BPS	RSS	HRS	sdBN0.2VII:He40	
23:35:41	+00:02:19	15.9	PB 5462	PG, BPS, GLX	HesdO	BPS	RSS			noisy
23:50:20	-41:14:02	15.3	HE 2347-4130	GLX, EC	HesdO	str07	RSS		sdO8VII:He39	
02:53:08	-70:58:56	16.1	EC 02527-7111		HesdB	EC4	RSS		DB	
04:32:14	-16:45:09	15.4	EC 04299-1651	HE	HesdB	EC2	RSS	HRS	DB+dM	vos07
19:31:57	-58:22:45	16.6	EC 19277-5829		HesdB	EC2	RSS		DB	
20:36:46	-25:14:41	15.1	EC 20337-2525		HesdB	EC3	RSS		DB	
22:23:58	-25:10:44	16.4	EC 22211-2525	GLX	HesdB	EC5	RSS		DB	

Fundamental Data: α_{2000} , δ_{2000} , m_G : Gaia Collaboration (2018), 1: EC3 (m_V).

Selected catalogues: BPS=Beers et al. (1992), [CW83]=Carnochan & Wilson (1983), EC = EC n : $n = 1, 5$ =Stobie et al. (1997b); Kilkeny et al. (1997); O'Donoghue et al. (2013); Kilkeny et al. (2015, 2016), Feige=Feige (1958), FB=Greenstein & Sargent (1974), GLX=Bianchi et al. (2017), HE=Wisotzki et al. (1996), JL=Jaidee & Lyngå (1969), KUV=Kondo et al. (1984), LB=(Luyten 1953, et seq.), LSIV=Nassau & Stephenson (1963), LSS=Stephenson & Sanduleak (1971), MCT=Demers et al. (1990), PB=Berger & Fringant (1980a), PG=Green et al. (1986), PHL=Haro & Luyten (1962), SB=Slettebak & Brundage (1971), Ton S=Chavira (1958), UVO=Carnochan & Wilson (1983)

LORES references: as above plus ber80=Berger & Fringant (1980b), ØG=Østensen (2006); Geier et al. (2017), kil89=Kilkeny & Muller (1989), kil92=Kilkeny & Busse (1992), lam00=Lamontagne et al. (2000), moe90=Moehler et al. (1990a), rod07=Rodríguez-López et al. (2007), str07=Ströer et al. (2007), ven11=Vennes et al. (2011), vit91=Viton et al. (1991)

Notes. a CLASS has also given by: D13=Drilling et al. (2013), sen15=Şener-Şatir (2015), jef17=Jeffery (2017), nas11=Naslim et al. (2011) vos07=Voss et al. (2007); metal poor = very weak metal lines; noisy = too noisy to classify.

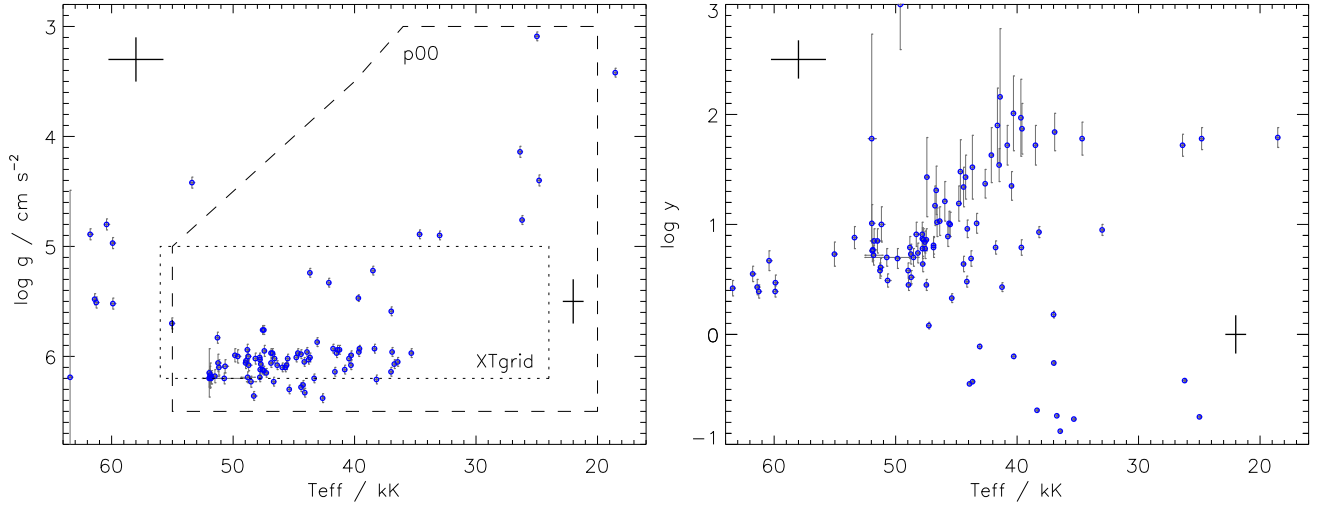


Figure 7. $T_{\text{eff}} - \log g$ (left) and $T_{\text{eff}} - \log y$ (right) diagrams for helium-rich subdwarfs from the SALT sample obtained from the *salt_p00* model grid. The long-dashed line shows the boundary of the LTE solar-mix grid. The short-dashed line shows the boundary of the non-LTE zero-metal grid (Németh et al. 2012). Gray error bars associated with each datum are formal errors as given in Table 4. Stars with $\delta \log g > 2$ are omitted. Dark error bars upper-left and lower-right represent estimated mean observational errors (see text).

4.2 Method

LTE_CODES include the optimization code SFIT (Jeffery et al. 2001). Here we use the Levenburg-Marquardt option to minimize the square residual between each observed normalized spectrum and the grid of models described above.

Before optimization, the radial velocity v_{rad} of the observed spectrum relative to the laboratory rest-frame is established by cross-correlation with a representative theoretical spectrum; the wavelengths of the observed spectrum are then corrected by this amount so that the radial velocity is not a free parameter of the fit.

Inputs to the optimization include the normalized spectrum shifted to the local rest-frame velocity, a definition of regions of spectrum representative of continuum, masks to exclude non-stellar features (e.g. interstellar calcium H and K), masks to give additional weight to key lines, full-width half-maximum for the instrumental broadening profile (1.25 \AA), and a threshold for excluding cosmic-ray features ($1.5 \times \text{continuum}$). Regions of spectrum weighted 10 times other regions included $\text{H}\beta$, $\text{H}\gamma$, He II 4686 and 4540 \AA , He I 4471, 4381, 4121, 4144 and 4169 \AA .

The initial optimisation commences with starting values for $T_{\text{eff}} = 33.0 \text{ kK}$, $\log g / \text{cm s}^{-2} = 4.9$, $n_{\text{He}} = 0.9$ and with the projected rotation velocity fixed at $v \sin i = 0$. Two renormalization steps are carried out using the high-pass procedure outlined by Jeffery et al. (1998), with filter widths set at 200 \AA and 50 \AA respectively. An optimization step is carried out after each renormalization; for the second of these $v \sin i$ is free.

Outputs from the optimization include T_{eff} , $\log g$, n_{He} (or equivalently, $\log y = n_{\text{He}}/n_{\text{H}}$), and $v \sin i$, as well as the renormalized observed and best-fit model spectra. v_{rad} determined prior to optimization is included in the overall set of outputs.

Various sets of starting values for T_{eff} , $\log g$, and n_{He} were investigated. The adopted values were chosen because a converged solution was obtained in all cases. Choosing T_{eff} too high or too low yielded consistent solutions in some fraction of cases, but also led to divergence for a fraction of late or early-type spectra, respectively.

Care is required in the choice of template used to determine v_{rad} ,

especially for very hot stars. Because of the offset between hydrogen Balmer lines and He II lines, a template helium-hydrogen ratio which does not match the observed spectrum produces a systematic velocity shift and hence degrades the model optimisation. A second iteration was therefore introduced in which the first best-fit model was used as the velocity template, the second v_{rad} measurement being retained.

From experience, the zero-points for both RSS and HRS wavelength calibrations must be treated with caution. Undocumented evidence for seasonal drifts might be associated with thermal drift in RSS, which sits on the tracker some 15 m above the primary mirror assembly. Early implementations of the HRS calibration pipeline suffered zero-point errors (Crawford, private communication). Consequently individual measurements of v_{rad} should be treated with caution. Excessively high values may indicate an object of interest.

Since $v \sin i$ is an output from SFIT, and required to ensure the solution is self-consistent, it has a lower limit represented by the instrumental resolution. For RSS spectra, $c/R \approx 83 \text{ km s}^{-1}$. For stars with $T_{\text{eff}} \geq 50 \text{ kK}$, there are no sharp lines in the zero-metal models with which to constrain the rotational broadening; hence $v \sin i$ is degenerate with $\log g$. For the sample of 71 RSS spectra with $T_{\text{eff}} < 50 \text{ kK}$, $\langle v \sin i \rangle = 83 \pm 22 \text{ km s}^{-1}$, all except EC 20111–6902 have $v \sin i < \langle v \sin i \rangle + 2\sigma$.

For the HRS spectra, the nominal $c/R \approx 7 \text{ km s}^{-1}$ was degraded by resampling so that the mean $\langle v \sin i \rangle = 12 \pm 2 \text{ km s}^{-1}$ obtained for four (excluding EC 10475–2703) using the line-blanketed LTE models is satisfactory. Again the absence of sharp lines in the high- T_{eff} zero-metal models required that $v \sin i = 12 \text{ km s}^{-1}$ be fixed for the final fits.

4.3 Results

Values for T_{eff} , $\log g$ and $\log y$ obtained for the full sample are shown in Table 4. Results lying outside respective grid boundaries are included for completeness. It is emphasized that these analyses have been carried out for the purpose of data exploration and discovery; their used in detailed investigations of individual stars may be ill advised.

Table 4. Atmospheric parameters for helium-rich hot subdwarfs observed and classified with SALT/RSS. Stars observed only with SALT/HRS are marked ‘*’, σ represents standard deviation of fluxes about the mean in a continuum region $\lambda 4810 - 4845 \text{ \AA}$ (i.e. $\sigma = 0.01 \Rightarrow \text{S/N} = 100$.) All errors are formal; rather, mean errors $\delta T_{\text{eff}}/T_{\text{eff}} \approx \pm 0.028$, $\delta \log g \approx \pm 0.27$, $\delta \log y \approx \pm 0.29$, and $\delta v_{\text{rad}} \approx \pm 3.0 \text{ km s}^{-1}$ should be adopted (§ 4.3). For cases where SFIT finds $n_{\text{He}} \geq 1$, we set $n_{\text{He}} = 1$ and $\log y = 3$. Tests suggest $\langle \delta v_{\text{rad}} \rangle \approx \pm 3 \text{ km s}^{-1}$ (see text). v_{wid} is a nominal measure of the line broadening, dominated by the instrumental width $c/R \approx 83 \text{ km s}^{-1}$ (RSS) (see text); a smaller value $\sim 12 \text{ km s}^{-1}$ is indicated where only an HRS spectrum is available (marked †).

Star	Class	σ	T_{eff} kK	$\log g$ cm s^{-2}	$\log y$	n_{He}	v_{rad} km s^{-1}	v_{wid} km s^{-1}	grid
Ton S 144	sdO9.5VII:He37	0.010	43.79±0.07	6.03±0.04	0.69±0.07	0.83±0.03	−17	87	xt
Ton S 148	sdBC0.2VI:He37	0.012	38.49±0.09	5.22±0.04	1.72±0.18	0.98±0.01	159	109	p00
EC 00468–5440	sdBC0VII:He25	0.020	38.36±0.10	5.93±0.04	−0.69±0.01	0.17±0.02	57	117	p00
BPS 22946–0005	sdB2.5II:He24	0.010	24.99±0.11	3.09±0.04	−0.75±0.01	0.15±0.03	−64	102	p00
SB 705	sdOC7.5VII:He40	0.013	48.72±0.20	6.08±0.05	0.52±0.06	0.77±0.03	−14	65	xt
LB 3229	sdO9.5VII:He39	0.012	44.10±0.08	† 6.33±0.04	0.96±0.08	0.90±0.02	48	79	xt
Feige 19	sdO9VII:He37	0.017	44.14±0.08	6.05±0.04	0.48±0.05	0.75±0.03	19	61	xt
LB 1630	sdOC5VI:He38	0.020	53.39±0.15	† 4.42±0.05	0.88±0.10	0.88±0.03	233	105	xt
PG 0240+046	sdBC0.5VII:He25	0.011	37.00±0.09	6.14±0.04	0.18±0.03	0.60±0.02	52	105	p00
LB 3289	sdBN0.2VII:He29	0.013	39.65±0.10	5.96±0.04	0.79±0.07	0.86±0.02	98	92	p00
EC 02523–6934	sdO9VII:He39	0.013	46.37±0.10	6.08±0.04	1.03±0.13	0.91±0.02	−44	80	xt
EC 03505–6929	sdO9VII:He40	0.018	45.51±0.10	6.02±0.04	1.00±0.11	0.91±0.02	−2	71	xt
EC 04013–4017	sdBC1VII:He32	0.012	38.20±0.10	† 6.21±0.04	0.93±0.05	0.89±0.01	9	94	p00
GLX J04111–0048	sdO8VII:He40	0.017	46.88±0.10	5.97±0.04	0.79±0.09	0.86±0.03	41	74	xt
EC 04110–1348	sdOC7.5VII:He39	0.013	48.94±0.18	6.04±0.05	0.45±0.05	0.74±0.03	36	70	xt
HE 0414–5429	sdO8VII:He39	0.016	47.79±0.10	6.03±0.04	0.78±0.09	0.86±0.03	15	78	xt
GLX J04205+0120	sdOC8.5VII:He39	0.009	47.80±0.10	6.19±0.04	0.87±0.10	0.88±0.03	49	83	xt
LB 1721	sdOC9VII:He38	0.024	45.60±0.10	6.08±0.04	1.01±0.11	0.91±0.02	41	86	xt
EC 04271–2909	sdO8.5VI:He39	0.011	47.47±0.10	6.13±0.04	0.86±0.10	0.88±0.03	15	60	xt
EC 04281–4738	sdOC6.5VII:He39	0.027	52.97±0.13	6.07±4.32	0.68±0.09	0.83±0.04	64	78	xt
LB 1741	sdO9VII:He39	0.009	44.41±0.10	5.98±0.04	0.64±0.07	0.81±0.03	18	75	xt
BPS 29520–0048	sdOC9VII:He39	0.015	45.95±0.10	6.10±0.04	1.21±0.18	0.94±0.02	71	76	xt
EC 04405–3211	sdO7.5VII:He39	0.013	51.50±0.30	6.18±0.06	0.85±0.11	0.88±0.03	3	73	xt
EC 04517–3706	sdB0.5VI:He40	0.013	40.30±0.08	6.08±0.04	2.01±0.34	0.99±0.01	14	118	p00
GLX J05138–1944	sdO7.5VII:He39	0.036	48.53±0.38	† 6.23±0.05	0.70±0.08	0.83±0.03	−7	48	xt
Ton S 415	sdO8VII:He30	0.007	43.92±0.10	5.96±0.04	−0.45±0.01	0.26±0.02	233	85	xt
EC 05242–2900	sdO8VII:He28	0.008	43.67±0.10	6.01±0.04	−0.43±0.01	0.27±0.02	148	105	xt
GLX J05580–2927	sdOC7VII:He39	0.014	53.60±0.13	6.05±4.34	0.58±0.08	0.79±0.04	25	85	xt
EC 05593–5901	sdB0.5VII:He39	0.019	40.81±0.08	6.12±0.04	1.72±0.18	0.98±0.01	22	101	p00
GLX J06126–2712	sdB0.2VI:He40	0.010	41.62±0.06	6.14±0.04	1.90±0.34	0.99±0.01	85	76	xt
GLX J07076–6222	sdOC6.5VII:He40	0.009	53.62±0.13	6.02±4.53	0.58±0.08	0.79±0.04	3	85	xt
GLX J07158–5407	sdO3VII:He40	0.018	† 61.02±0.15	6.02±4.58	0.30±0.05	0.67±0.04	37	133	xt
GLX J07581–0432	sdO9.5VII:He33	0.009	41.24±0.07	5.94±0.04	0.43±0.04	0.73±0.02	107	78	xt
GLX J08454–1214	sdOC9.5VI:He39	0.008	43.68±0.08	5.24±0.04	1.52±0.29	0.97±0.02	113	77	xt
PG 0902+057	sdB0VII:He39	0.010	42.63±0.07	† 6.38±0.04	1.37±0.13	0.96±0.01	55	60	xt
UVO 0904–02	sdO7.5VI:He39	0.010	51.88±0.21	6.17±0.11	0.77±0.10	0.85±0.04	12	80	xt
LSS 1274	sdO8VI:He39	0.011	46.88±0.10	6.06±0.04	0.81±0.08	0.86±0.03	22	73	xt
EC 09557–1551	sdO7VII:He40	0.014	51.92±0.22	6.19±0.10	0.76±0.10	0.85±0.04	75	94	xt
PG 0958–119	sdO8VII:He39	0.013	47.57±0.11	5.76±0.04	0.78±0.09	0.86±0.03	40	61	xt
EC 10475–2703	sdOC3VI:He39 *	0.010	59.90±0.17	5.52±0.05	0.47±0.07	0.75±0.04	−8	! 12	xt
EC 10479–2714	sdO8.5VII:He40	0.014	47.59±0.10	6.12±0.04	0.84±0.10	0.87±0.03	89	73	xt
EC 11236–1945	sdOC2VII:He40	0.012	† 61.77±0.18	4.89±0.05	0.55±0.07	0.78±0.04	32	136	xt
PG 1127+019	sdOC9.5VII:He39	0.010	44.41±0.10	† 6.28±0.04	1.34±0.18	0.96±0.02	35	71	xt

*: HRS spectrum, †: extrapolated

Large errors in $\log y$ occur for stars with very low hydrogen abundances. The hydrogen abundance is difficult to measure precisely in hot helium-rich stars since the Balmer lines are completely dominated by the corresponding lines in the HeII Pickering series and, since $y \equiv n_{\text{He}}/n_{\text{H}}$, the increasing error in the smaller denominator dominates the error budget.

Table 4 also provides an estimate of the noise σ in the spectrum used for the analysis, the radial velocity v_{rad} of said spectrum, and the parameter obtained as $v \sin i$ in the model atmosphere fit, but more precisely labelled as a line width v_{wid} in velocity units.

Fig. E.1 in the Supplementary Material shows correlations between physical parameters and spectral class indicators. Trends illustrate the systematics, and scatter provides an estimate of the random errors.

For $T_{\text{eff}} \lesssim 35 \text{ kK}$, ($\text{Sp} \gtrsim \text{sdB1}$) stars have surface gravities outside the *XTgrid* boundary; the *salt_p00* grid results shown in Table 4 are to be preferred. For $42 \gtrsim T_{\text{eff}}/\text{kK} \gtrsim 35$ ($\text{sdO9} \lesssim \text{Sp} \lesssim \text{sdB1}$), both grids give comparable values for T_{eff} , with *salt_p00* giving slightly higher g (by 0 – 0.3 dex) for $T_{\text{eff}} \lesssim 42 \text{ kK}$ and lower g for $T_{\text{eff}} \gtrsim 42 \text{ kK}$. For $42 \gtrsim T_{\text{eff}}/\text{kK} \gtrsim 35$ ($\text{sdO9.5} \lesssim \text{Sp} \lesssim \text{sdB1}$), *salt_p00* gives g higher than *XTgrid* by ≈ 0.1 dex, but for $T_{\text{eff}}/\text{kK} \gtrsim 42$ ($\text{Sp} \lesssim \text{sdO9.5}$), systematic trends appear in the residual. For $T_{\text{eff}} \gtrsim 42 \text{ kK}$ ($\text{Sp} \lesssim \text{sdO9.5}$), *salt_p00* increasingly underestimates T_{eff} compared with *XTgrid*. The latter provides a roughly linear correlation between T_{eff} and Sp between sdO7 and sdB1 , although the gradient is markedly steeper than the equivalent relation reported by D13. The differences between results obtained from the two model

Table 4 – continued

Star	Class	σ	T_{eff} kK	$\log g$ cm s ⁻²	$\log y$	n_{He}	v_{rad} km s ⁻¹	v_{wid} km s ⁻¹	grid
PG 1220–056	sdO4VII:He39	0.021	† 59.04±0.14	6.04±4.46	0.51±0.07	0.76±0.04	–9	90	xt
PG 1230+067	sdON9.5VII:He39	0.011	43.33±0.07	6.20±0.04	1.01±0.09	0.91±0.02	–18	57	xt
EC 12349–2824	sdO8VII:He40	0.014	47.72±0.10	6.07±0.04	0.86±0.10	0.88±0.03	–9	72	xt
EC 12420–2732	sdOC4VII:He40	0.013	† 60.37±0.14	6.03±4.52	0.59±0.09	0.80±0.04	–28	110	xt
PG 1318+062	sdOC9VII:He39	0.023	46.76±0.10	5.97±0.04	1.17±0.18	0.94±0.03	20	66	xt
EC 13290–1933	sdOC9.5VII:He39	0.012	44.24±0.08	† 6.26±0.04	1.43±0.20	0.96±0.02	–26	72	xt
GLX J14258–0432	sdON7VI:He39 *	0.015	51.97±0.29	6.20±0.08	1.78±0.95	0.98±0.04	–137	! 12	xt
PG 1455–069	sdOC8.5VII:He40	0.033	48.30±0.19	† 6.36±0.04	0.91±0.11	0.89±0.03	18	83	xt
GLX J15235–1817	sdOC9VII:He39	0.016	44.80±0.10	6.01±0.04	1.19±0.16	0.94±0.02	18	68	xt
PG 1528+029	sdO8VII:He40	0.013	48.83±0.14	5.94±0.05	0.79±0.10	0.86±0.03	–48	78	xt
EC 15348–1652	sdO8VII:He39	0.015	48.97±0.19	6.06±0.05	0.58±0.07	0.79±0.03	28	76	xt
PG 1537–046	sdOC2VII:He40	0.015	† 61.27±0.16	5.51±0.05	0.39±0.06	0.71±0.04	–109	118	xt
PG 1625–034	sdO8VII:He39	0.043	45.38±0.10	† 6.30±0.04	0.33±0.04	0.68±0.03	–92	50	xt
GLX J16546+0318	sdOC3VII:He40	0.021	† 61.30±0.15	6.07±4.24	0.68±0.10	0.83±0.04	36	106	xt
GLX J17051–7156	sdOC6VII:He40	0.009	54.93±0.13	6.14±3.77	0.56±0.08	0.79±0.04	–48	97	xt
GLX J18325–4744	sdOC9VII:He38 *	0.010	44.67±0.11	5.97±0.04	1.48±0.29	0.97±0.02	–104	! 12	xt
GLX J18372–3125	sdOC8VII:He38 *	0.017	49.62±0.18	6.00±0.06	3.00±0.41	1.04±0.04	–37	! 12	xt
GLX J18387–5409	sdB0VII:He39	0.012	41.48±0.06	5.97±0.04	1.54±0.15	0.97±0.01	–9	78	xt
GLX J18459–4138	sdBN2V:He38	0.017	24.81±0.12	4.40±0.05	1.78±0.10	0.98±0.00	–69	98	p00
GLX J19059–4438	sdOC8.5VI:He39 *	0.013	47.43±0.11	5.95±0.05	1.43±0.36	0.96±0.03	–62	! 12	xt
GLX J19108–4417	sdBC0.2VI:He39	0.008	39.69±0.09	5.47±0.03	1.97±0.35	0.99±0.01	1	81	p00
GLX J19111–1406	sdOC6.5VII:He39 *	0.012	† 55.04±0.16	5.70±0.05	0.73±0.11	0.84±0.04	–240	! 12	xt
GLX J19150–4235	sdO8.5VII:He40	0.013	48.17±0.12	6.02±0.05	0.74±0.09	0.85±0.03	–15	71	xt
GLX J19333–2345	sdBC0.5VI:He38	0.016	39.60±0.10	5.93±0.03	1.87±0.23	0.99±0.01	84	86	p00
GLX J19376–4303	sdB2.5V:He21	0.013	26.21±0.12	4.76±0.04	–0.42±0.01	0.28±0.02	–50	89	p00
BPS 22896–0128	sdOC7VII:He39	0.018	51.29±0.13	5.83±0.05	0.58±0.07	0.79±0.04	–102	93	xt
EC 19529–4430	sdB3IV:He35	0.005	† 18.54±0.09	3.42±0.04	1.79±0.09	0.98±0.00	5	113	p00
GLX J20133–1201	sdOC2VII:He37	0.014	† 60.42±0.18	4.80±0.05	0.67±0.09	0.82±0.03	–70	135	xt
EC 20111–3724	sdO9VII:He33	0.010	43.08±0.09	5.87±0.04	–0.11±0.02	0.44±0.03	65	66	xt
EC 20111–6902	sdBC1.5VII:He38	0.019	34.10±0.11	5.68±0.04	1.99±0.22	0.99±0.01	–81	153	p00
GLX J20204–1901	sdBN0VI:He35	0.008	41.77±0.07	5.93±0.04	0.79±0.06	0.86±0.02	65	77	xt
EC 20184–3435	sdO9.5VI:He28	0.011	40.28±0.10	5.99±0.04	–0.20±0.02	0.39±0.02	–11	72	p00
EC 20187–4939	sdB0.2VII:He36	0.012	40.46±0.08	6.02±0.04	1.35±0.13	0.96±0.01	–69	94	p00
GLX J20251–0804	sdOC2VII:He39	0.014	† 59.92±0.17	4.97±0.05	0.39±0.05	0.71±0.04	64	118	xt
EC 20221–6249	sdOC9.5VII:He39	0.016	42.12±0.08	5.33±0.04	1.63±0.25	0.98±0.01	72	79	xt
EC 20236–5703	sdBC2.5IV:He35	0.011	26.38±0.13	4.14±0.05	1.72±0.10	0.98±0.00	–74	89	p00
BPS 22940–0009	sdBC1V:He38	0.010	34.65±0.11	4.89±0.04	1.78±0.15	0.98±0.01	28	93	p00
EC 20306–5127	sdOC6.5VII:He39	0.017	53.66±0.13	5.97±4.73	0.55±0.07	0.78±0.04	–17	81	xt
EC 20450–1501	sdOC8VII:He38	0.040	47.47±0.09	5.76±0.04	0.45±0.05	0.74±0.03	–100	13	xt
EC 20450–6947	sdO7VII:He40	0.009	51.24±0.19	6.06±0.08	0.61±0.08	0.80±0.03	69	76	xt
EC 20481–5518	sdO7.5VII:He39	0.011	51.96±0.19	6.15±0.22	1.01±0.17	0.91±0.03	–10	73	xt
LS IV–14 116	sdB1VII:He18	0.019	35.33±0.11	5.97±0.04	–0.77±0.01	0.15±0.02	–163	105	p00
Ton S 14	sdOC9VII:He40	0.022	46.59±0.10	6.02±0.04	1.02±0.13	0.91±0.03	–35	59	xt
EC 21077–4815	sdOC7.5VII:He39	0.025	47.77±0.10	6.12±0.04	0.64±0.07	0.81±0.03	41	55	xt
BPS 30319–0062	sdB0.5VII:He20	0.020	36.73±0.08	6.07±0.04	–0.74±0.01	0.15±0.02	–42	86	p00
EC 21125–7013	sdOC6.5VII:He40	0.019	54.11±0.13	6.16±3.10	0.69±0.09	0.83±0.04	–8	92	xt
EC 21306–4911	sdBC1VII:He40	0.019	36.91±0.09	5.96±0.04	1.84±0.17	0.99±0.01	29	105	p00
EC 21416–3645	sdO8.5VII:He34	0.019	51.17±0.21	6.10±0.07	1.00±0.16	0.91±0.03	43	130	xt
PHL 149	sdO7.5VII:He40	0.017	51.77±0.32	6.19±0.06	0.85±0.11	0.88±0.03	–5	69	xt
PHL 178	sdO7.5VII:He40	0.012	50.66±0.21	6.09±0.06	0.49±0.06	0.76±0.03	20	66	xt
PG 2158+082	sdO2VII:He40	0.012	† 63.42±0.15	6.19±1.70	0.42±0.07	0.72±0.04	–102	105	xt
BPS 22956–0090	sdO9VII:He40	0.012	45.70±0.10	6.10±0.04	0.89±0.09	0.89±0.02	–83	80	xt
BPS 22892–0051	sdOC7VII:He40	0.018	51.82±0.71	6.20±0.05	0.72±0.09	0.84±0.03	–100	56	xt
PB 7124	sdOC9VII:He40	0.021	47.81±0.10	6.01±0.04	0.91±0.11	0.89±0.03	–7	75	xt
BPS 22875–0002	sdOC9VII:He40	0.013	46.66±0.10	† 6.23±0.04	1.31±0.22	0.95±0.02	–47	63	xt
PG 2218+051	sdB0.5VII:He20	0.014	36.45±0.08	6.05±0.04	–0.88±0.01	0.12±0.02	14	94	p00
EC 22332–6837	sdO7.5VII:He37	0.030	47.27±0.11	6.15±0.04	0.08±0.03	0.54±0.03	–102	58	xt
BPS 22938–0044	sdOC7.5VII:He40	0.012	50.73±1.80	6.20±0.05	0.70±0.08	0.83±0.03	16	69	xt
EC 22536–5304	sdB0.2VII:He23	0.012	36.98±0.09	5.59±0.04	–0.26±0.02	0.36±0.02	21	97	p00
BPS 22938–0073	sdO7.5VII:He39	0.016	48.75±0.16	6.00±0.05	0.73±0.09	0.84±0.03	47	83	xt
PHL 540	sdO7.5VII:He40	0.013	49.85±0.17	5.99±0.06	0.69±0.09	0.83±0.03	1	72	xt
Ton S 103	sdBN0.2VII:He40	0.013	41.40±0.06	5.94±0.04	2.16±0.62	0.99±0.01	–55	83	xt
PB 5462	sdOC5VII:He40	0.045	† 61.40±0.17	5.48±0.05	0.43±0.07	0.73±0.04	–24	174	xt
HE 2347–4130	sdO8VII:He39	0.016	48.80±0.56	6.19±0.05	0.74±0.09	0.85±0.03	–8	83	xt

*: HRS spectrum, †: extrapolated

grids are shown in Fig. 6. These are indicative of the systematic errors introduced by assuming the overall metallicity and/or local thermodynamic equilibrium.

Experiments suggested that model grid spacings, metallicity and microturbulent velocity have a significant influence on the outcomes, but we conclude that the systematic errors introduced by the LTE assumption are unacceptable for $T_{\text{eff}} \geq 42$ kK. To avoid this critical boundary, we therefore use the nLTE zero metal grid (*XTgrid*) for $T_{\text{eff}} \geq 41$ kK. Below this value, metal-line blanketing and a model grid which extends to $\log g = 3$ are both required to obtain satisfactory fits, so the *salt_p00* grid is used for $T_{\text{eff}} < 41$ kK. Excluding outliers, there is a mean offset of $\approx 1.3 \pm 3.0 \text{ km s}^{-1}$ between radial velocities obtained using models from the two grids.

SFIT provides formal errors on the parameters governing the fit used based on a value of χ^2 which is not realistic because of the method used to increase the weight of specified spectral lines as described above. From the scatter of points in Fig. 6, we estimate measurement errors to be $\delta \log T_{\text{eff}} \approx \pm 0.012$, $\delta \log g \approx \pm 0.27$, $\delta \log y \approx \pm 0.29$, and $\delta v_{\text{rad}} \approx \pm 3.0 \text{ km s}^{-1}$. For convenience, the first three translate to fractional errors: $\delta T_{\text{eff}}/T_{\text{eff}} \approx \pm 0.028$, $\delta g/g \approx \pm 0.62$, and $\delta y/y \approx \pm 0.67$. These should be used in preference to the formal errors cited in Table 4.

A second approach to estimating the measurement errors was to use the best-fit models obtained with the *salt_p00* grid as an independent low-noise sample with otherwise similar spectral properties to the observed sample. This sample was processed with the *XTgrid* models in exactly the same way as before, except that no velocity correction was necessary. Then the differences between the parameters obtained from the observed sample and the theoretical sample were formed, giving the following mean differences and standard deviations: $\langle \Delta \log T_{\text{eff}} \rangle = 0.000 \pm 0.017$, $\langle \Delta \log g \rangle = 0.253 \pm 0.203$, and $\langle \Delta \log y \rangle = -0.112 \pm 0.262$. Restricting the test sample to $T_{\text{eff}} > 42$ kK, these numbers change to $\langle \Delta \log T_{\text{eff}} \rangle = -0.005 \pm 0.015$, $\langle \Delta \log g \rangle = 0.236 \pm 0.201$, and $\langle \Delta \log y \rangle = -0.069 \pm 0.174$. Again, these translate to mean fractional errors $\delta T_{\text{eff}}/T_{\text{eff}} \approx \pm 0.039$, $\delta g/g \approx \pm 0.46$, and $\delta y/y \approx \pm 0.40$.

Solutions obtained with both grids show a correlation between the upper limit of $\log y$ and T_{eff} for $T_{\text{eff}} \gtrsim 40$ kK (Fig. 7). As T_{eff} increases and the number of neutral hydrogen atoms becomes critically small, RSS spectra containing helium become increasingly degenerate in y at high T_{eff} . The situation ameliorates at high resolution when the displacement between Balmer and ionized helium lines allows the former to be resolved.

Representative spectra and best-fit solutions are illustrated in Fig. 8. Equivalent plots for the entire sample of Table 3 are provided in Figs. E.1–E.7 of the Supplementary material.

4.4 Previous results

Spectroscopic measurements of one or more of T_{eff} , $\log g$, $\log y$ have been published for some 30 members of the overall sample (Table 5). Fig. 9 compares those data with values in Table 4. More than two thirds of the differences are within either the errors of the original observations or of the new measurements. Of the remainder: PB 5462 (Hügelmeier et al. 2006) lies outside the current model grid, Ton S 144 and Ton S,103 were measured using a restricted grid of nLTE models (Hunger et al. 1981), the weakness of He II 4686 in GLX J18459–4138 was overlooked by Németh et al. (2012) (cf. Jeffery 2017), the hydrogen abundances measured from high-resolution spectra of LSS 1274 and UVO 0904–02 by Schindewolf et al. (2018b) are to be preferred, the published helium abundance of EC 05593–5901 was 1.5 dex above the bound-

Table 5. Published atmospheric parameters for SALT sample members. Errors $< \pm 0.1$ have been rounded up.

Star	T_{eff} kK	$\log g$ cm s ⁻²	$\log y$	Reference
Ton S 144	38.0±3.5	4.5±0.4	0.4±0.2	Hunger et al. (1981)
— " —	41.7±1.1	5.7±0.1	2.1±0.1	Ströer et al. (2007)
BPS 22946–0005	20.0±3.0	2.7±0.3	-1.1±0.1	Kendall et al. (1997)
SB 705	45.1±8.1	5.6±0.6	1.0±0.4	Németh et al. (2012)
— " —	44.7±3.5	5.8±0.4	0.0±0.1	Hunger et al. (1981)
LB 3229	40.0±0.5	5.2±0.2	1.9±0.8	Naslim et al. (2010)
Feige 19	40.0±2.5	5.0±0.3	1.0±1.5	Dreizler et al. (1990)
— " —	45.0±2.5	6.0±0.3	0.3±0.4	Thejll et al. (1994)
PG 0240+046	37.0±2.5	5.3±0.3	0.1±0.3	Thejll et al. (1994)
— " —	34.0±0.2	5.4±0.1	0.2±0.1	Ahmad & Jeffery (2003)
EC 03505–6929	42.6±0.2	6.2±0.1	0.2±0.1	Moni Bidin et al. (2017)
HE 0414–5429	50.6±0.7	6.5±0.1	0.3±0.3	Moni Bidin et al. (2017)
GLX J04205+0120	45.0±0.8	5.7±0.2	> 1.2	Vennes et al. (2011)
— " —	46.1±0.9	6.0±0.2	1.0±0.2	Németh et al. (2012)
EC 04271–2909	53.0	—	—	Drilling & Beers (1995)
EC 05593–5901	42.2±0.3	5.6±0.2	0.6±0.2	Moni Bidin et al. (2017)
GLX J07581–0432	41.4±0.5	5.9±0.3	0.5±0.5	Németh et al. (2012)
PG 0902+057	43.0±2.5	6.0±0.3	1.5±0.4	Thejll et al. (1994)
UVO 0904–02	47.0±0.5	5.7±0.1	2.0±0.3	Schindewolf et al. (2018a)
LSS 1274	44.3±0.4	5.5±0.1	2.2±0.3	Schindewolf et al. (2018a)
PG 0958–119	44.2±0.5	5.4±0.1	1.2±0.4	Hirsch & Heber (2009)
PG 1127+019	43.7±0.7	5.9±0.2	1.9±1.2	Luo et al. (2016)
PG 1230+067	43.0±2.5	5.5±0.3	1.2±1.5	Thejll et al. (1994)
PG 1318+062	44.6±1.0	5.8±0.2	1.1±0.8	Luo et al. (2016)
GLX J18459–4138	35.9±4.8	5.2±0.3	2.1±1.1	Németh et al. (2012)
— " —	26.2±0.8	4.2±0.1	2.0±0.4	Jeffery (2017)
GLX J19111–1406	56.0±4.5	5.7±0.7	0.3±0.9	Németh et al. (2012)
BPS 22940–0009	33.7±0.8	4.7±0.2	2.2±0.1	Naslim et al. (2010)
LS IV–14 116	34.0±0.5	5.6±0.1	-0.7±0.1	Naslim et al. (2011)
— " —	35.0±0.3	5.9±0.1	-0.6±0.1	Green et al. (2011)
— " —	35.2±0.1	5.9±0.1	-0.6±0.1	Randall et al. (2015)
— " —	35.5±1.0	5.9±0.9	-0.6±0.1	Dorsch et al. (2020)
PG 2158+082	75.1±7.6	6.0±0.2	0.2±1.1	Németh et al. (2012)
BPS 22892–0051	45.7	—	—	Beers et al. (1992)
BPS 22875–0002	56.2	—	—	Beers et al. (1992)
PG 2218+051	36.5±1.0	6.2±0.2	-0.8±0.1	Saffer et al. (1994)
— " —	36.0±0.7	5.9±0.1	-0.7±0.1	Luo et al. (2016)
EC 22536–5304	36.9±0.1	6.1±0.1	-0.5±0.1	Jeffery & Miszalski (2019)
Ton S 103	39.8±3.5	6.5±0.4	2±1	Hunger et al. (1981)
PB 5462	47.5	8.2	—	Kepler et al. (2015)
— " —	60.0±0.9	6.4±0.1	—	Hügelmeier et al. (2006)
HE 2347–4130	44.9±1.2	5.8±1.5	1.4±0.4	Ströer et al. (2007)

ary of the model grid used by Moni Bidin et al. (2017), and the spectrum of PG 0240+046 used by Ahmad & Jeffery (2003) was limited to H γ , He I 4388 and 4471.

5 HIGHLIGHTS

The primary objective of this part of the survey was to identify stars of particular interest for further investigation. For us this means:

- stars at late spectral types (sdO9–sdB3) (or low T_{eff} and g) which might indicate links to other classes of helium-rich stars,
- stars with intermediate helium classes (He10–He35) (or helium - to - hydrogen ratios) which might include heavy-metal stars and confronts the question of why hot subdwarfs are predominantly extremely helium-poor or helium-rich,
- stars with anomalous radial or rotational velocities which might indicate subdwarfs in close binary systems or otherwise high-velocity stars.

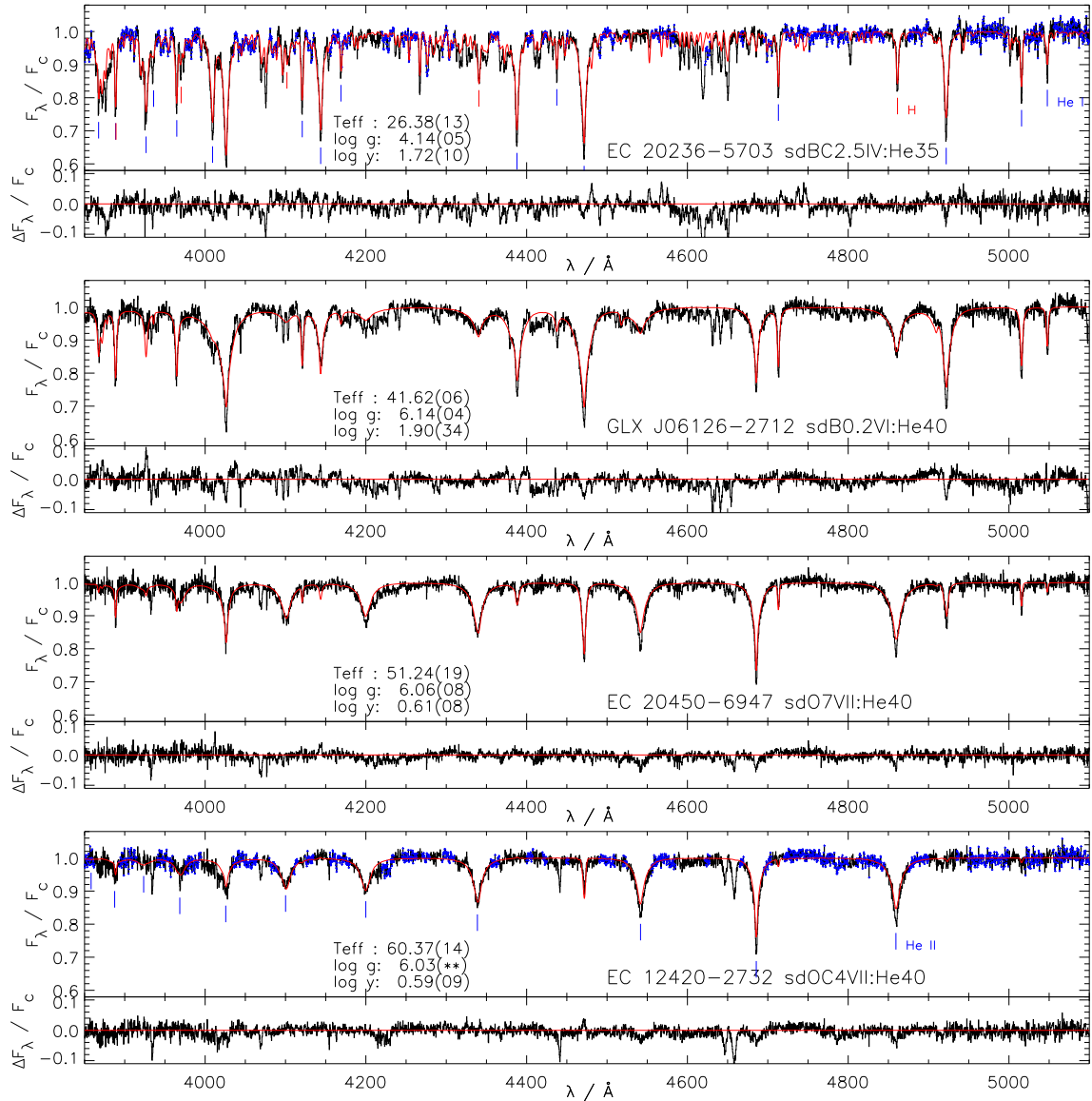


Figure 8. RSS spectra and best fit solutions for a selection of representative stars. Each panel shows the merged spectrum (black histogram) and the best-fit solution (red polyline). The residual (observed – calculated) is plotted beneath. Each star’s identifier, assigned spectral type and physical parameters (T_{eff} /kK, $\log g/\text{cm s}^{-2}$, and $\log y$) are indicated, with formal errors in the last 2 digits in parentheses. Positions of hydrogen Balmer lines (red) and neutral helium lines (blue) are identified for EC 20236-5703. Ionized helium lines are identified for EC 1240-2732. ‘Continuum’ regions used to rectify all observed spectra are identified by blue crosses for the latter two stars. Equivalent plots for the entire sample of Table 3 are provided in the supplementary material.

The stars have been gathered into subgroups described in the following subsections. Within each group, stars are introduced by name, spectral class and model-dependent parameters as in Table 4. The last are expressed as (T_{eff} /kK, $\log g/\text{cm s}^{-2}$, $\log y$). Groups and individual stars are identified in Fig. 10.

5.1 Sp = sdB1 – sdB3, LC \leq V, He > 20

The first group includes stars which are classified sdB1 or later and have luminosity class V or less. These are indicated by filled red squares in Fig. 10. As such, they are not true subdwarfs since their surface gravity is similar to or lower than that of the main-sequence. Some or all might be shown to be subluminous on account of their mass and luminosity.

GLX J18459–4138 (sdB2V:He38) (24.8, 4.4, 1.8) was identified as being similar to the pulsating helium star V652 Her. The survey parameters are consistent with those given by Jeffery (2017). It is the only nitrogen-rich member of this group.

GLX J19376–4303 (sdB2.5V:He21) (26.2, 4.8, –0.4) appears similar to GLX J18459–4138 but has stronger Balmer lines, indicating hydrogen and helium abundances of 63% and 27% respectively (Jeffery et al. 2017a).

EC 19529–4430 (sdB3IV:He35) (18.5, 3.4, 1.8) shows no ionized helium lines (including HeII 4686Å) and Balmer lines much weaker than the neutral helium lines. A defining feature is the weakness of all metal lines (cf. HD144941: Harrison & Jeffery 1997) and the narrow wings of the H and HeI lines.

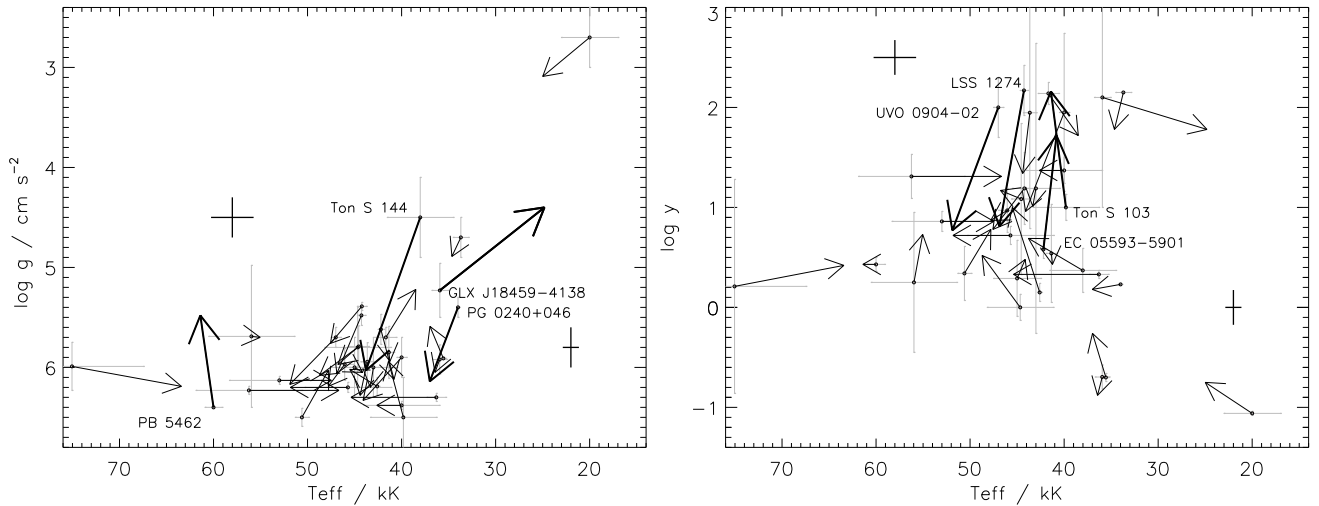


Figure 9. As Fig. 7, showing previous results for SALT sample members (grey error bars) linked to the current result (Table 4) by an arrow. The largest differences are indicated by thicker lines and labelled (i.e. for $\delta \log T_{\text{eff}} > 0.1$, $\delta \log g > 0.6$, or $\delta \log y > 1.0$). The mean SALT error bars are shown as in Fig. 7. Data values and sources for the previous results are given in the Supplementary Material (Appendix F). Where g or y were not given in the earlier study, we have substituted values from Table 4.

EC 20236–5703 (sdBC2.5IV:He35) (26.4, 4.1, 1.7) has similar properties to EC 19529-4430, but with slightly narrower He I lines and a carbon rich metal-lined spectrum. It is likely to have similarities to the carbon-rich pulsating helium star BX Cir (Woolf & Jeffery 2000).

BPS 22940–0009 (sdBC1V:He38) (34.7, 4.9, 1.8) makes the fifth and hottest member of this group, all of which could be called extreme helium stars. Its closest well-studied counterparts are the hot extreme helium star LS IV+6² (Jeffery 1998), and PG 1415+492 (sdBC1VI:He39 Ahmad & Jeffery 2003) and PG 0135+243 (Moehler et al. 1990b). A high-resolution spectral analysis was carried out by Naslim et al. (2010) who showed it to be the lowest gravity member of their sample of helium-rich subdwarfs. Our coarse analysis is in general agreement.

BPS 22946–0005 (sdB2.5II:He24) (25.0, 3.1, –0.8) has He < 30 but otherwise fits this group. It is a post-AGB star analyzed by Kendall et al. (1997). It was mistakenly included in our sample but provides a useful control. In comparison with Kendall et al., our temperature is high and our gravity low, but still consistent with a post-AGB star.

5.2 $Sp = \text{sdO9.5} - \text{sdB1}$, $LC \approx \text{V} - \text{VI}$, $He > 30$

If signal-to-noise ratios were higher, and luminosity classification was a more precise science, this section would isolate other sample members with $LC \leq \text{VI}$, and hence identify the remaining high luminosity stars. Given the large errors associated with assigning luminosity class, $\log g \leq 5.7$ has been used as a proxy.

GLX J19108-4417 (sdBC0.2VI:He39) (39.7, 5.5, 2.0) is just slightly hotter and less luminous than BPS 22940–0009 (see above). Whilst it also resembles the extreme helium dwarf LS IV+6² (Jeffery 1998), it has a higher hydrogen abundance (Beliere 2018). Again, connections with PG 1415+492 (Ahmad & Jeffery 2003) and PG 0135+243 (Moehler et al. 1990b) should also be explored.

Other stars in this group include: EC 20111–6902 (sdBC1.5VII:He38 — 34.1, 5.7, 2.0), Ton S 148 (sdBC0.2VI:He37 — 38.5, 5.2, 1.7), GLX J08454–1214 (sdOC9.5VI:He39 — 43.4, 5.2, 1.5), and EC 20221-6249 (sdOC9.5VII:He39 — 42.1, 5.3, 1.6). They are indicated by green diamonds in Fig. 10 and all await detailed analysis from high-resolution spectroscopy. These stars will be crucial in establishing any link between the low-luminosity helium stars identified in § 5.1 and helium-rich subdwarfs stars on the helium-main-sequence, such as the post-double white dwarf merger connection proposed by Zhang & Jeffery (2012).

5.3 $Sp = \text{sdB0} - \text{sdB1}$, $He < 25$

As a primary indicator, helium class is a useful proxy for surface helium abundance, but is increasingly imperfect at spectral types earlier than sdO8 (Fig. 4). There are 14 stars in the sample with $\text{sdO8} \leq Sp \leq \text{sdB1}$ and $He < 35$. These are often referred to as intermediate helium-rich subdwarfs. Spectral characteristics vary enormously across the group, which covers transitions from helium to hydrogen dominated and He I to He II dominated spectra. Identifying smaller subgroups is useful.

The most distinctive and most hydrogen-rich group covers a narrow spectral range $\text{sdB0} \leq Sp \leq \text{sdB1}$, $He < 25$ and includes the heavy-metal subdwarfs. These are indicated by large filled blue circles in Fig. 10.

LS IV–14 116 (sdB1VII:He18) (35.3, 6.0, –0.8) is a well-studied pulsating intermediate helium subdwarf with a remarkable surface chemistry (Ahmad & Jeffery 2005; Naslim et al. 2011). It was included in the RSS sample as a control. The survey parameters are consistent with other recent measurements (Randall et al. 2015; Dorsch et al. 2020).

EC 22536–5304 (sdB0.2VII:He23) (37.0, 5.6, –0.3) was identified from the 4495Å line of triply-ionized lead in the HRS spectrum, and confirmed by the detection of both Pbrv 4495 and 4049Å in the RSS

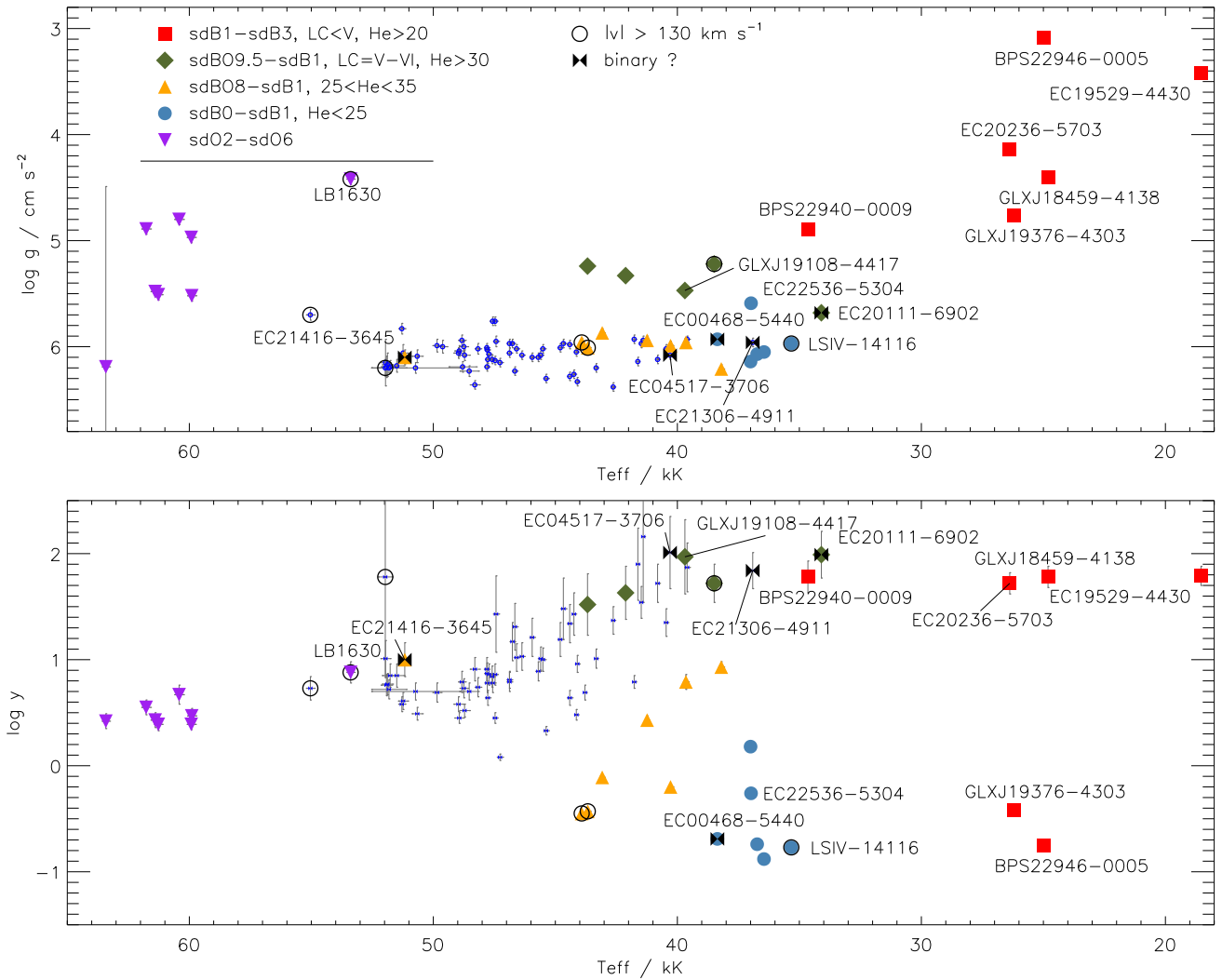


Figure 10. As Fig. 7 extended to identify subgroups and individual stars discussed in § 5. The groups identified in the key and by different colours and symbols correspond to §§ 5.1 – 5.7. The small blue circles refer to the remaining stars (cf. § 5.8).

spectrum. It is the most lead-rich heavy-metal subdwarf so far, with a lead abundance 4.5 dex above solar (Jeffery & Miszalski 2019).

Four additional stars have similar spectral type: EC 00468–5440 (sdBC0VII:He25 — 38.4, 5.9, –0.7), PG 2218+051 (sdB0.5VII:He20 — 36.5, 6.1, –0.9), BPS 30319–0062 (sdB0.5VII:He20 — 36.7, 6.1, –0.7), and PG 0240+046 (sdBC0.5VII:He25 — 37.0, 6.1, 0.2). Their spectra are illustrated in Fig. 11. For the known examples of this group, in which radiative levitation is regarded as the crucial driver of exotic chemistry, the sharp heavy-metal absorption lines are distinctive in high-resolution spectra because of their very low rotation velocity. The lines are much harder to recognise at the resolution of classification spectra. Coarse analyses have been carried out previously for PG 2218+051 (Saffer et al. 1994; Luo et al. 2016) and PG 0240+046 (Aznar Cuadrado & Jeffery 2001; Ahmad & Jeffery 2003), with similar results to those presented here. Whilst all six stars show a clear signature from C III 4647,4650 Å, it is only strong enough in two cases, PG 0240+046 and EC 00468–5440, to trigger a carbon-rich ‘C’ classification. The four heavy-metal candidates should be investigated at higher resolution and signal-to-noise for

evidence of lead or zirconium absorption lines, and to determine whether the carbon abundance is correlated with hydrogen-to-helium ratio.

5.4 Sp = sdO8 – sdB1, 25 < He < 35

Of the remaining intermediate helium stars, EC 04013–4017 (sdBC1VII:He32 — 38.2, 6.2, 0.9) is the coolest and could arguably have been included amongst the group in § 5.2 since the helium class and log y appear contradictory.

Six stars in the sample have similar spectra with some spread in H/He and He I/II ratios: Ton S 148 (sdBC0.2VI:He32 — 38.5, 5.2, 1.7), LB 3289 (sdBN0.2VII:He29 — 39.7, 6.0, 0.8), GLX J07581–0432 (sdO9.5VII:He33 — 41.2, 5.9, 0.4), EC 20184–3435 (sdO9.5VI:He28 — 40.3, 6.0–0.2), EC 20111–3724 (sdO9VII:He33 — 43.1, 5.9, –0.1), Ton S 415 (sdO8VII:He30 — 43.9, 6.0, –0.5), and EC 05242–2900 (sdO8VII:He28 — 43.7, 6.0, –0.4). These represent quintessentially typical intermediate helium-rich stars, concerning which little is known. They are indicated by yellow upward triangles in Fig. 10.

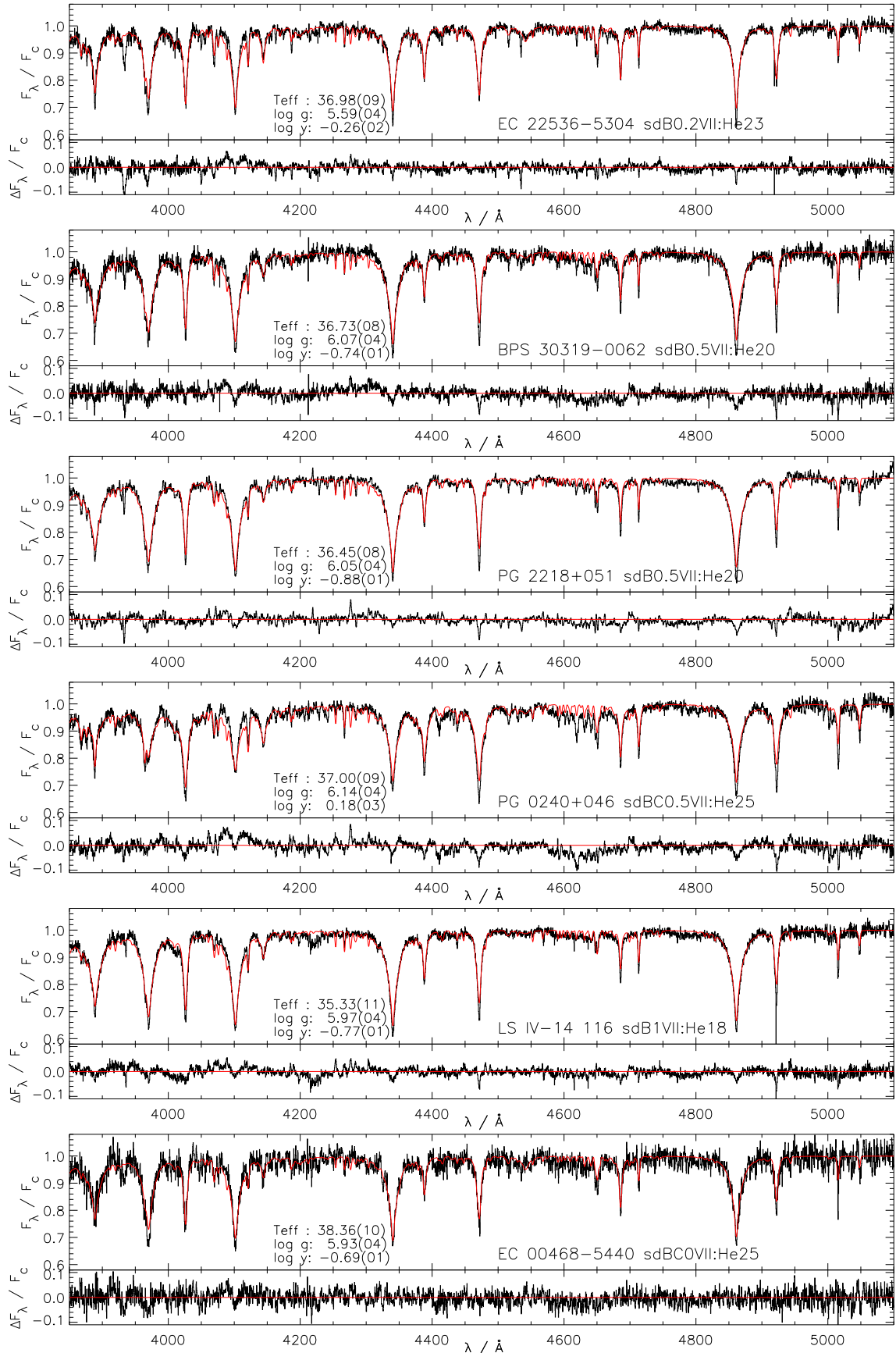


Figure 11. As Fig. 8 for intermediate helium subdwarfs. LSIV-14°116 and EC22536-5304 are known heavy-metal subdwarfs (Naslim et al. 2010; Jeffery & Miszalski 2019); PG 0240+046, PG 2218+051, BPS 30319-0062, or EC 00468-5440 have similar T_{eff} , g and y , but no heavy-metal detections yet.

For GLX J07581-0432, [Németh et al. \(2012\)](#) give $T_{\text{eff}}, \log g, \log y \approx 41.4, 5.9, 0.07$ in good agreement with our analysis. Other stars in this group include BPS 22956-0094 ([Naslim et al. 2010](#)) and possibly HS 1000+471 (sdBC0.2VII:He28) and Ton 107 (sdBC0.5VII:He28) ([Ahmad & Jeffery 2003](#)).

EC 21416-3645 (sdO8.5VII:He34) (51.2, 6.1, 1.0) stands out. Most of the principal H and He lines are weaker than in the stars described above. The spectrum is unique in our sample, showing strong broad features at calcium H and K. In hot stars, these normally correspond to either He or He II 3968Å (or both), and He I 3935Å, and are rarely seen at similar strength. The DSS2 image is elliptical, whilst the 2MASS image is circular and offset 2.7'' to the west. It appears that the hot subdwarf spectrum is contaminated by that of a faint red star, Gaia DR2 6586406672826522112 ($\langle g \rangle = 15.6, b_p - r_p = 0.85$). Having twice the parallax of EC 21416-3645, the two stars are unlikely to be associated. The two stars would be unresolved under normal SALT seeing conditions. The cool star may also account for apparent noise in the combined spectrum.

5.5 High radial velocity

As a consequence of the optical layout and from undocumented experience, we do not have full confidence in the SALT/RSS radial velocities and so the precision of v_{rad} in Table 4 may be worse than the statistical errors suggest. However, as a counter argument, LS IV -14 116 has a well-established radial velocity of $-149 \pm 2 \text{ km s}^{-1}$ ([Randall et al. 2015](#)). Table 4 gives $-163 \pm 1 \text{ km s}^{-1}$. Table 4 is therefore useful for identifying high velocity stars and/or close binaries. As an arbitrary example, other stars in the sample with $|v_{\text{rad}}| > 130 \text{ km s}^{-1}$ include GLX J19111-1406, GLX J14258-0432, EC 05242-2900, Ton S 148, LB 1630, and Ton S 415. They are indicated by black circles surrounding the spectral group symbol in Fig. 10. It will be interesting to investigate the space motions of these stars.

5.6 Broad lines: $v_{\text{wid}} > 150 \text{ km s}^{-1}$

The mean line width for RSS spectra in Table 4 is $\langle v_{\text{wid}} \rangle = 85 \pm 21 \text{ km s}^{-1}$. Excluding very hot stars $T_{\text{eff}} \geq 50 \text{ kK}$, where hydrogen-helium blends cannot be resolved, $\langle v_{\text{wid}} \rangle = 80 \pm 16$. Stars with $v_{\text{wid}} \geq \langle v_{\text{wid}} \rangle + 2\sigma$ are of interest, since these indicate either a higher than average rotation velocity, a variable velocity spectrum used to construct the mean, or a spectrum originating in two or more similar stars with different velocities. Examples are indicated by black bowties superimposed on the spectral group symbol in Fig. 10. Table 4 shows four stars with $v_{\text{wid}} > 112 \text{ km s}^{-1}$ and $T_{\text{eff}} < 50 \text{ kK}$.

EC 20111-6902 (sdBC1.5VII:He38) (34.1, 5.7, 2.0). The SFIT solution to the hydrogen-deficient spectrum of EC 20111-6902 ($T_{\text{eff}} = 34 \text{ kK}$) shows a well-above average value for the line width ($v_{\text{wid}} = 153 \text{ km s}^{-1}$). Using *XTgrid* yielded $v_{\text{wid}} = 204 \text{ km s}^{-1}$ and so the high value is not a consequence of using LTE rather than non-LTE models. The spectrum is well-exposed ($S/N \approx 52$), being the sum of observations made on 4 separate nights. The individual observations show a spread in radial velocity of 40 km s^{-1} from cross-correlation with a model template and of 53 km s^{-1} from shifts in the C II 4267 Å absorption line. Co-adding these spectra without correction will contribute substantially to the high value of v_{wid} . The cause of the variation requires further investigation. The spectrum bears a strong similarity to that of the double helium subdwarf

binary PG 1544+488 (sdBC1VII:He39p: D13) (Fig. 12). The latter has a 12 h orbital period with velocity semi-amplitudes of 87 and 95 km s^{-1} for each of the components, respectively ([Ahmad et al. 2004](#); [Şener & Jeffery 2014](#)). It is proposed that EC 20111-6902 is very likely a spectroscopic binary containing at least one, if not two, helium-rich subdwarfs, and for which the velocity semi-amplitude is at least 50 km s^{-1} .

EC 04517-3706 (sdB0.5VI:He40) (40.3, 6.1, 2.0) has $v_{\text{wid}} = 118 \text{ km s}^{-1}$ on the 2σ boundary. It is warmer and less carbon-rich than EC 20111-6902 (Fig. 12).

EC 21306-4911 (sdBC1VII:He40) (36.9, 6.0, 1.8) has a spectrum and parameters similar to EC 20111-6902 (Fig. 12). Both have strong carbon lines. $v_{\text{wid}} = 105 \text{ km s}^{-1}$ is high but lies within 2σ of the mean. While only a single RSS observation contributes to the spectrum, the S/N ratio is the same as that of the combined spectrum of EC 20111-6902. Variable radial velocity is not a contributing factor, but the presence of two similar spectra with different velocities, as in PG 1544+488, cannot be ruled out. Additional time-resolved high-resolution measurements are essential for all of these potential binary-star candidates.

EC 00468-5440 (sdBC0VII:He25) (38.4, 5.9, -0.7) has $v_{\text{wid}} = 117 \text{ km s}^{-1}$ but a spectrum similar to the otherwise sharp-lined intermediate helium-rich subdwarfs (see § 5.3). A higher S/N spectrum is required.

5.7 $Sp \lesssim \text{sdO6}$

Thirteen stars have spectral types earlier than sdO6, including GLX J17051-7156 (sdOC6VII:He40 — 54.9, 6.1, 0.6), PB 5462 (sdOC5VII:He40 — 61.4, 5.5, 0.4), LB 1630 (sdOC5VI:He38 — 53.4, 4.4, 0.9), EC 12420-2732 (sdOC4VII:He40 — 60.4, 6.0, 0.6), PG 1220-056 (sdO4VII:He39 — 59.0, 6.0, 0.5), GLX J16546+0318 (sdOC3VII:He40 — 61.3, 6.1, 0.7), EC 10475-2703 (sdOC3VI:He39 — 59.9, 5.5, 0.5), GLX J07158-5407 (sdO3VII:He40 — 61.0, 6.0, 0.3), PG 1537-046 (sdOC2VII:He40 — 61.3, 5.5, 0.4), GLX J20251-0804 (sdOC2VII:He39 — 59.9, 5.0, 0.4), GLX J20133-1201 (sdOC2VII:He37 — 60.4, 4.8, 0.7), EC 11236-1945 (sdO2VII:He40 — 61.8, 4.9, 0.6), and PG 2158+082 (sdO2VII:He40 — 63.4, 6.2, 0.4). These correspond to subdwarfs with $T_{\text{eff}} \geq 50 \text{ kK}$ and stretch both the boundaries and the physics of the model atmosphere grids. They are indicated by purple downward triangles in Fig. 10.

The majority have strong carbon lines, including emission around 4650 Å . As discussed already, the absence of neutral hydrogen at these temperatures makes it difficult to measure the hydrogen abundance at the resolution of the RSS spectra.

LB 1630 (sdOC5VI:He38) (53.4, 4.4, 0.9) has markedly narrower He II lines than the remainder of this group, hence its lower luminosity class and, indeed, surface gravity. It is possibly similar to the helium-rich subdwarfs LSE 153, 259 and 263 ([Husfeld et al. 1989](#)) or BD+37 442 and BD+37 1977 ([Jeffery & Hamann 2010](#)) and hence the descendant of a helium-shell-burning giant rather than a helium-core-burning subdwarf. Detailed fine analysis of this and the higher-gravity subdwarfs in this group would address important questions about their origin and fate.

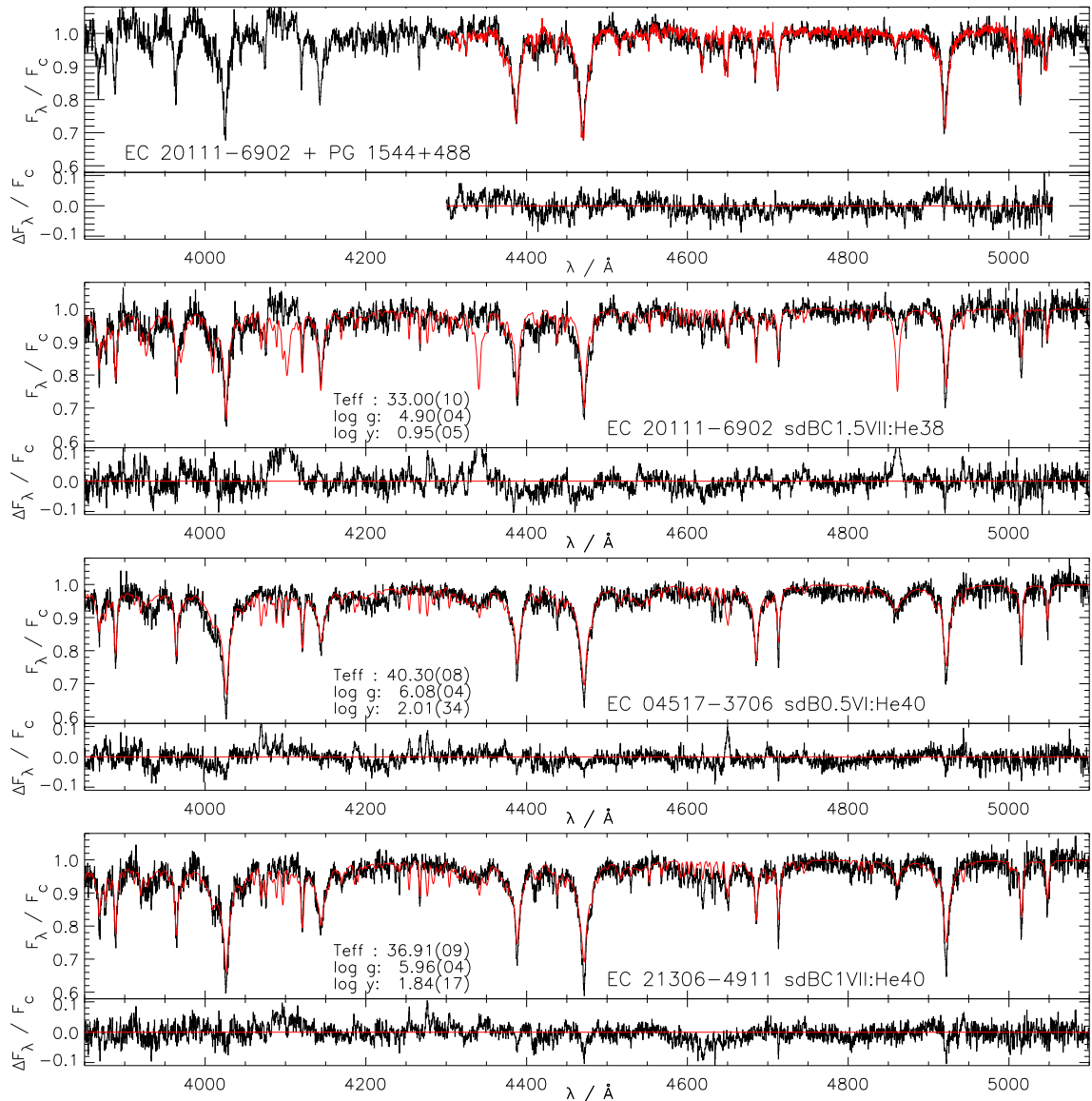


Figure 12. Stars with spectra similar to the double helium-rich subdwarf PG 1544+488. Top: Comparison of the SALT/RSS spectrum of EC 20111–6902 (black) with a William Herschel Telescope spectrum (r746709) of the double helium white dwarf PG 1544+488 (red) (Sener & Jeffery 2014, Table 3). The latter has been shifted in radial velocity to match. The residual (EC 20111 – PG 1544) is shown beneath at the same scale. Bottom three panels: As Fig. 8 for EC 20111–6902, EC 04571–3706 and EC 21306–4911.

5.8 $Sp = sdO6.5 - sdB0.5, He \gtrsim 35$

The remaining members of the sample comprise what are most commonly understood to be ‘He-sdO’ stars. These are indicated by small blue circles in Fig. 10. They all have low hydrogen abundance and a (rms) dispersion in surface gravity which is less than the estimated measurement error ($\langle \log g \rangle = 6.05 \pm 0.19$), although several of the solutions lie uncomfortably close to the *XTgrid* boundary. Nearly half (35) have a carbon-rich ‘C’ classification and 4 have a nitrogen-rich ‘N’ classification. 52 are concentrated in spectral types sdO7 to sdO9.

Detailed inspection of the spectra of these stars will surely yield additional surprises. Since these stars are likely to have surfaces which provide a chemical record of previous evolution, further analysis to obtain precise hydrogen, carbon and nitrogen abundances, as well as data for other species, will be invaluable (cf. Zhang & Jeffery 2012).

6 CONCLUSION

The current survey aims to characterize the properties of a substantial fraction of helium-rich subdwarfs in the southern hemisphere, to establish the existence and sizes of subgroups within that sample, and to provide evidence with which to explore connections between these subgroups and other classes of evolved star. This paper has presented and validated the methods used to observe, classify and measure atmospheric parameters from intermediate dispersion ($R \approx 3600$) spectroscopy obtained primarily with the Robert Stobie spectrograph of the Southern African Large Telescope. It has presented spectral classifications on the MK-like Drilling system (D13) and atmospheric parameters T_{eff} , $\log g$, $\log y$ based on non-LTE zero-metallicity ($T_{\text{eff}} > 41$ kK) or LTE line-blanketed ($T_{\text{eff}} < 41$ kK) model atmospheres. Although the majority of the sample, especially for spectral types earlier than sdO8, are classified as being extremely helium rich on the basis of line depth ratios, the helium to hydrogen

ratio y is not well constrained by model atmospheres for $T_{\text{eff}} > 40$ kK at the classification resolution. There are two reasons: one is that it is increasingly difficult to resolve hydrogen from the dominant He II lines as T_{eff} increases and the other is that, as the hydrogen abundance $n_{\text{H}} \rightarrow 0$, the error in the denominator ($y = n_{\text{He}}/n_{\text{H}}$) dominates.

It is clear that the generic term ‘helium-rich subdwarfs’ as applied to low-resolution classification surveys includes stars with a wide range of properties. The majority (74/106) occupy a tight volume in parameter space with $41 \lesssim T_{\text{eff}}/\text{kK} \lesssim 52$, $5.9 \lesssim \log g/\text{cm s}^{-2} \lesssim 6.4$, and $\log y > 0.5$. Of the remainder distinct groups include: very hot stars with spectral types sdO6 or earlier (13), cool low-gravity ($\log g < 5$) extremely helium-rich stars (5), and stars with intermediate helium abundances and spectral types sdO8 – sdB1 (14), of which up to 6 may have surfaces heavily enriched in s-process elements.

Several remarkable individual stars have been identified. A few have been reported previously, e.g. GLX J18459–4138, EC 22536–5305 (Jeffery et al. 2017b; Jeffery & Miszalski 2019). At least one star (EC 20111–6902) is a radial-velocity variable and bears a strong resemblance to the double helium subdwarf PG 1544+488. Other binaries are likely to lie undetected within the sample. One star (EC 19529–4430) at the extreme cool end of the sample is remarkable for the absence or weakness of its metal lines. LB 1630 appears to be a high luminosity extreme helium subdwarf.

Immediate future work will include completion of the low-resolution survey with SALT/RSS and its extension to high-resolution for all sufficiently bright sample members. The sample must also be reviewed for radial-velocity variables, and followed up for positive detections. Classification and parameterisation should be carried out for the remainder of the sample on completion of the observations, and should include stars observed with other telescopes so as to establish a complete magnitude limited sample.

Methods used for atmospheric analyses must be extended to include line-blanketed nLTE models of appropriate composition wherever practically possible, though appropriate LTE models will continue to be useful for low temperature stars $T_{\text{eff}} > 30$ kK. Robust techniques that deliver reliable, self-consistent and precise fundamental quantities and abundances for large numbers of helium-rich subdwarfs are urgently required.

With the imminent improvement of Gaia parallaxes and proper motions to $< 0.001''$, spectroscopy should be supplemented with total-flux methods to establish precise angular diameters which will yield useful radii, luminosities and galactic orbits.

Spectroscopic masses derived therefrom together with abundances for carbon, nitrogen and other species, will provide illuminating tests for evolution models that otherwise pass the tests of radius, luminosity and galactic location.

ACKNOWLEDGMENTS

The Armagh Observatory and Planetarium is funded by direct grant from the Northern Ireland Dept for Communities. That funding has enabled the Armagh Observatory and Planetarium to participate in the Southern African Large Telescope (SALT) through member of the United Kingdom SALT consortium (UKSC). All of the observations reported in this paper were obtained with SALT following generous awards of telescope time from the UKSC and South African SALT Time Allocation Committees under programmes 2016-1-SCI-045, 2016-2-SCI-008, 2017-1-SCI-004, 2017-2-SCI-007, 2018-1-SCI-038, 2018-2-SCI-033, and 2019-1-MLT-003. The authors acknowledge invaluable assistance from current and former SALT staff, particularly Christian Hettlage and Steve Crawford. The model

atmospheres were computed on a machine purchased under grant ST/M000834/1 from the UK Science and Technology Facilities Council. This research has made use of the SIMBAD database, operated at CDS, Strasbourg, France

DATA AVAILABILITY

The raw and pipeline reduced SALT observations are available from the SALT Data Archive (<https://ssda.sao.ac.za>). The model atmospheres and spectra computed for this project are available on the Armagh Observatory and Planetarium web server (<https://armagh.space/~SJeffery/Data/>).

SUPPLEMENTARY MATERIAL

The supplementary material contains five appendices as follows.

A: provides dates on which SALT obtained data with either RSS or HRS for each star classified in Table 2 (i.e. Table 1 in full).

B: compares automatic classifications obtained by applying the algorithms described in § 3.1 with the manual classifications given by D13. The observational data are the same for both sets of classifications.

C: compares theoretical spectra selected from the grids described in § 4.1.

D: compares effective temperature, surface gravity and helium-to-hydrogen ratio (T_{eff} , $\log g$, $\log y$) as determined in § 4 with the corresponding spectral type, luminosity and helium classes as determined in § 3.

E. shows the complete ensemble of reduced survey spectra, best-fit models and residuals.

REFERENCES

- Adelman-McCarthy J. K., Agüeros M. A., Allam S. S., et al. 2006, *ApJS*, **162**, 38
- Ahmad A., Jeffery C. S., 2003, *A&A*, **402**, 335
- Ahmad A., Jeffery C. S., 2005, in Koester D., Moehler S., eds, *Astronomical Society of the Pacific Conference Series Vol. 334*, 14th European Workshop on White Dwarfs. pp 291–+
- Ahmad A., Jeffery C. S., Solheim J.-E., Ostensen R., 2004, *Ap&SS*, **291**, 435
- Ahmad A., Behara N. T., Jeffery C. S., Sahin T., Woolf V. M., 2007, *A&A*, **465**, 541
- Anderson L., Grigsby J. A., 1991, in Crivellari L., Hubeny I., Hummer D. G., eds, *NATO Advanced Science Institutes (ASI) Series C Vol. 341*, NATO Advanced Science Institutes (ASI) Series C. p. 365
- Aznar Cuadrado R., Jeffery C. S., 2001, *A&A*, **368**, 994
- Beers T. C., Doinidis S. P., Griffin K. E., Preston G. W., Shectman S. A., 1992, *AJ*, **103**, 267
- Behara N. T., Jeffery C. S., 2006, *A&A*, **451**, 643
- Behara N. T., Jeffery C. S., 2008, in Heber U., Jeffery C. S., Napiwotzki R., eds, *Astronomical Society of the Pacific Conference Series Vol. 392*, Hot Subdwarf Stars and Related Objects. pp 87–+
- Beliere E., 2018, Bsc thesis, Trinity College Dublin
- Berger J., Fringant A. M., 1980a, *A&AS*, **39**, 39
- Berger J., Fringant A.-M., 1980b, *A&A*, **85**, 367
- Bianchi L., Shiao B., Thilker D., 2017, *ApJS*, **230**, 24
- Bramall D. G., Sharples R., Tyas L., et al. 2010, in *Ground-based and Airborne Instrumentation for Astronomy III*. p. 77354F, doi:10.1117/12.856382
- Burgh E. B., Nordsieck K. H., Kobulnicky H. A., Williams T. B., O’Donoghue D., Smith M. P., Percival J. W., 2003, in Iye M., Moorwood A. F. M., eds, *Proc. SPIE Vol. 4841*, Instrument Design and Performance for Optical/Infrared Ground-based Telescopes. pp 1463–1471, doi:10.1117/12.460312

- Carnochan D. J., Wilson R., 1983, *MNRAS*, **202**, 317
- Chavira E., 1958, Boletín de los Observatorios Tonantzintla y Tacubaya, **3**, 15
- Crawford S. M., Still M., Schellart P., et al. 2010, in *Observatory Operations: Strategies, Processes, and Systems III*. p. 773725, doi:10.1117/12.857000
- Crawford S. M., Crause L., Depagne É., et al. 2016, in *Ground-based and Airborne Instrumentation for Astronomy VI*. p. 99082L, doi:10.1117/12.2232653
- Demers S., Wesemael F., Irwin M. J., Fontaine G., Lamontagne R., Kepler S. O., Holberg J. B., 1990, *ApJ*, **351**, 271
- Dorsch M., Latour M., Heber U., Irrgang A., Charpinet S., Jeffery C. S., 2020, arXiv e-prints, p. arXiv:2009.09032
- Dreizler S., Heber U., Werner K., Moehler S., de Boer K. S., 1990, *A&A*, **235**, 234
- Drilling J. S., Beers T. C., 1995, *ApJ*, **446**, L27
- Drilling J. S., Jeffery C. S., Heber U., Moehler S., Napiwotzki R., 2013, *A&A*, **551**, A31
- Feige J., 1958, *ApJ*, **128**, 267
- Gaia Collaboration 2018, CDS/ADC Collection of Electronic Catalogues, **1345**, 0
- Geier S., Østensen R. H., Nemeth P., Gentile Fusillo N. P., Gänsicke B. T., Telting J. H., Green E. M., Schaffnerroth J., 2017, *A&A*, **600**, A50
- Green R. F., Schmidt M., Liebert J., 1986, *ApJS*, **61**, 305
- Green E. M., et al., 2011, *ApJ*, **734**, 59
- Greenstein J. L., Sargent A. I., 1974, *ApJS*, **28**, 157
- Haro G., Luyten W. J., 1962, Boletín de los Observatorios Tonantzintla y Tacubaya, **3**, 37
- Harrison P. M., Jeffery C. S., 1997, *A&A*, **323**, 177
- Heber U., 2016, *PASP*, **128**, 2001
- Hirsch H., Heber U., 2009, *Journal of Physics Conference Series*, **172**, 012015
- Hubeny I., Lanz T., Jeffery C. S., 1994, CCP7 Newsletter on Analysis of Astronomical Spectra, pp 30–42
- Hügelmeier S. D., Dreizler S., Homeier D., Krziesiński J., Werner K., Nitta A., Kleinman S. J., 2006, *A&A*, **454**, 617
- Hunger K., Gruschinske J., Kudritzki R. P., Simon K. P., 1981, *A&A*, **95**, 244
- Husfeld D., Butler K., Heber U., Drilling J. S., 1989, *A&A*, **222**, 150
- Jaidée S., Lyngå G., 1969, *Arkiv for Astronomi*, **5**, 345
- Jeffery C. S., 1998, *MNRAS*, **294**, 391
- Jeffery C. S., 2017, *MNRAS*, **470**, 3557
- Jeffery C. S., Hamann W. R., 2010, *MNRAS*, **404**, 1698
- Jeffery C. S., Miszalski B., 2019, *MNRAS*, **489**, 1481
- Jeffery C. S., Hamill P. J., Harrison P. M., Jeffers S. V., 1998, *A&A*, **340**, 476
- Jeffery C. S., Woolf V. M., Pollacco D. L., 2001, *A&A*, **376**, 497
- Jeffery C. S., Neelamkodan N., Woolf V. M., Crawford S. M., Østensen R. H., 2017a, *Open Astronomy*, **26**, 202
- Jeffery C. S., Baran A. S., Behara N. T., et al. 2017b, *MNRAS*, **465**, 3101
- Kendall T. R., Dufton P. L., Keenan F. P., Beers T. C., Hambly N. C., 1997, *A&A*, **317**, 82
- Kepler S. O., et al., 2015, *MNRAS*, **446**, 4078
- Kilkenny D., 1988, *MNRAS*, **232**, 377
- Kilkenny D., Busse J., 1992, *MNRAS*, **258**, 57
- Kilkenny D., Lynas-Gray A. E., 1982, *MNRAS*, **198**, 873
- Kilkenny D., Muller S., 1989, *South African Astronomical Observatory Circular*, **13**, 69
- Kilkenny D., O'Donoghue D., Koen C., Stobie R. S., Chen A., 1997, *MNRAS*, **287**, 867
- Kilkenny D., O'Donoghue D., Worters H. L., Koen C., Hambly N., MacGillivray H., 2015, *MNRAS*, **453**, 1879
- Kilkenny D., Worters H. L., O'Donoghue D., Koen C., Koen T., Hambly N., MacGillivray H., Stobie R. S., 2016, *MNRAS*, **459**, 4343
- Kobulnicky H. A., Nordsieck K. H., Burgh E. B., Smith M. P., Percival J. W., Williams T. B., O'Donoghue D., 2003, in Iye M., Moorwood A. F. M., eds, *Proc. SPIE Vol. 4841, Instrument Design and Performance for Optical/Infrared Ground-based Telescopes*. p. 1634, doi:10.1117/12.460315
- Koen C., Miszalski B., Väisänen P., Koen T., 2017, *MNRAS*, **465**, 4723
- Kondo M., Noguchi T., Maehara H., 1984, *Annals of the Tokyo Astronomical Observatory*, **20**, 130
- Lamontagne R., Demers S., Wesemael F., Fontaine G., Irwin M. J., 2000, *AJ*, **119**, 241
- Latour M., Fontaine G., Brassard P., Green E. M., Chayer P., Randall S. K., 2011, *ApJ*, **733**, 100
- Latour M., Fontaine G., Green E., 2014, in van Grootel V., Green E., Fontaine G., Charpinet S., eds, *Astronomical Society of the Pacific Conference Series Vol. 481, 6th Meeting on Hot Subdwarf Stars and Related Objects*. p. 91 (arXiv:1307.6112)
- Lei Z., Zhao J., Németh P., Zhao G., 2020, *ApJ*, **889**, 117
- Löbbling L., 2020, *MNRAS*, **497**, 67
- Luo Y.-P., Németh P., Liu C., Deng L.-C., Han Z.-W., 2016, *ApJ*, **818**, 202
- Luyten W. J., 1953, *AJ*, **58**, 75
- Moehler S., Richtler T., de Boer K. S., Dettmar R. J., Heber U., 1990a, *A&AS*, **86**, 53
- Moehler S., de Boer K. S., Heber U., 1990b, *A&A*, **239**, 265
- Moni Bidin C., Casetti-Dinescu D. I., Girard T. M., Zhang L., Méndez R. A., Vieira K., Korchagin V. I., van Alena W. F., 2017, *MNRAS*, **466**, 3077
- Napiwotzki R., 1997, *A&A*, **322**, 256
- Naslim N., Jeffery C. S., Ahmad A., Behara N. T., Şahin T., 2010, *MNRAS*, **409**, 582
- Naslim N., Jeffery C. S., Behara N. T., Hibbert A., 2011, *MNRAS*, **412**, 363
- Naslim N., Geier S., Jeffery C. S., Behara N. T., Woolf V. M., Classen L., 2012, *MNRAS*, **423**, 3031
- Naslim N., Jeffery C. S., Hibbert A., Behara N. T., 2013, *MNRAS*, **434**, 1920
- Naslim N., Jeffery C. S., Woolf V. M., 2020, *MNRAS*, **491**, 874
- Nassau J. J., Stephenson C. B., 1963, *Hamburger Sternw. Warner & Swasey Obs.*, **C04**, 0
- Németh P., Kawka A., Vennes S., 2012, *MNRAS*, **427**, 2180
- Nemeth P., Østensen R., Tremblay P., Hubeny I., 2014, in van Grootel V., Green E., Fontaine G., Charpinet S., eds, *Astronomical Society of the Pacific Conference Series Vol. 481, 6th Meeting on Hot Subdwarf Stars and Related Objects*. p. 95 (arXiv:1308.0252)
- O'Donoghue D., Kilkenny D., Koen C., Hambly N., MacGillivray H., Stobie R. S., 2013, *MNRAS*, **431**, 240
- Østensen R. H., 2006, *Baltic Astronomy*, **15**, 85
- Pereira C., 2011, PhD thesis, Queen's University Belfast
- Randall S. K., Bagnulo S., Ziegerer E., Geier S., Fontaine G., 2015, *A&A*, **576**, A65
- Rodríguez-López C., Ulla A., Garrido R., 2007, *MNRAS*, **379**, 1123
- Saffer R. A., Bergeron P., Koester D., Liebert J., 1994, *ApJ*, **432**, 351
- Schindewolf M., Németh P., Heber U., Battich T., Bertolami M. M. M., Latour M., 2018a, *Open Astronomy*, **27**, 27
- Schindewolf M., Németh P., Heber U., Battich T., Miller Bertolami M. M., Irrgang A., Latour M., 2018b, *A&A*, **620**, A36
- Slettebak A., Brundage R. K., 1971, *AJ*, **76**, 338
- Stephenson C. B., Sanduleak N., 1971, *Publications of the Warner & Swasey Observatory*, **1**
- Stobie R. S., Kilkenny D., O'Donoghue D., et al. 1997a, *MNRAS*, **287**, 848
- Stobie R. S., Kilkenny D., O'Donoghue D., et al. 1997b, in *Stobie et al. (1997a)*, p. 848
- Ströer A., Heber U., Lisker T., Napiwotzki R., Dreizler S., Christlieb N., Reimers D., 2007, *A&A*, **462**, 269
- Thejll P., Bauer F., Saffer R., Liebert J., Kunze D., Shipman H. L., 1994, *ApJ*, **433**, 819
- Vennes S., Kawka A., Németh P., 2011, *MNRAS*, **410**, 2095
- Viton M., Deleuil M., Tobin W., Prevot L., Bouchet P., 1991, *A&A*, **242**, 175
- Voss B., Koester D., Napiwotzki R., Christlieb N., Reimers D., 2007, *A&A*, **470**, 1079
- Wenger M., et al., 2000, *A&AS*, **143**, 9
- Wisotzki L., Koehler T., Groote D., Reimers D., 1996, *A&AS*, **115**, 227
- Woolf V. M., Jeffery C. S., 2000, *A&A*, **358**, 1001
- Zhang X., Jeffery C. S., 2012, *MNRAS*, **419**, 452
- Şener H. T., Jeffery C. S., 2014, *MNRAS*, **440**, 2676
- Şener-Şatir H. T., 2015, PhD thesis, Queen's University of Belfast
- van Dokkum P. G., 2001, *PASP*, **113**, 1420

The SALT survey of helium-rich hot subdwarfs: methods, classification, and coarse analysis.

Supplementary Online Material

C. S. Jeffery¹, B. Miszalski² and E. Snowdon¹

¹*Armagh Observatory and Planetarium*

²*Australian Astronomical Optics - Macquarie, Faculty of Science and Engineering, Macquarie University, North Ryde, NSW 2113, Australia*

20 November 2020

APPENDIX A: SALT OBSERVATION DATES

Table A.1 provides dates on which SALT obtained data with either RSS or HRS for each star classified in Table 2. Full details are available in the SALT archives.

APPENDIX B: CLASSIFICATION VERIFICATION

Figure B.1 compares automatic classifications obtained by applying the algorithms described in §3.1 with the manual classifications given by ? (D13). The observational data are the same for both sets of classification.

APPENDIX C: MODEL ATMOSPHERES

Models selected from the grids described in §4.1 are presented and compared. Figures C.1 and C.2 demonstrate the transition of the theoretical spectrum from helium-poor to helium-rich ($-2 \leq \log y \leq 2$ and from $25 \leq T_{\text{eff}}/\text{kK} \leq 55$). Metal-poor and solar-metallicity STERNE/SPECTRUM LTE models are compared with the TLUSTY/SYNSPEC non-LTE zero-metal models of ?. All models are computed for a surface gravity $\log g = 5.75$ characteristic of the majority of stars analysed in this paper.

APPENDIX D: CLASSIFICATION CALIBRATION

D13 provides approximate calibrations between spectral type and T_{eff} and between luminosity class and $\log g$ for restricted subsets of their sample. Figure D.1 compares effective temperature, surface gravity and helium-to-hydrogen ratio ($T_{\text{eff}}, \log g, \log y$) as determined in §4 with the corresponding spectral type, luminosity and helium classes as determined in §3.

APPENDIX E: SPECTRAL ATLAS

Figs. E.1 - E.7 show the complete ensemble of reduced survey spectra and best-fit models arranged by subsection in §5 in the same format as Fig. 6.

arXiv:2011.09523v1 [astro-ph.SR] 18 Nov 2020

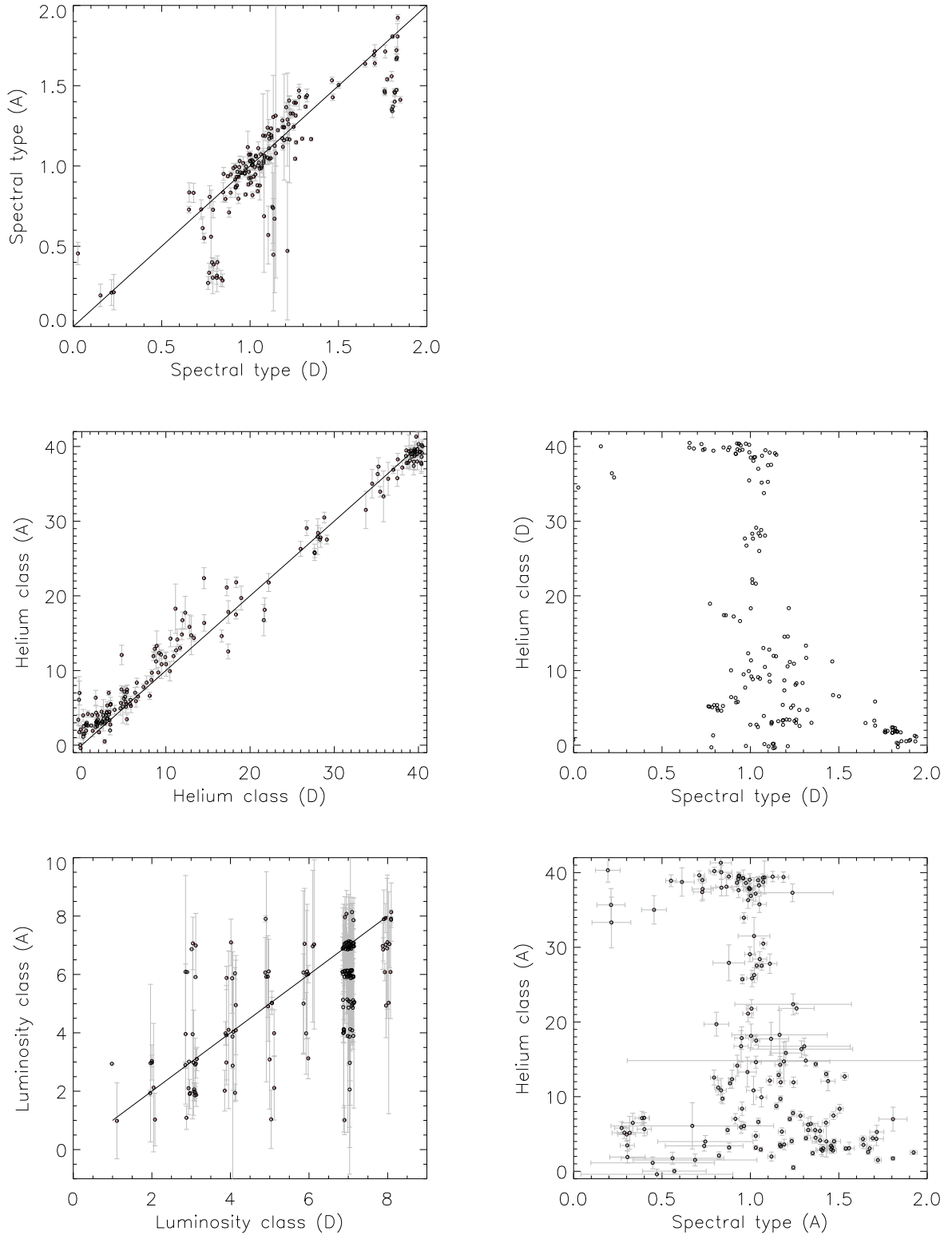


Figure B.1. Left: Comparison of automatic classifications (A) with D13 classifications (D) (Drilling sample). For visibility, all classification plots include a random jitter on intervals of ± 0.05 , ± 0.15 and ± 0.5 in SpT, LC and He respectively. Right: Comparison of the SpT – He diagram for D13 (top: D) and automatic (bottom: A) classifications (Drilling sample). If multiple spectra exist for the same star, each has been classified separately in the current exercise.

[h]

Table A.1. Observation dates in the form *yyyymmdd*.

Name	RSS Dates	HRS Dates
Ton S 144	20181101	20180611
Ton S 148	20191101	20180616 20180705 20180722 20190619 20190715
EC 00468–5440	20180801 20190617 20191114	
SB 705	20180823	20170706
LB 3229	20180823	20170716
PG 0208+016	20180823 20190717	20170713
LB 1630	20190715	
PG 0240+046	20180729 20190803	20171106 20181118 20191103 20191104
LB 3289	20180729 20190714	20170827 20171028 20171105 20181118 20181119 20191103
EC 02523–6934	20190714 20191031 20191101	
EC 02527–7111	20190814 20191117	
PHL 1466	20190817	
EC 03505–6929	20190917	
EC 04013–4017	20180730 20190717	20181118 20191102 20191105
GLX J04111–0048	20180817	20170116 20170906 20190916 20191012
EC 04110–1348	20190727	
HE 0414–5429	20191108	
2M 0420+0120	20191103	20170113 20181117 20181118
HE 0421–5415	20190717	
EC 04271–2909	20191107	
EC 04281–4738	20190907	
EC 04299–1651	20180801 20190814	
LB 1741	20191004	
BPS 29520–0048	20190814	
HE 0440–3211	20190917	
EC 04517–3706	20181110	
GLX J05138–1944	20190814	
Ton S 415	20180823 20191102	20170316
EC 05242–2900	20200208	
GLX J05580–2927	20191207	
EC 05593–5901	20180823 20190917	
GLX J06126–2712	20181216	20170909
GLX J07076–6222	20180915 20191010	20180414
GLX J07158–5407		20170124
GLX J07581–0432	20181024 20181122	20161115 20161126
UVO 0832–01	20191115	
GLX J08454–1214	20191103 20191116	20170314 20170315
PG 0902+057	20181217	20170126
UVO 0904–02	20191210	
LSS 1274	20191127	
EC 09557–1551	20181123	
PG 0958–119	20191210	
EC 10475–2703		20170602
EC 10479–2714	20181214	
EC 11236–1945	20181214	
PG 1127+019	20190105 20190420	20170119 20180109 20180128
PG 1220–056	20200111	
PG 1230+067	20200124	20170131
EC 12349–2824	20190117	
EC 12420–2732	20190104	
PG 1318+062	20190330 20190620	20190206
EC 13290–1933	20180612	
GLX J14258–0432		20170416 20170514
PG 1455–069	20180628 20180824	
GLX J15235–1817	20180605	20170711

Table A.1. (contd.)

Name	RSS Dates	HRS Dates
PG 1528+029	20180630 20190430	
EC 15348–1652	20180821 20190818	
PG 1537–046	20190501	
PG 1625–034	20190720	
GLX J16546+0318	20180630	
GLX J17051–7156	20200322	20170331 20180428 20180429
GLX J18325–4744		20170315 20170703
GLX J18372–3125		20170629
GLX J18387–5409	20180516	20170415 20170514
GLX J18459–4138	20180526	20170316 20170317 20170420 20170516
GLX J19059–4438		20170618
GLX J19108–4417	20180516	20170506
GLX J19111–1406		20170615
GLX J19150–4235	20180824	20170704
GLX J19333–2345	20180815 20190419	
GLX J19376–4303	20180513	20170510
BPS 22896–0128	20190615 20191025 20191102	
EC 19529–4430	20180516	20190323 20190329
GLX J20133–1201	20190709	
EC 20111–3724	20190427	
EC 20111–6902	20180628 20190424 20191103 20191104	
GLX J20204–1901	20180818 20181026 20190713	
EC 20184–3435	20180705	
EC 20187–4939	20180517	20160525
GLX J20251–0804	20180703	20170704
EC 20221–6249	20180604	20170403
EC 20236–5703	20190619	20190403
BPS 22940–0009	20160612 20180504	20160622 20160629 20180506 20190424 20170404 20170416 20170614
EC 20306–5127	20180816	
EC 20337–2525	20190720	
EC 20450–1501	20180801	20160511
EC 20450–6947	20180727 20180801	
EC 20481–5518	20190614 20191113	
LS IV–14 116	20190427 20190501	
EC 20577–5641	20180822	
Ton S 14	20190617	
EC 21077–4815	20190817	
BPS 30319–0062	20180818	20190516 20190606
EC 21125–7013	20180627	
EC 21306–4911	20190709	
EC 21416–3645	20190617 20191109 20191111	
PHL 149	20180822	
PHL 178	20190617	
PG 2158+082	20190618	
BPS 22956–0090	20180628 20190521	20161031 20161101 20161106
BPS 22892–0051	20180822	
PB 7124	20180725	20170704
BPS 22875–0002	20180822	20170601
PG 2218+051	20191029	
EC 22332–6837	20190617 20191109	
BPS 22938–0044	20180604 20180612 20180628 20190514	
GLX J22565–5248	20180604	20170518 20181115
BPS 22938–0073	20180821	20170519
PHL 540	20190618	
Ton S 103	20180608	20161106 20170923
HE 2347–4130	20190521	

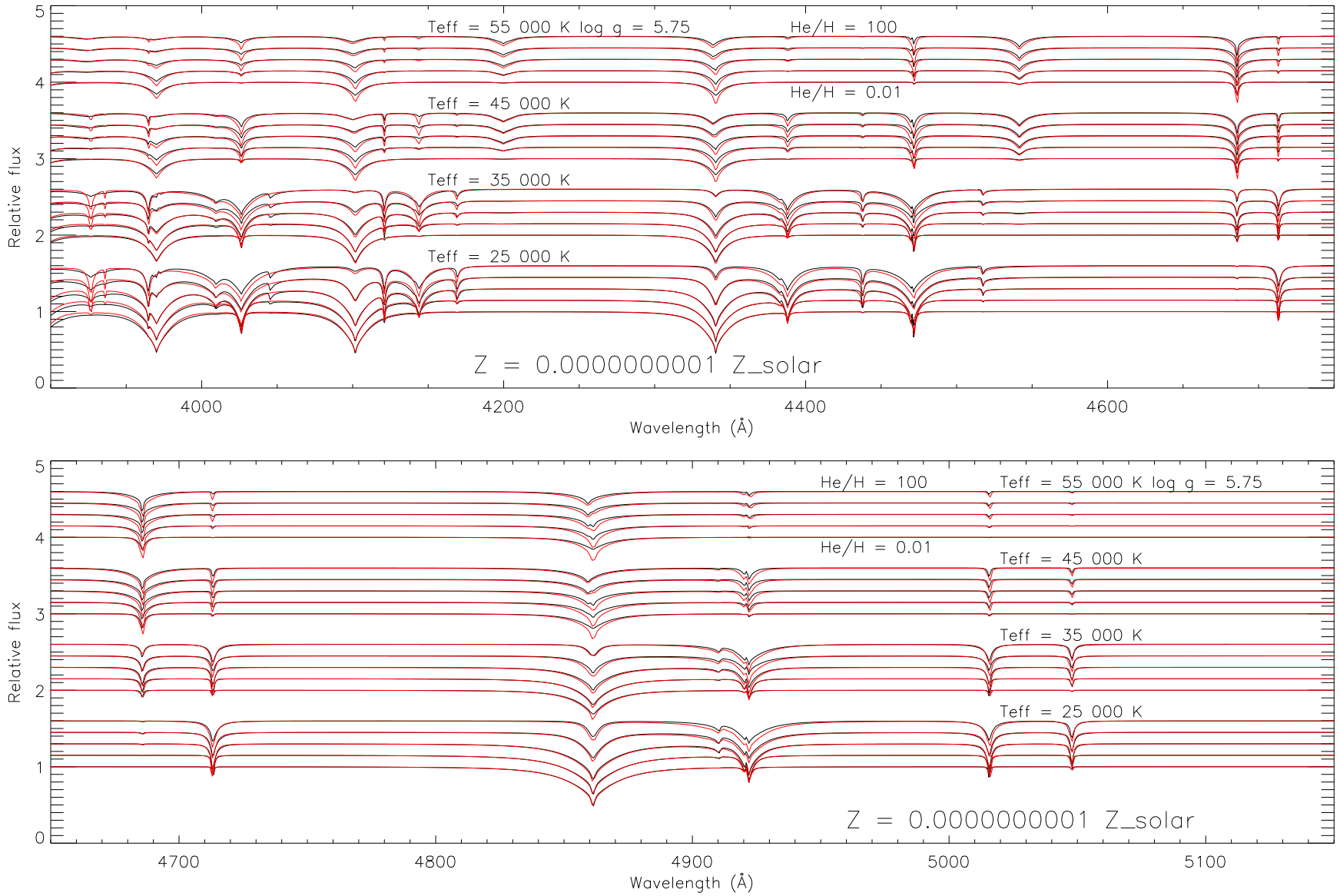


Figure C.1. A comparison of theoretical spectra for selected model atmospheres extracted from the grids described in § 4.1. STERNE/SPECTRUM LTE models with negligible abundance of elements heavier than helium ($\log Z/Z_{\odot} = -10$; black) are compared with TLUSTY/SYNSPEC non-LTE zero-metal models (red).

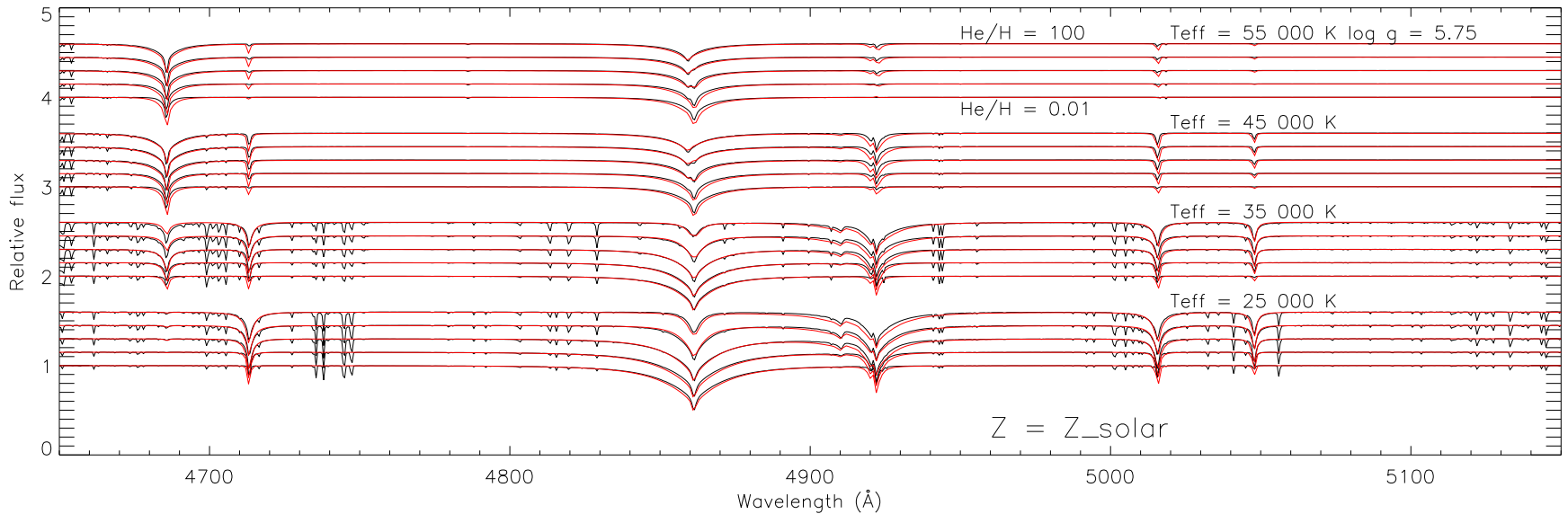
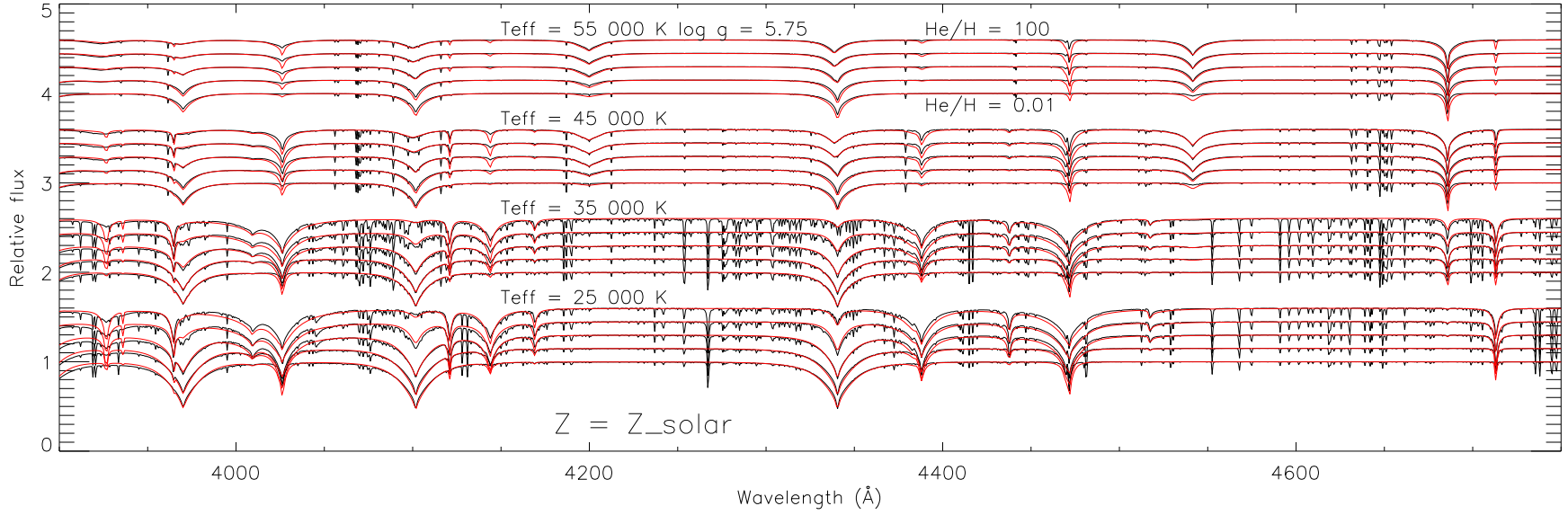


Figure C.2. As Fig. C.1 but for STERNE/SPECTRUM LTE models with solar metallicity (black).

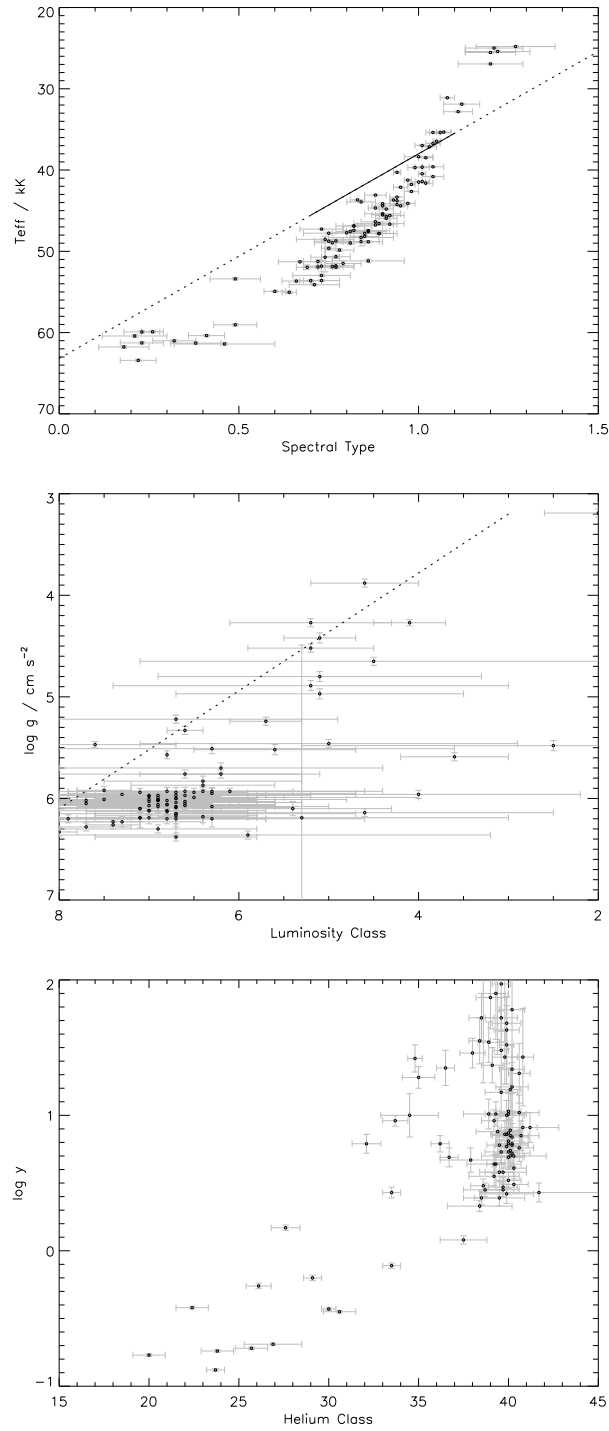


Figure D.1. T_{eff} , $\log g$ and $\log y$ from Fig. 3 are compared with spectral type, luminosity and helium classes from Table 2 (top to bottom). The dotted lines approximately represent calibrations presented in D13, shown as solid over regions where they are considered valid.

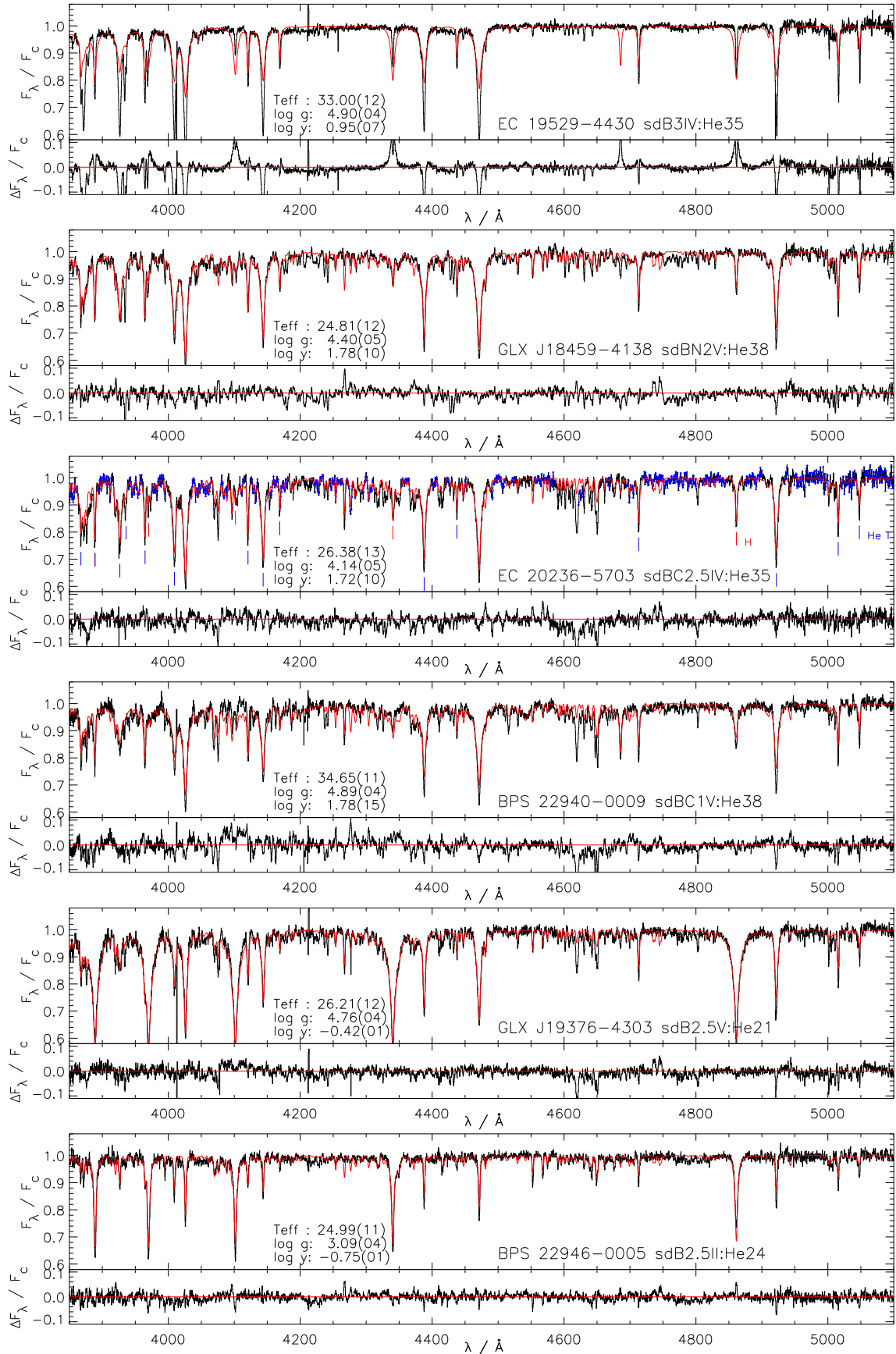


Figure E.1. As Fig. 6 for the stars discussed in § 5.1: SpT = sdB1 – sdB3, $LC \leq V$, $He > 20$

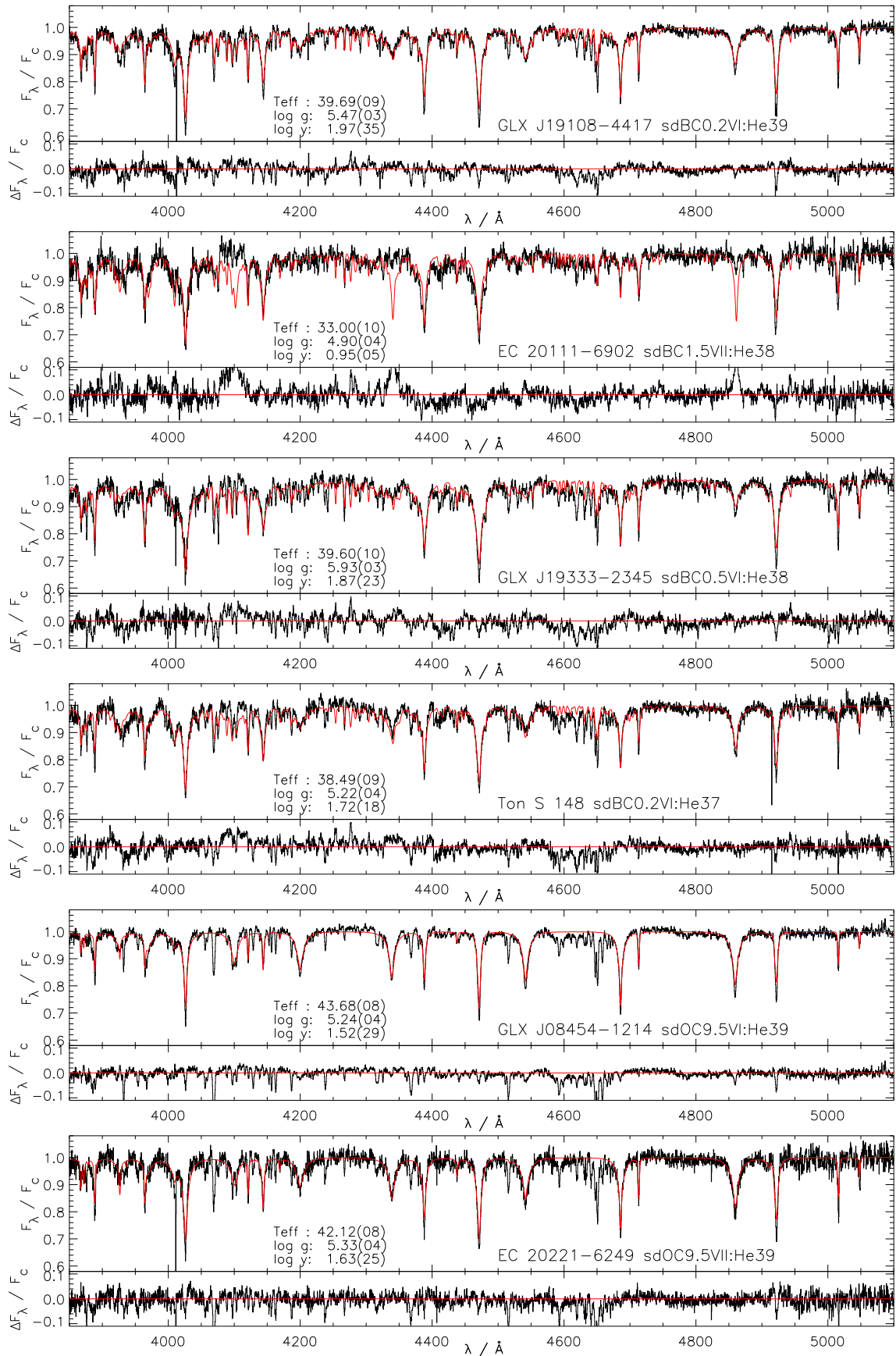


Figure E.2. As Fig. 6 for the stars discussed in § 5.2: SpT = sdO9.5 – sdB1, LC \approx V – VI, He > 30

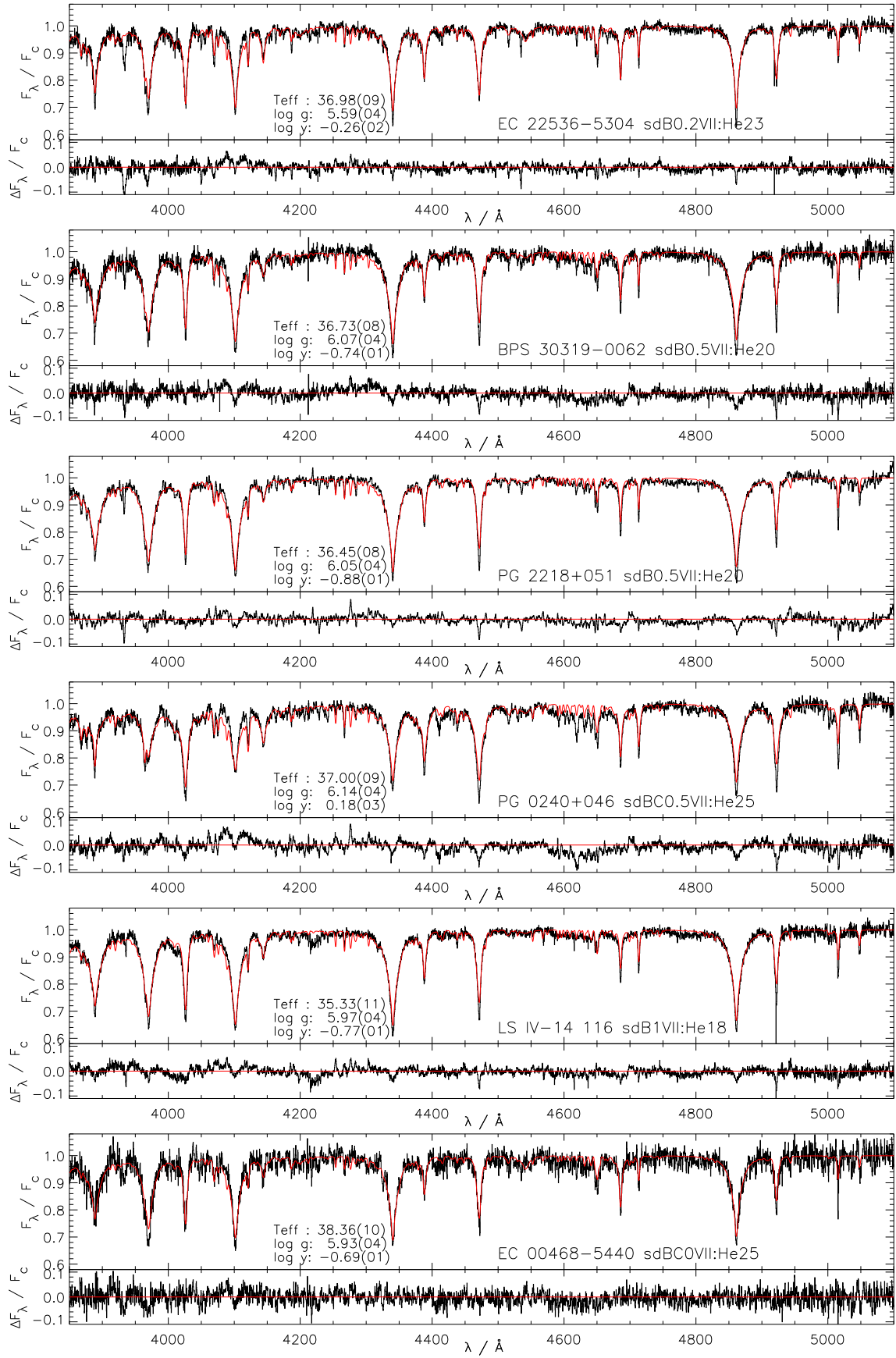


Figure E.3. As Fig. 6 for the stars discussed in § 5.3: sdB0 \leq Sp \leq sdB1, He < 25

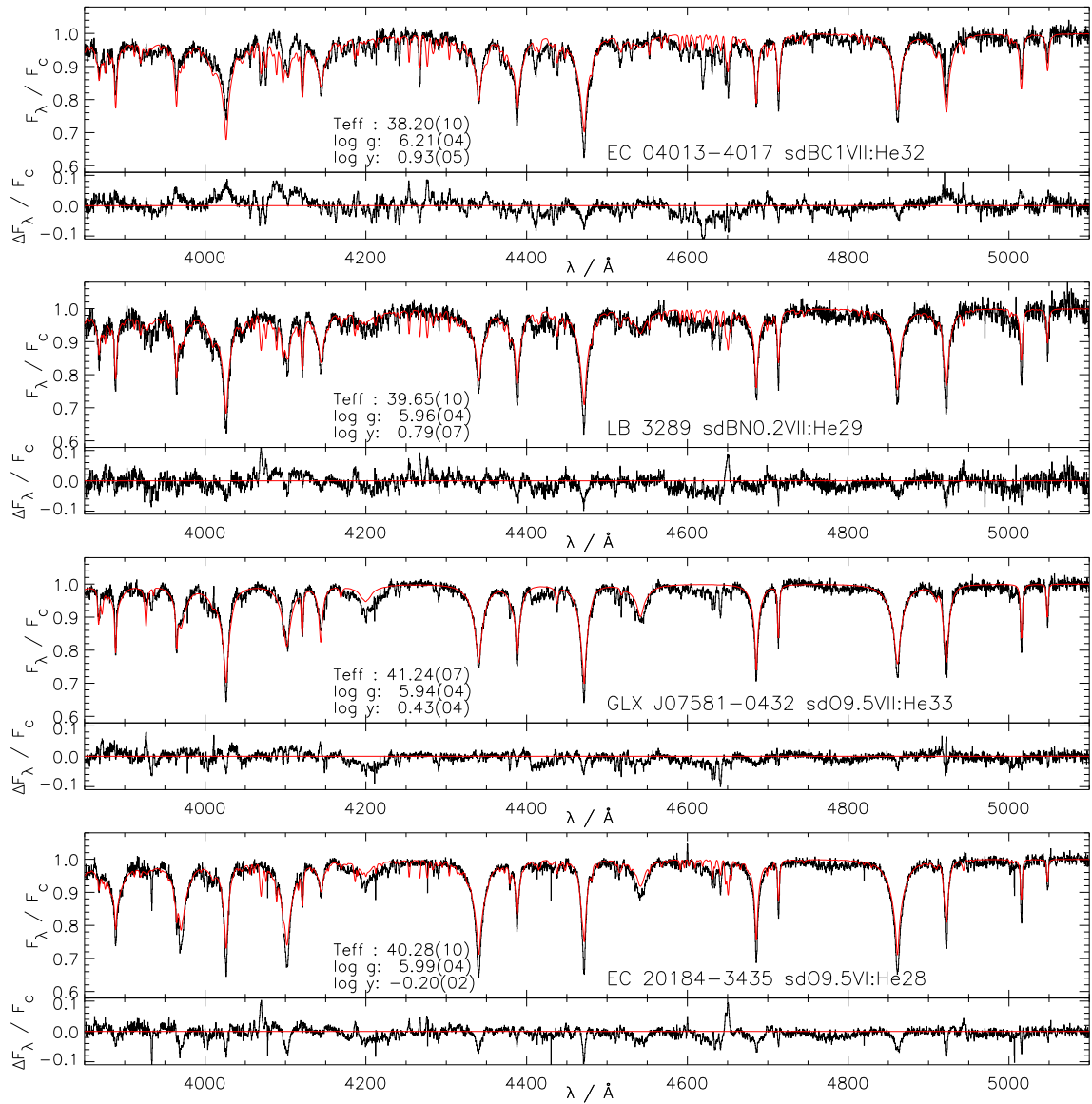


Figure E.4. As Fig. 6 for the stars discussed in § 5.4: $Sp = \text{sdO8} - \text{sdB1}$, $25 < He < 35$

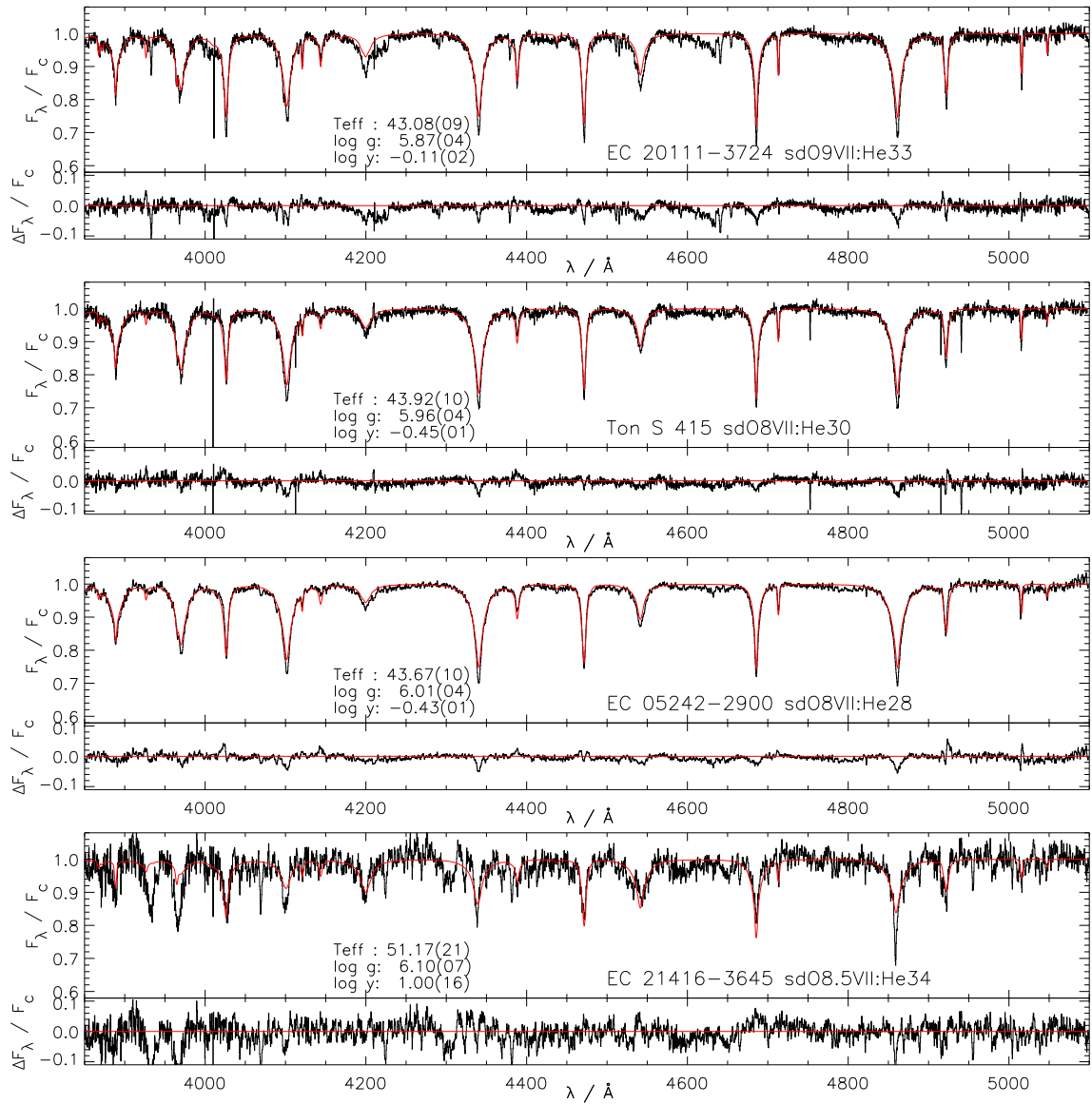


Figure E.4 – continued

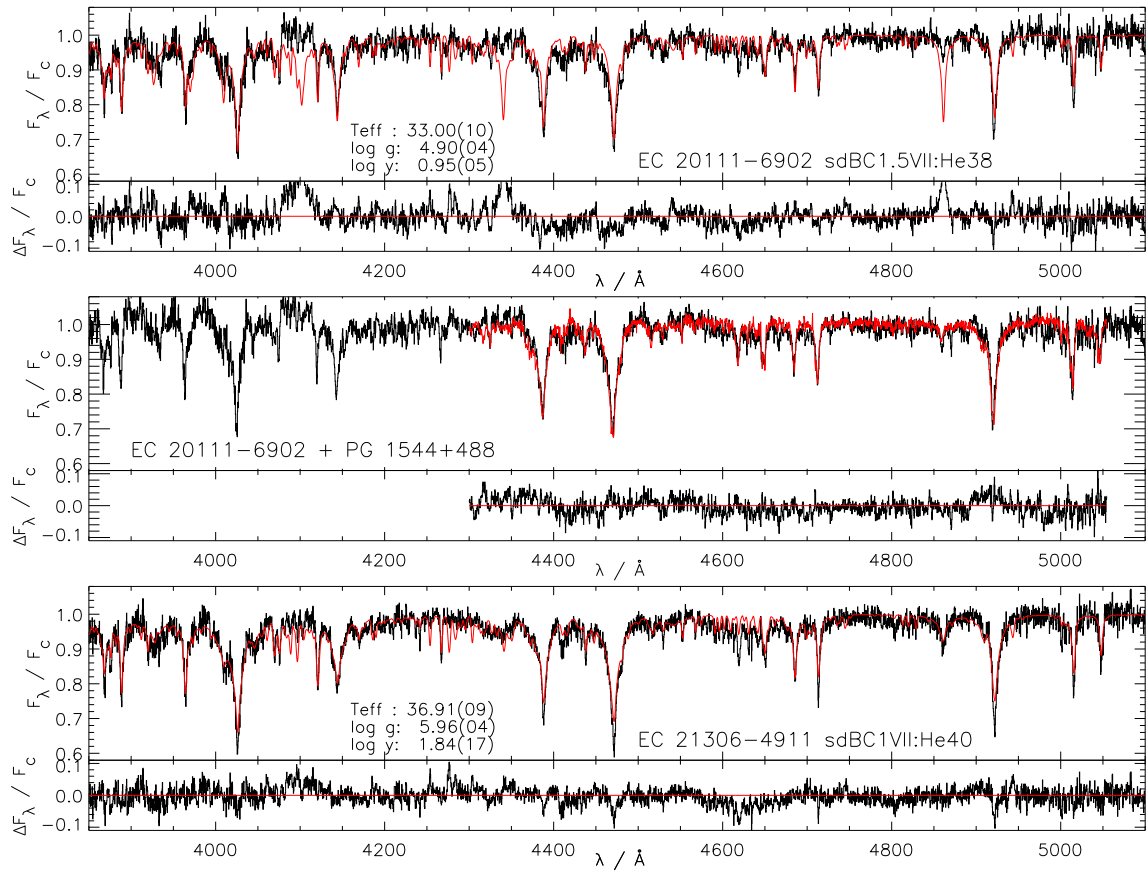
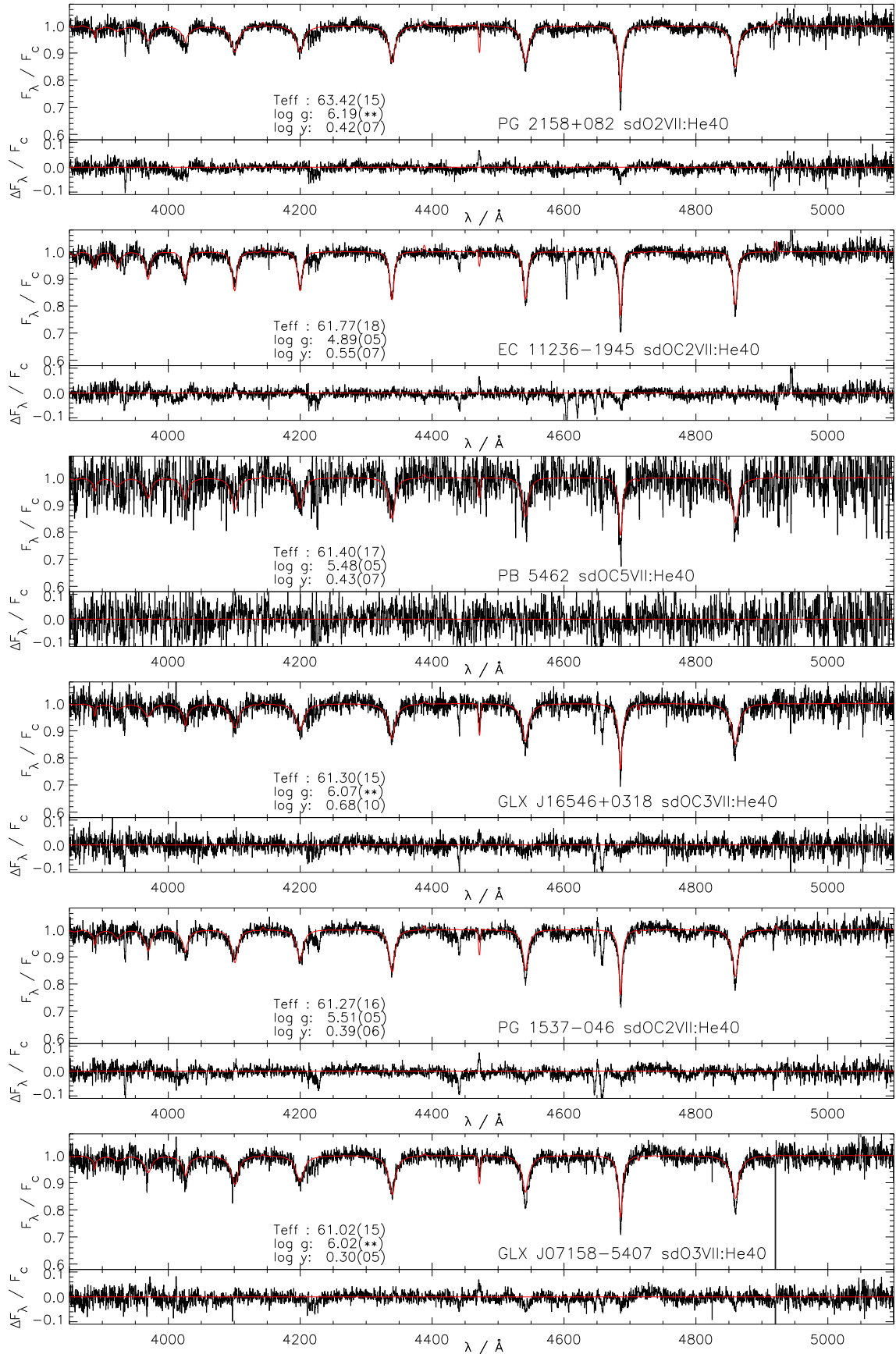


Figure E.5. As Fig. 6 for the stars discussed in § 5.6: broad lines

Figure E.6. As Fig. 6 for the stars discussed in § 5.7: $Sp \leq \text{sdO6}$

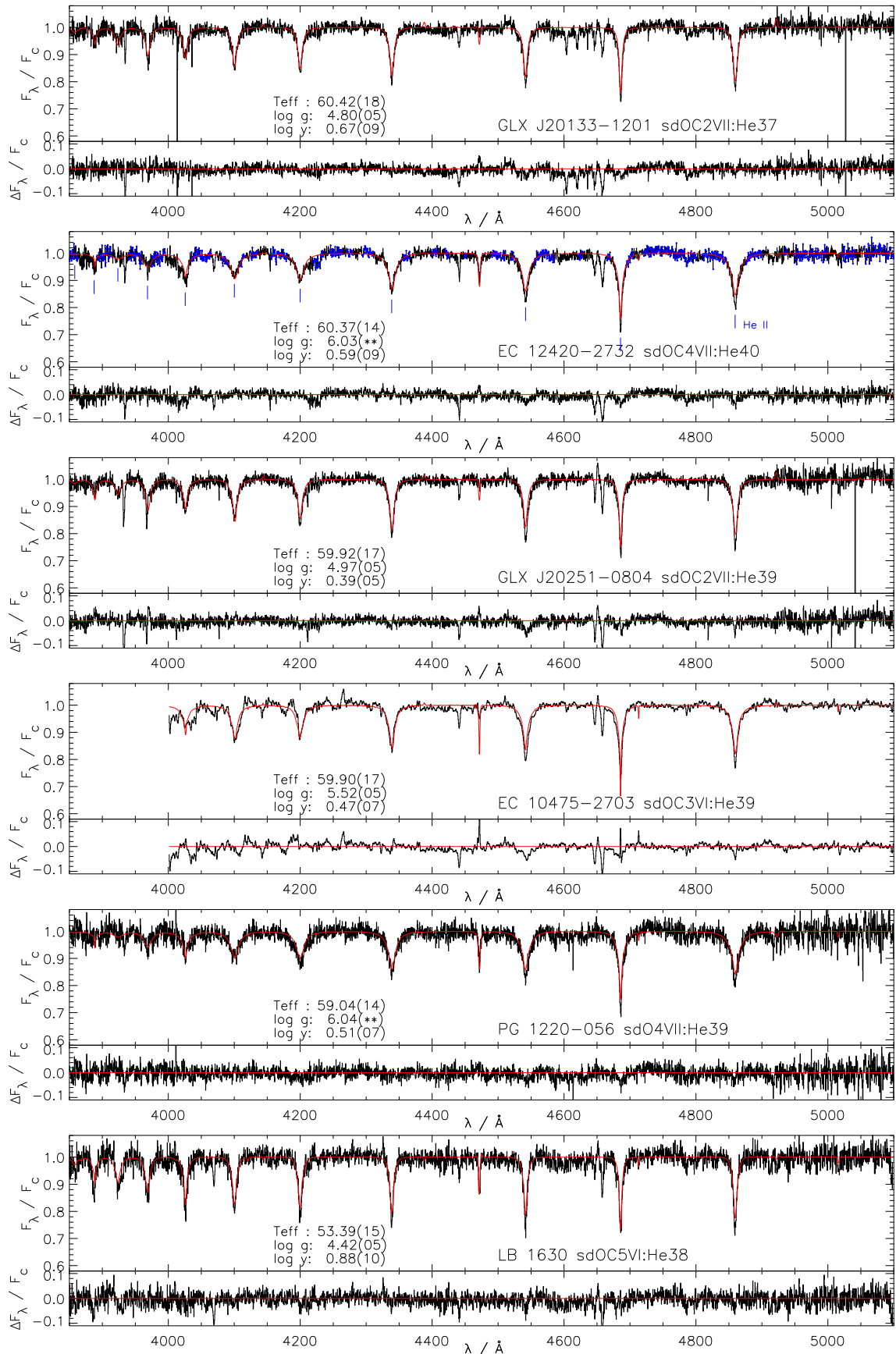


Figure E.6 – continued

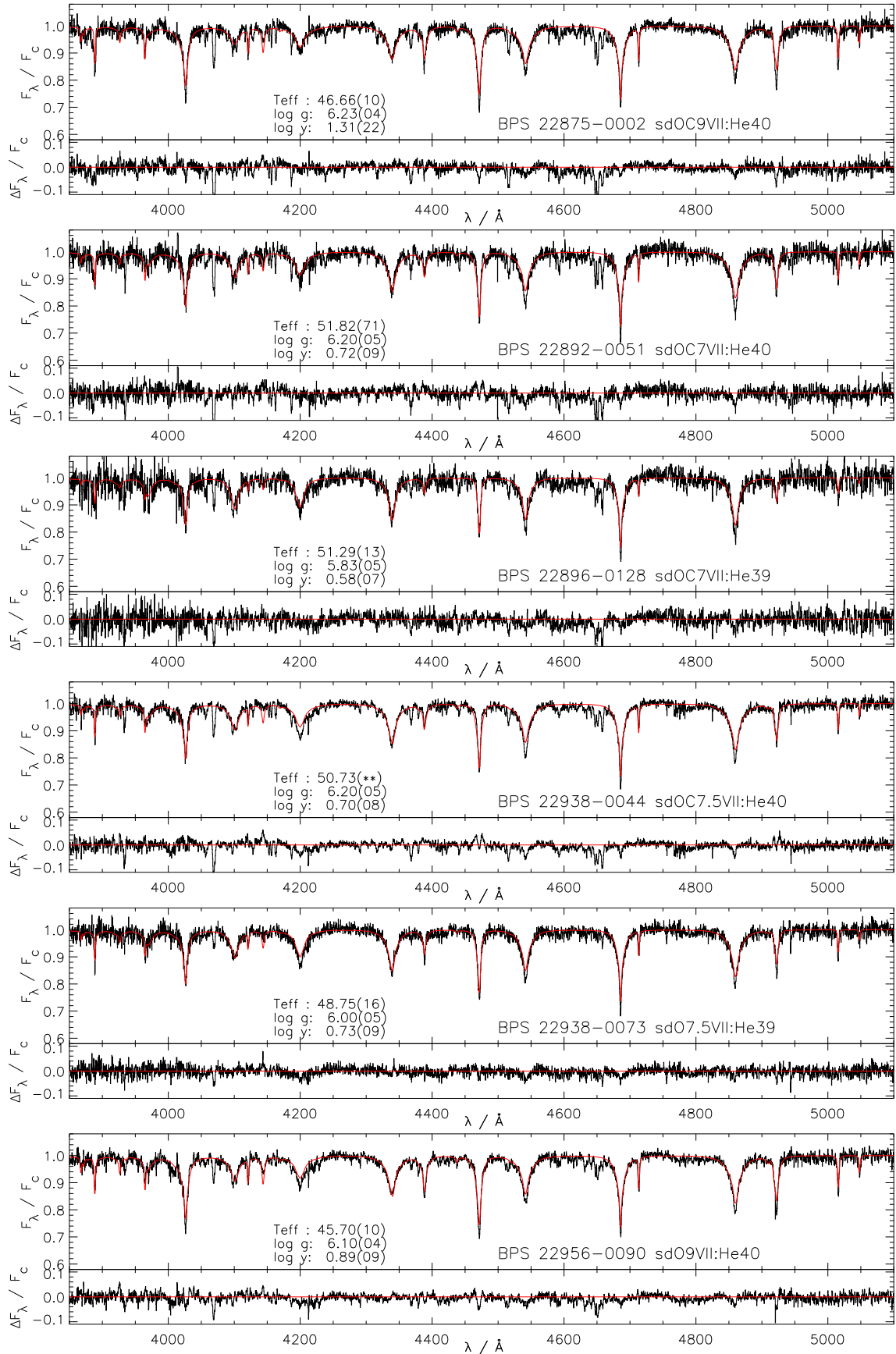


Figure E.7. As Fig. 6 for the stars discussed in § 5.8: Sp = sdO6.5 – sdB0.5, He \geq 35

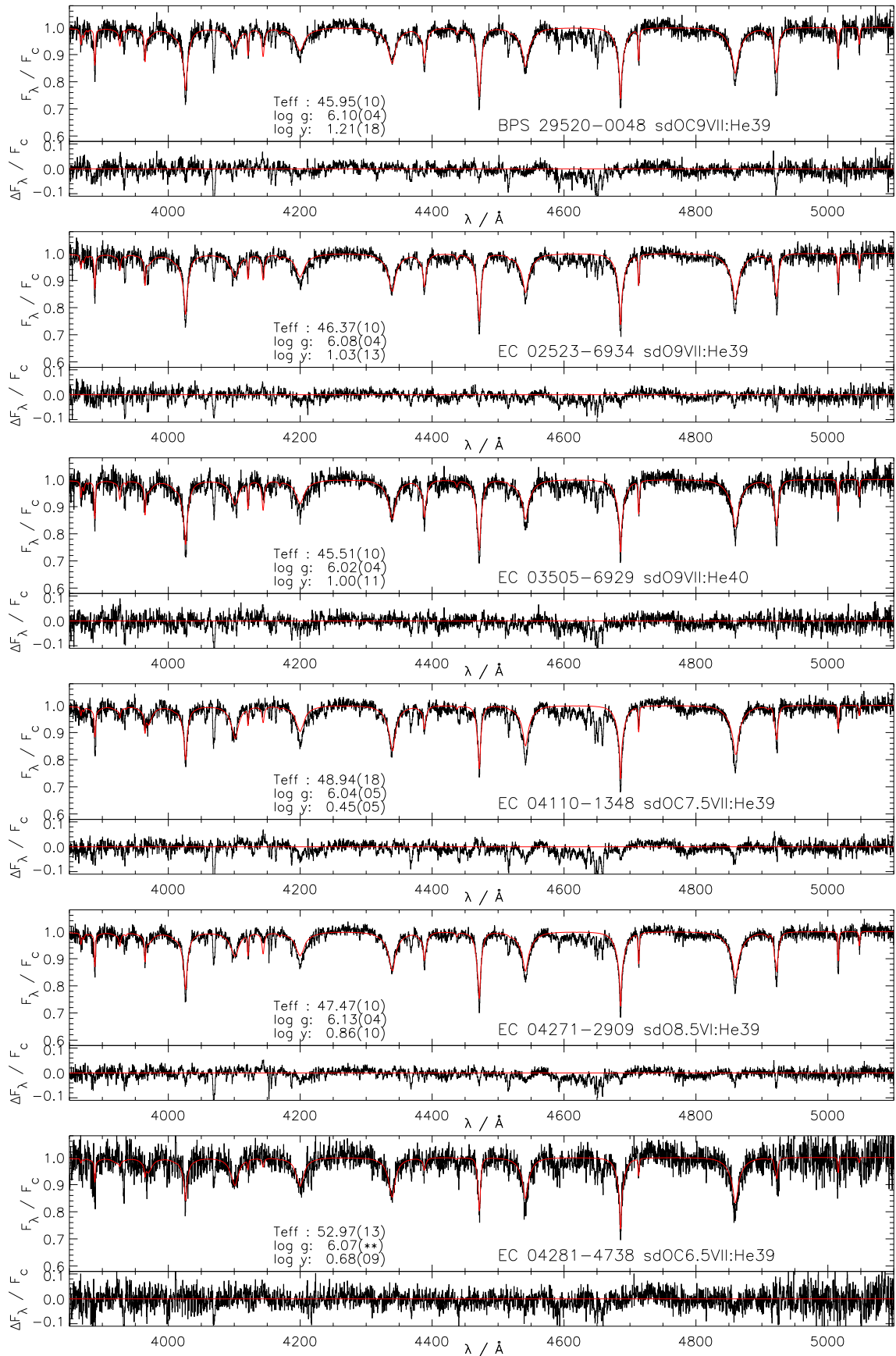


Figure E.7 – continued

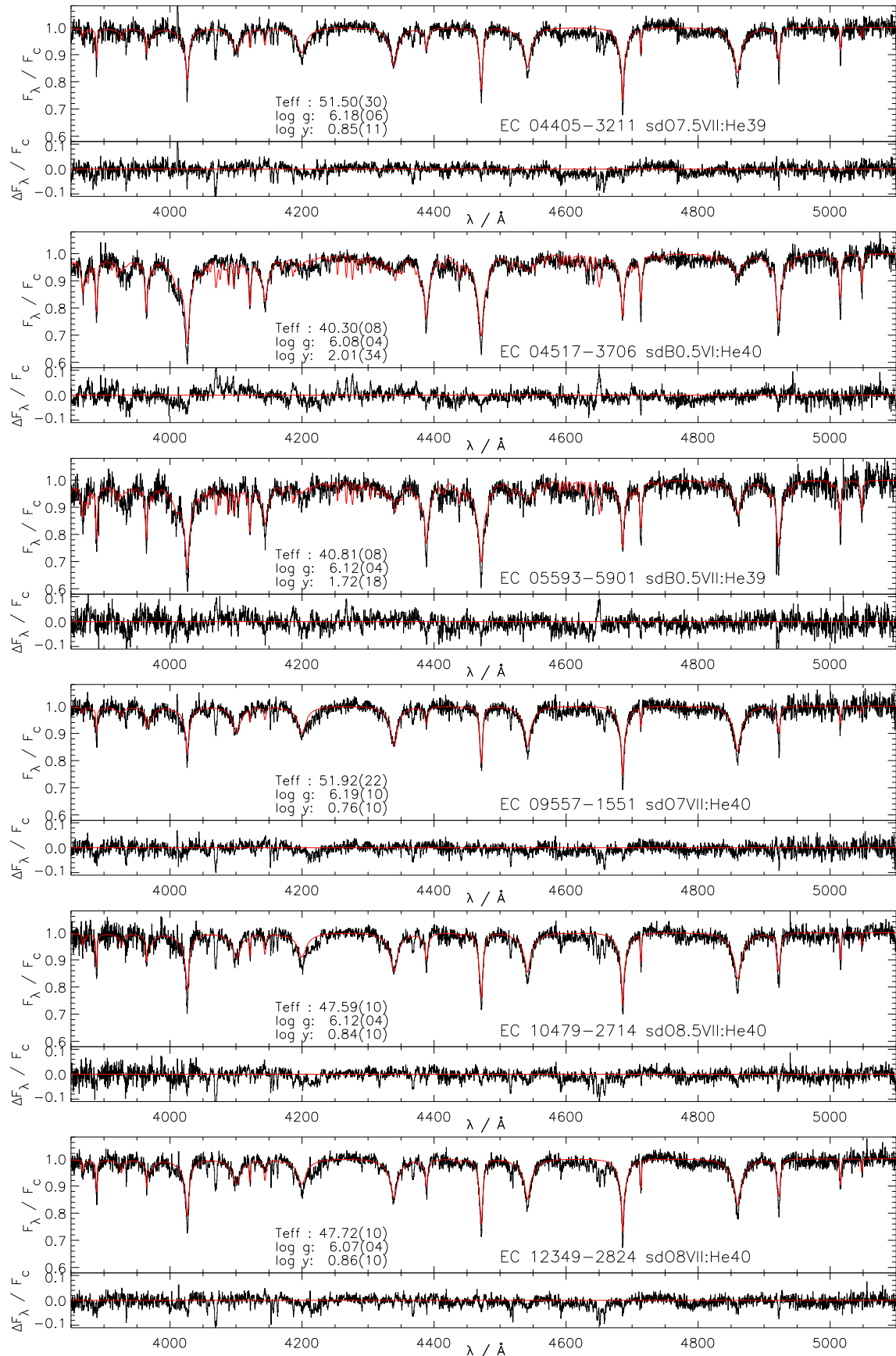


Figure E.7 – continued

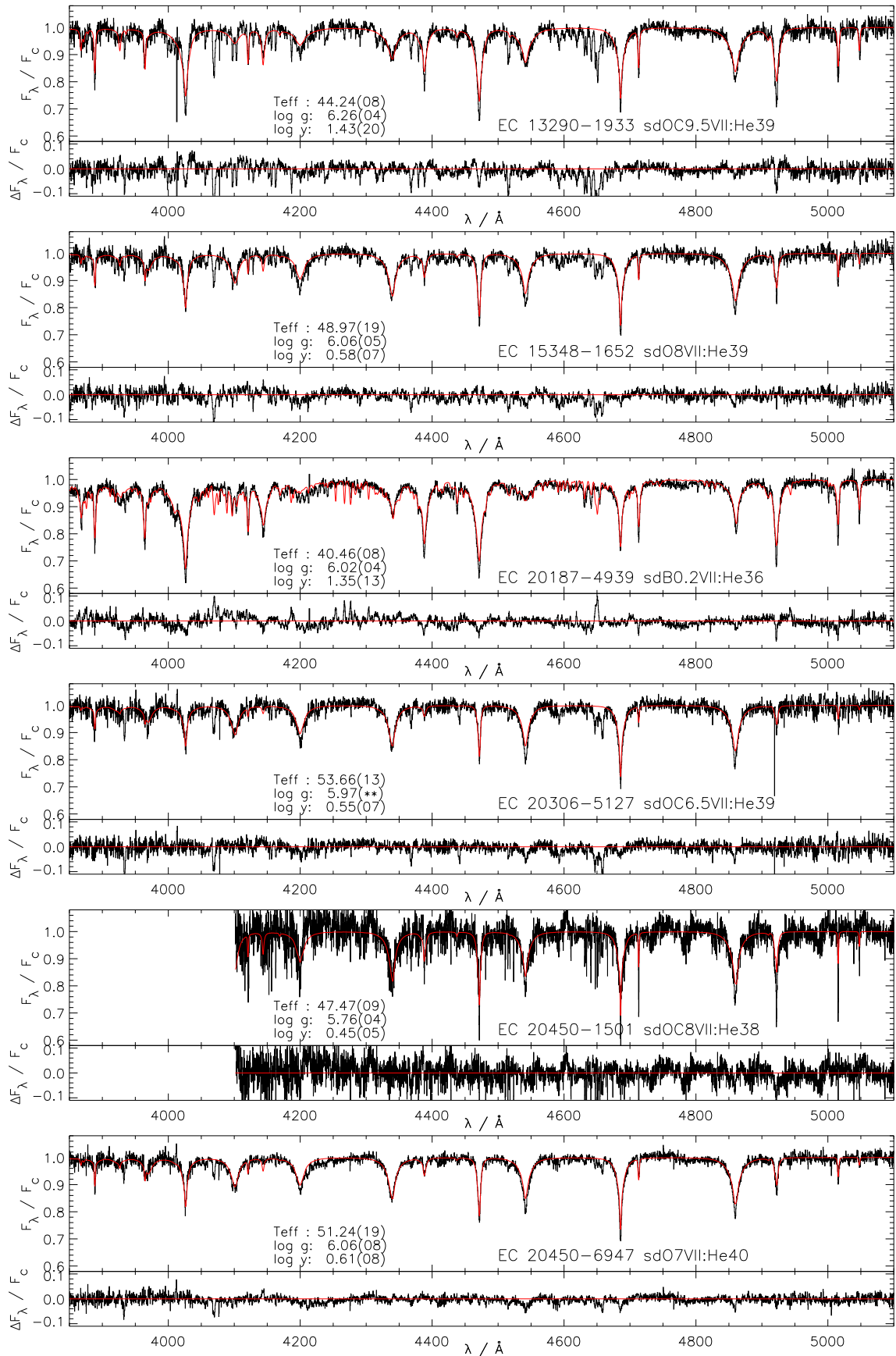


Figure E.7 – continued

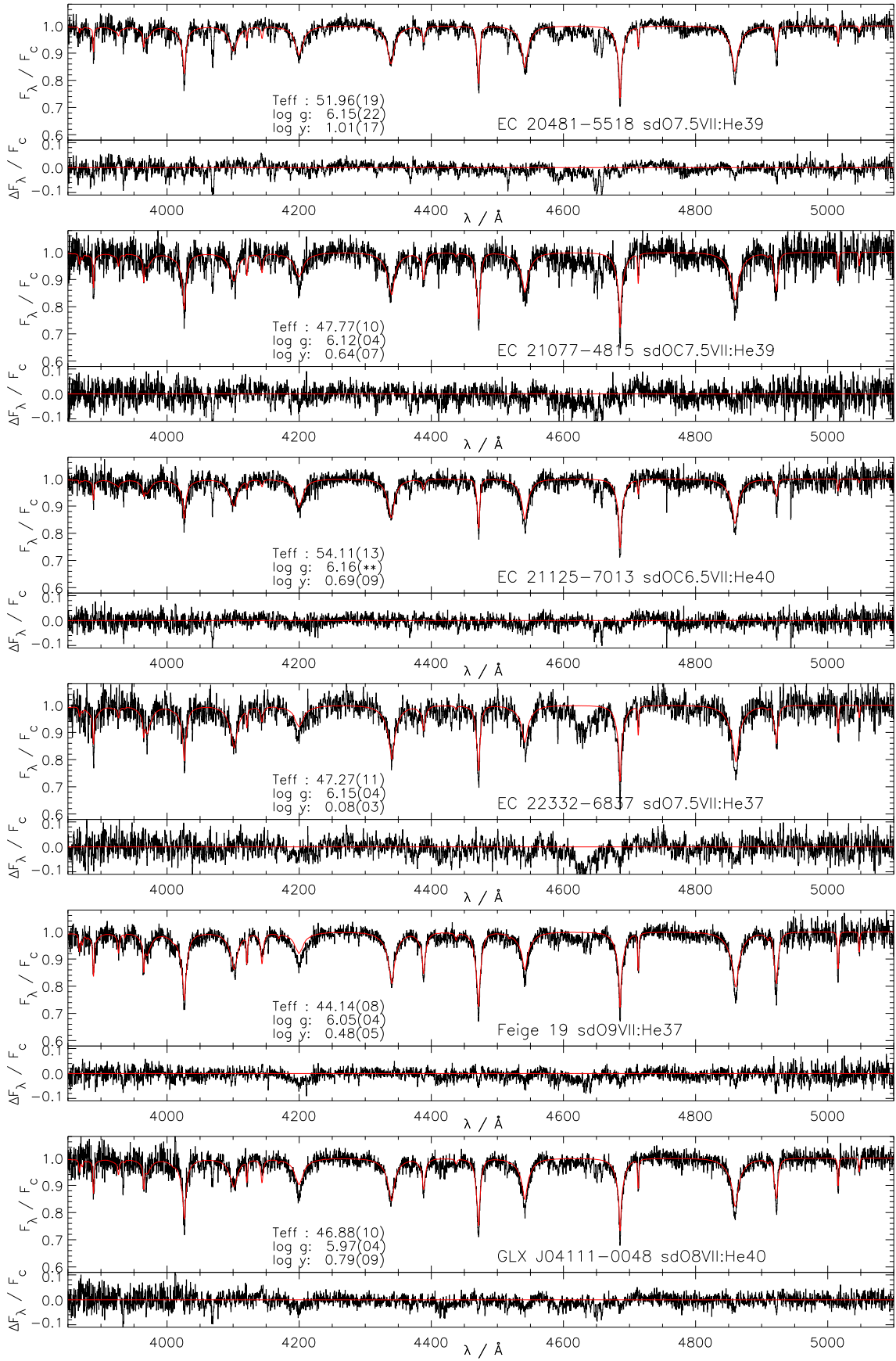


Figure E.7 – continued

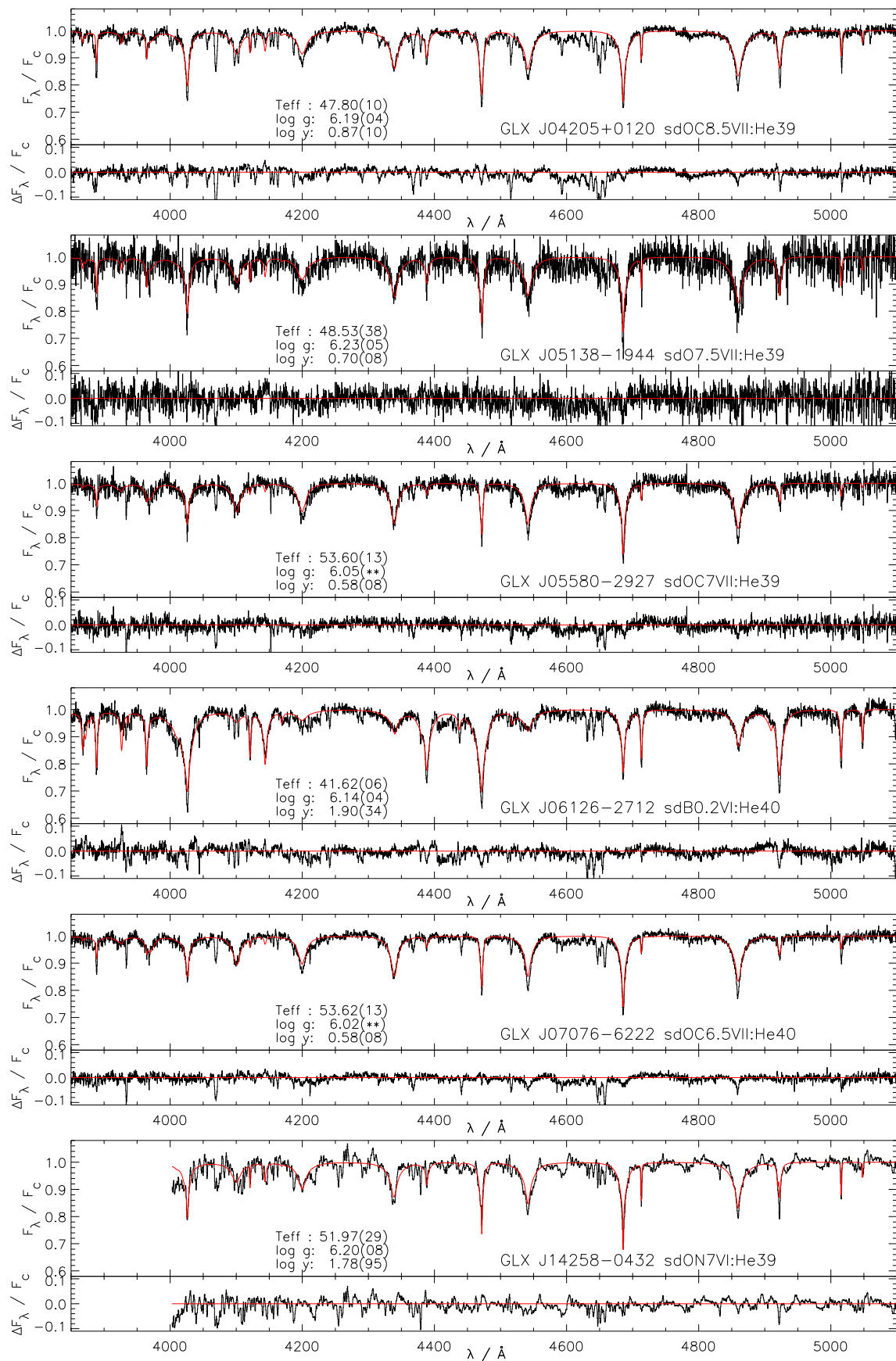


Figure E.7 – continued

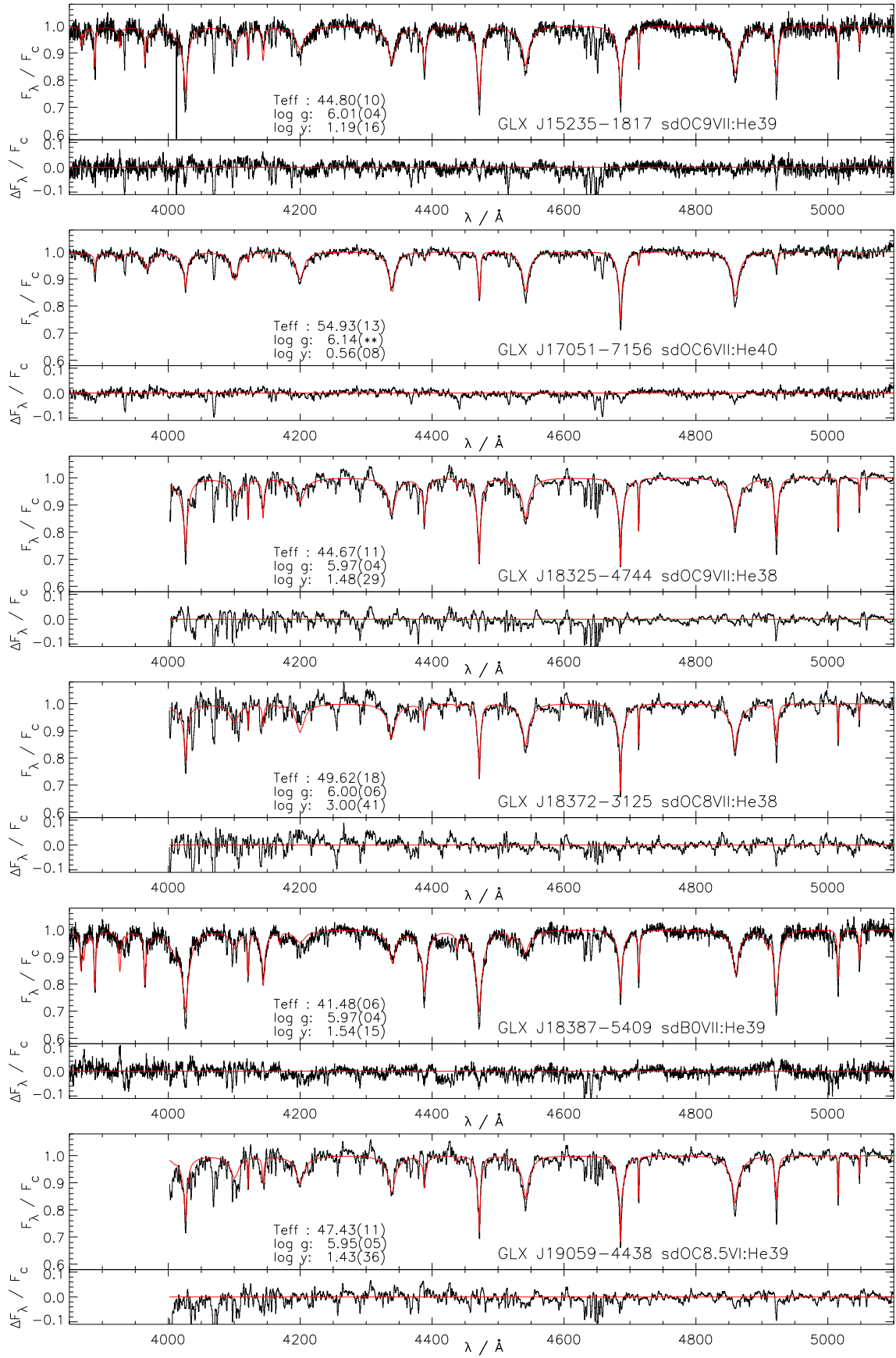


Figure E.7 – continued

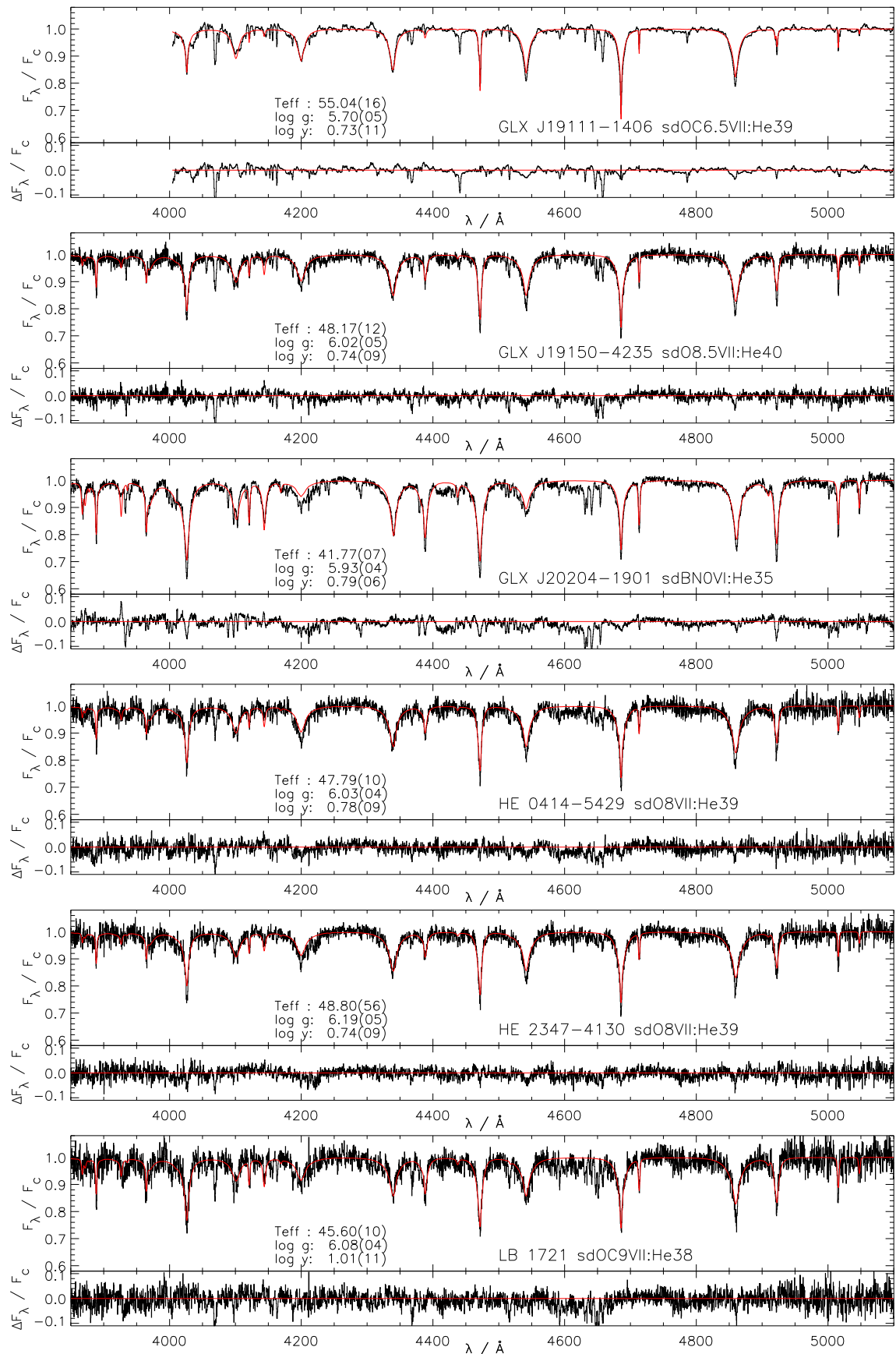


Figure E.7 – continued

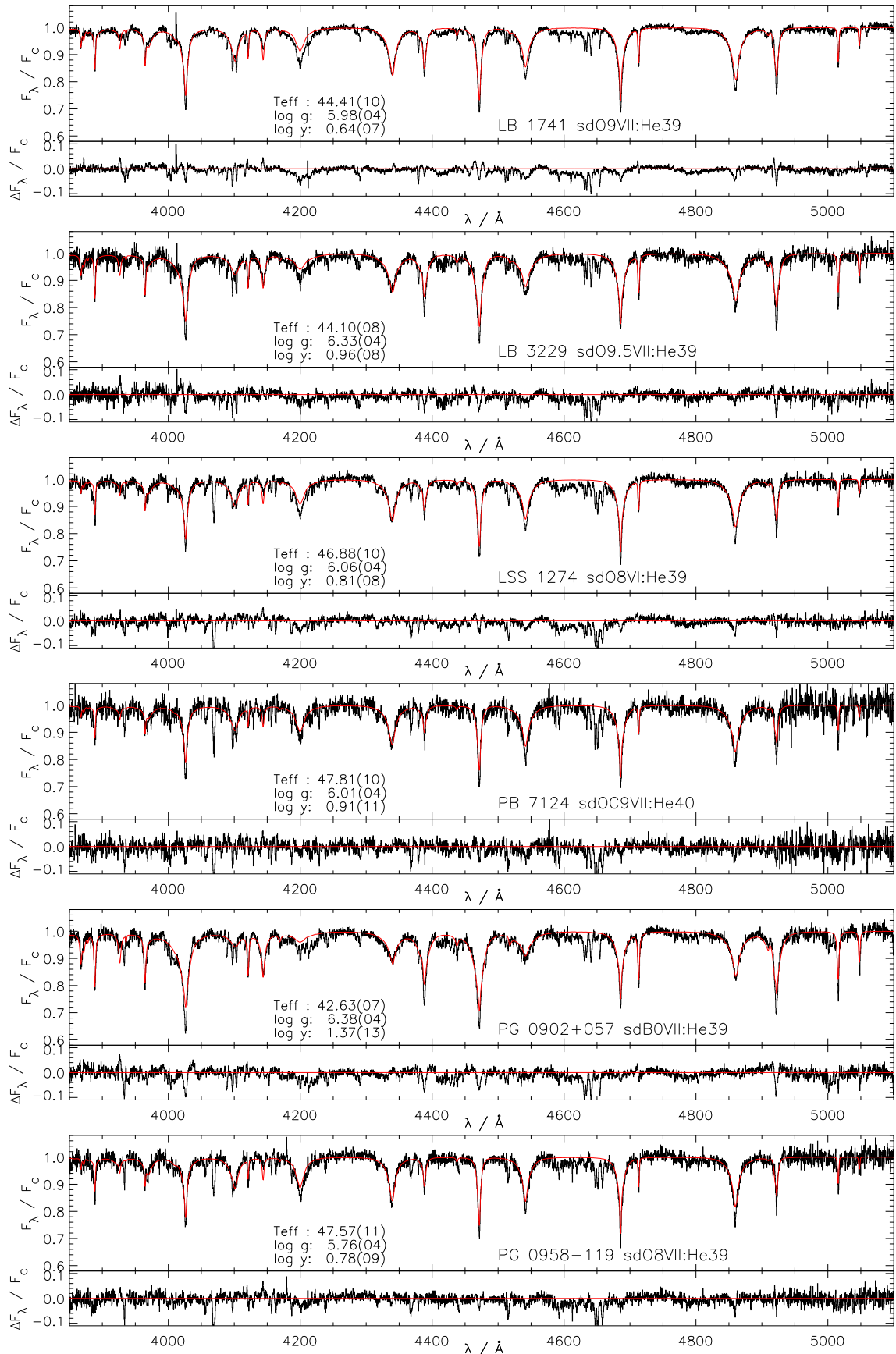


Figure E.7 – continued

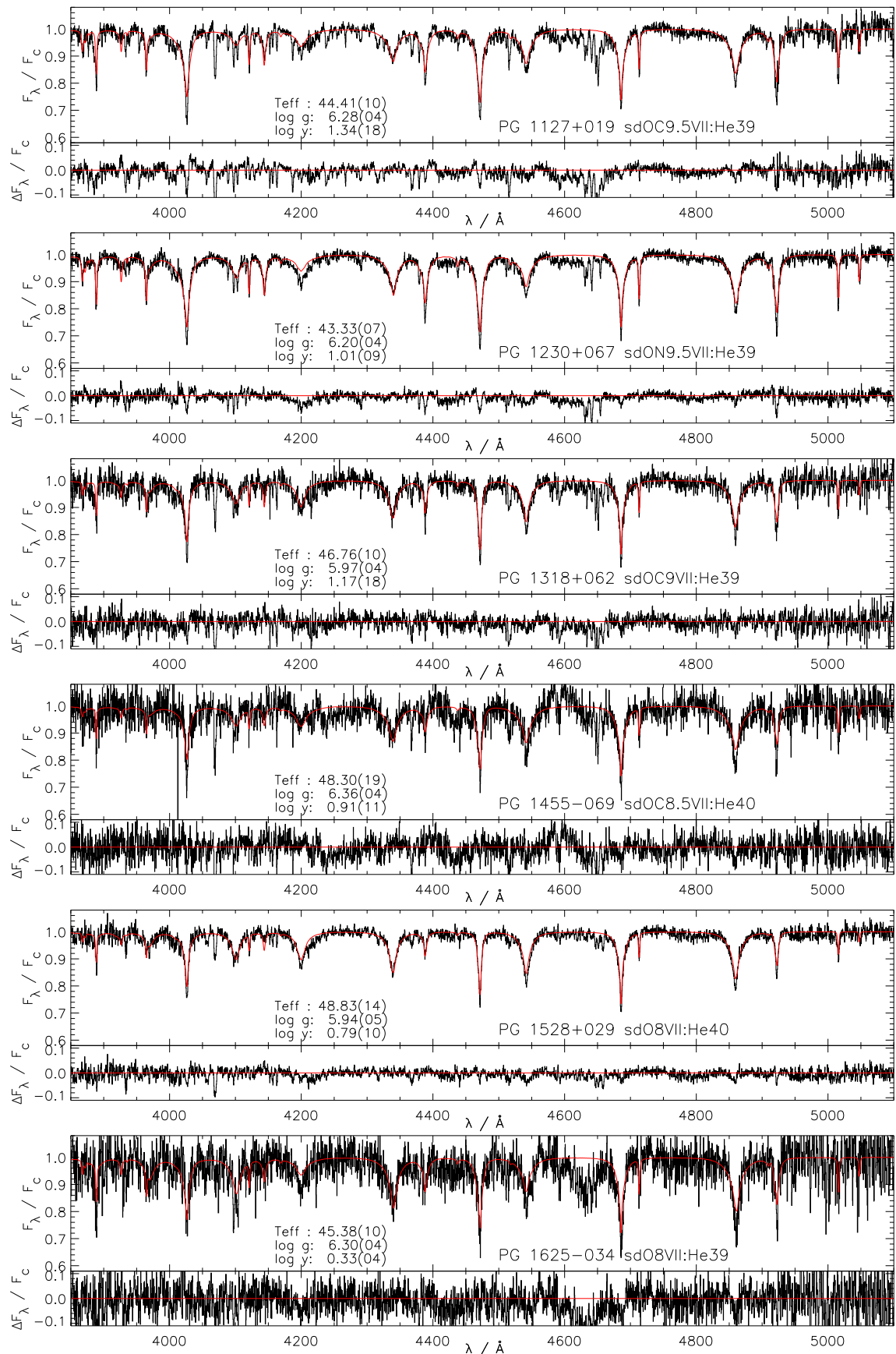


Figure E.7 – continued

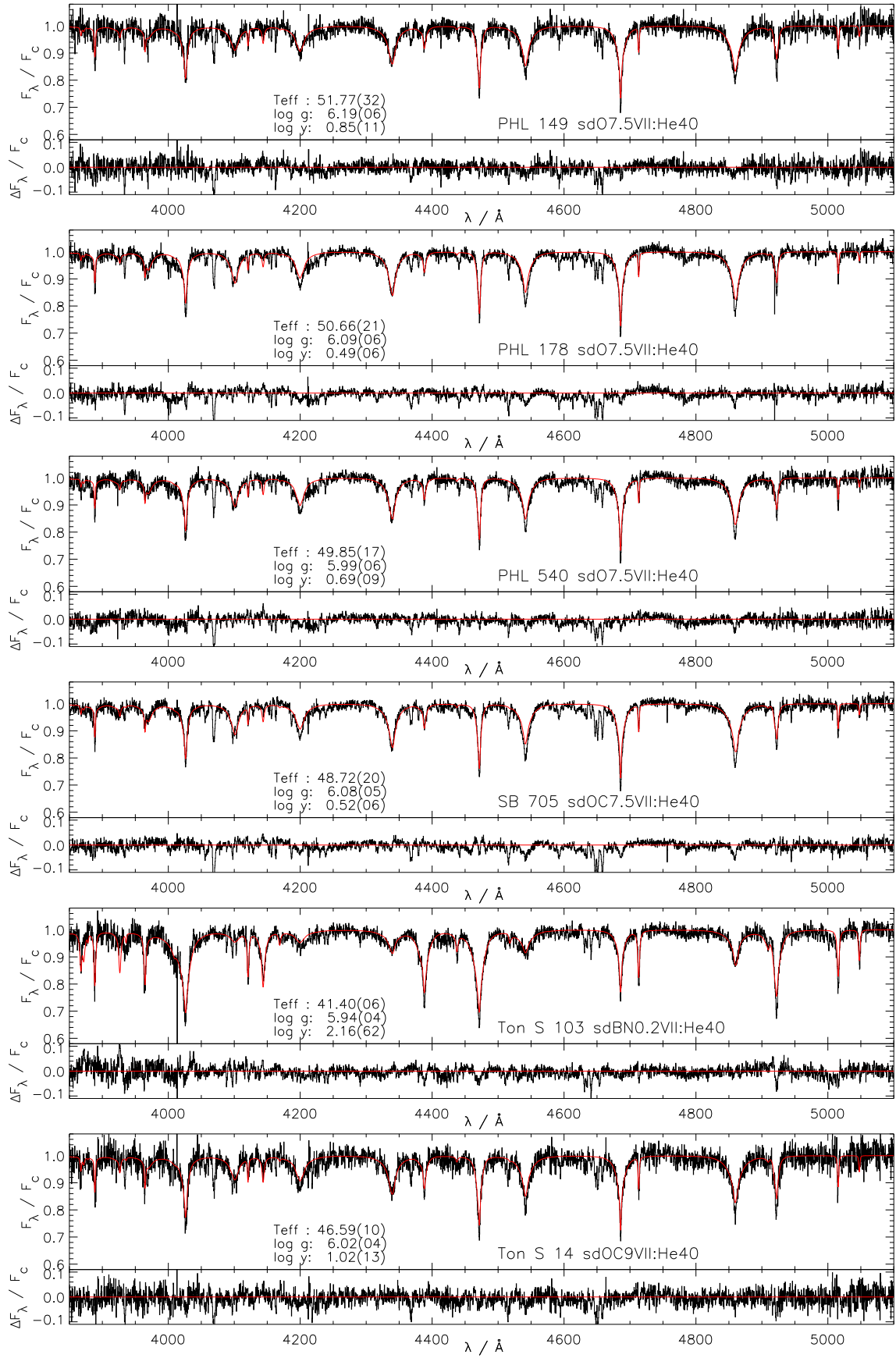
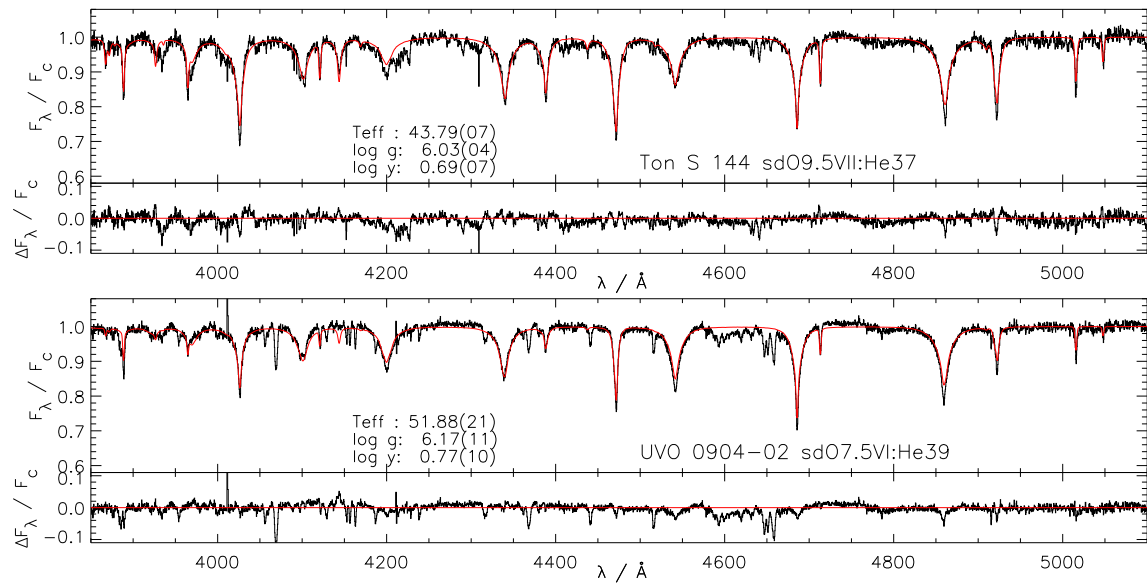


Figure E.7 – continued

**Figure E.7** – *continued*